POLITECNICO DI MILANO

School of Industrial and Information Engineering

DEPARTMENT OF ENERGY

MASTER OF SCIENCE IN NUCLEAR ENGINEERING

OPTIMIZING SOLPS SIMULATIONS IN A LINEAR PLASMA DEVICE
THROUGH THE SUPPORT OF THE GBS CODE FOR THE EVALUATION
OF THEORY-BASED DIFFUSIVITIES

Advisor: Prof. Matteo PASSONI

Co-Advisor: Prof. Paolo RICCI
Elena TONELLO
Louis Nicolas STENGER

Graduation Thesis of:
Massimo CARPITA
947554

ACADEMIC YEAR 2020-21

Contents

List of Figures

---

[1]Global Braginskii Solver
[2]Scrape-Off Layer Plasma Simulations

List of Tables

Sommario

I codici numerici multi-fluido per simulare il plasma di bordo in macchine a confinamento magnetico hanno un ruolo cruciale nella ricerca sulla fusione a confinamento magnetico (MCF). Due branche si sviluppano in questo campo, approcci mean-field e ai principi primi, differendo principalmente nel modo in cui trattano il trasporto in direzione perpendicolare alle linee di campo magnetico. I codici mean-field impiegano l'approssimazione diffusiva e valutano il trasporto perpendicolare mediante l'uso di coefficienti di diffusione efficace, solitamente stabiliti sperimentalmente. Al contrario, i codici ai principi primi sono capaci di simulare il trasporto perpendicolare in maniera auto-consistente. In questo lavoro di tesi due codici, SOLPS e GBS, rispettivamente basati su approcci mean-field e ai principi primi, sono accoppiati iterativamente per la prima volta. L'obiettivo è fornire a SOLPS un set di coefficienti di diffusione efficace valutati in maniera auto-consistente, estratti dal post-processing dei risultati di GBS. Ad oggi, un forte interesse nella comunità di ricerca MCF è indirizzato verso questo tipo di supporto ai codici mean-field da parte di quelli ai principi primi.

Il setup di simulazione è quello di un device lineare basato sulla macchina GyM (IFP-CNR, Milano). Opportune modifiche sono introdotte alla corrente versione di GBS per applicarlo a questo tipo di configurazione per la prima volta. Nonostante il ruolo fondamentale delle macchine lineari nello studio dei fenomeni legati ai plasmi di bordo, l'applicazione di codici multi-fluido per simulazioni di questi sistemi è stata raramente sfruttata.

Un plasma di He, con parametri tipici della macchina GyM, è prima simulato da una simulazione SOLPS preliminare, che fornisce gli input richiesti dalla seguente simulazione GBS. I risultati della simulazione GBS sono analizzati, evidenziando l'evoluzione di strutture turbolente e dei drift nel plasma, e dal loro post-processing sono costruiti profili radiali auto-consistenti per i coefficienti di diffusione efficace. Questi sono re-introdotti nel codice SOLPS per girare nuove simulazioni ottimizzate e valutare il loro impatto.

Parole chiave: Fusione nucleare, Plasma, Scrape-off layer, Trasporto, Codici multi-fluido, Coupling, Macchine lineari, Turbolenza, Coefficienti di diffusione efficace.

Abstract

Multi-fluid numerical codes to simulate the boundary plasma in magnetic devices currently play a crucial role in magnetic confinement fusion (MCF) research. Two branches develop in this field, mean-field and first principle approaches, differing mainly in the way transport is modelled in the direction perpendicular to magnetic field lines. Mean-field codes employs a diffusive approximation and compute perpendicular transport using effective diffusion coefficients, usually experimentally assessed. On the other hand, first principle codes are able to simulate perpendicular transport self-consistently. In this thesis work two codes, namely SOLPS and GBS, based on the mean-field and the first principle approaches respectively, are coupled in an iterative way for the first time. The goal is to provide to SOLPS a set of self-consistently evaluated profiles for effective diffusion coefficients, extracted from the post-processing of results from GBS. Nowadays, strong interest in MCF research community is directed towards this kind of support to mean-field codes coming from first principle ones.

The simulation setup of interest is a linear plasma device configuration based on the GyM machine (IFP-CNR, Milan). Suitable modifications are introduced on the current GBS version to apply it to this kind of configuration for the first time. Despite the fundamental role of linear plasma devices in the study of phenomena related to boundary plasmas, applications of multi-fluid codes for simulations of these systems have seldom been exploited.

An He plasma, characterized by realistic parameters for the GyM machine, is first simulated by a preliminary SOLPS run, extracting inputs needed for the following GBS simulation. GBS simulation's results are analyzed, highlighting turbulent structures and plasma drifts evolution in the plasma, and from their post-processing self-consistent radial profiles for effective diffusion coefficients are built. These are then adopted in the SOLPS code again to run optimized simulations and their impact is evaluated.

Keywords: Nuclear Fusion, Plasma, Scrape-off layer, Transport, Multi-fluid codes, Coupling, Linear plasma devices, Turbulence, Effective diffusion coefficients.

Introduction

This opening chapter aims at giving a general overview related to the background topics for this work.

It begins with a brief introduction to energy production from nuclear fusion, starting from the physics of nuclear fusion reactions (§ 1.1.1), presenting the concept of plasma state and its connection with nuclear fusion (§ 1.1.2) and then discussing the general energy balance which characterizes an ideal fusion power plant, pointing out the role of the so-called Lawson criterion (§ 1.1.3).

Once this element has been defined, it'll be described the magnetic confinement approach to nuclear fusion and its basic physical aspects (§ 1.2.1). Then one of the main engineering challenge related to these devices, namely the power exhaust problem, will be briefly addressed together with some of the currently adopted solutions (§ 1.2.2), before detailing the characteristics of the boundary plasma region (§ 1.2.3).

In the end, it'll be outlined the important role of linear plasma devices in magnetic confinement fusion research, in particular with respect to the above mentioned problem (§ 1.3).

1.1   ENERGY PRODUCTION BY NUCLEAR FUSION

Energy consumption is currently strongly linked to living standards and is proven to be highly unsustainable for societies aiming at an intense economic growth [30]. Nowadays, with a rapidly growing global population and a fast industrial development of a large number of countries, the interest in power production from nuclear fusion is set by the goal of achieving a clean, safe and virtually inexhaustible source of electric energy production against the increasing global demand, shown as a projection for example in figure 1.1.

Nuclear fusion, as a potential way to produce electric energy, presents a set of highly appreciated features: it has a very large intrinsic energy density, it is reliable and independent both from weather and geography, it is based on a virtually infinite fuel, it is environmental-friendly, safe and radioactivity is a minor issue with respect to nuclear fission. This justifies the intense research in this field despite its evident drawbacks, namely the large capital costs, including the up-front payment needed to fund research and the uncertain timing with which it will be available for large scale adoption.
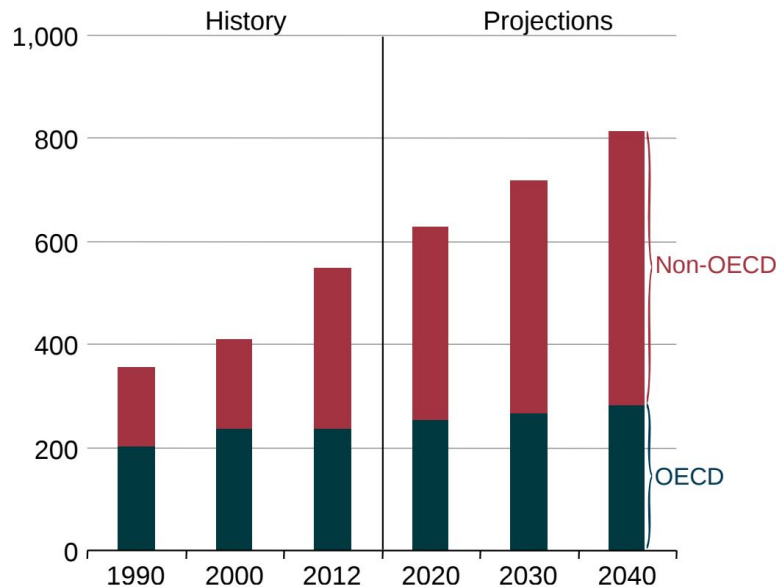
Figure 1.1: Historic and projected energy consumption. Taken from [2]. The ordinate is given in quadrillion British thermal unit, which approximately equals 1018 J.

1.1.1 *Nuclear Fusion Physics*

To understand most of the benefits and the difficulties related to exploiting nuclear fusion in energy production, one needs to start from the physics of the underlying reaction.

Nuclear fusion, as well as nuclear fission, is a process in which energy can be extracted exploiting the increase in binding energy per nucleon after this reaction has occurred. In particular, in nuclear fusion two light nuclei fuse together into an heavier and stabler product and the freed energy represents the net exothermic output of the reaction. The interaction involved in this process, namely the strong nuclear force, is very intense and presents a short range of action with respect to the electromagnetic force which characterizes chemical reactions. This is the main reason for the extremely large energy density[3] which characterizes nuclear fusion [101].

The approach of exploiting nuclear fusion reactions to produce energy is best suited for very light nuclei for two different reasons. First, the gain in binding energy per nucleon is in general much larger for two very light nuclei fusing together, as it can be seen in figure 1.2. Then, as the two nuclei should overcome the Coulomb potential barrier which arise due to their positive charges in order to fuse together, working with the lightest nuclei minimizes the required energy to trigger the reaction. For this reason the commonest choice for reactants in fusion applications are hydrogen and helium isotopes. The corresponding reactions, together with their energy output, are reported in table 1.1.

---

[3]Here intended as energy produced per unit mass of fuel. As a rule of thumb, for nuclear fusion this will be 10^6 times larger with respect to ordinary chemical reactions involved in power production
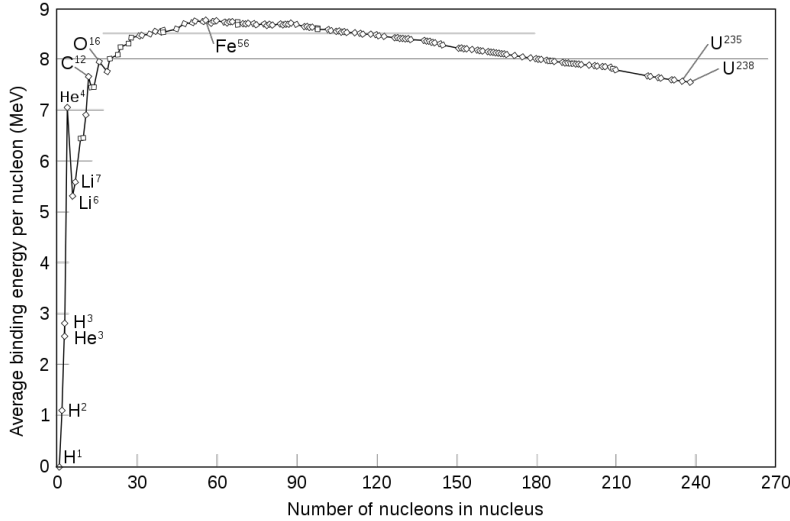
Figure 1.2: Binding energy per nucleon against number of nucleons.

Reactants	Products	E output (MeV)
$D + D$	$He_3 + n \ (br \ 50\%) \mid T + H \ (br \ 50\%)$	$3.27 \ MeV \mid 4.03 \ MeV$
$D + He_3$	$He_4 + H$	$18.3 \ MeV$
$D + T$	$He_4 + n$	$17.6 \ MeV$

Table 1.1: Commonest fusion reactions employed for power production purposes.

The typical form for the nuclear fusion *cross section* is expressed [77] as

$$\sigma(E) = \frac{1}{E} f(E) e^{-\sqrt{E_G/E}} \tag{1.1}$$

where E is the energy involved in the reaction, E_G is the so-called Gamow energy, which scales as the square of the involved nuclear charges, and $f(E)$ is a factor slowly varying with E. The exponential factor in formula 1.1 is taking into account the tunnel effect which, in a quantum picture, allows the reaction to occur even for involved energies smaller than the actual Coulomb barrier potential. This energy will be provided by the kinetic energy linked to the *relative velocity* v_r between the two colliding reactants. For power production purposes, where one would be interested in exploiting a large number of fusion reactions occurring together in a given time, the cross section plays a very important role in determining the *volumetric reaction rate* R which represents the number of reactions occurring between two given populations of reactants per unit time and per unit volume. R can be expressed [74] quite generally as

$$R = n_i n_j \langle \sigma v_r \rangle \tag{1.2}$$

where $n_{i,j}$ are the number densities[4] of the involved reactants populations and $\langle \sigma v_r \rangle$ is the average of the cross section and relative velocity product weighted on the relative velocity distribution between the two populations. $\langle \sigma v_r \rangle$ is also referred to as *rate coefficient*.

---

[4]From now on, the number density will be simply referred to as density.

This same exact definition of reaction rate can be applied also to other reactions between particles, with a coherent definition of σ from case to case. This will be important in this thesis work, for example, when dealing with the role of neutral particles in the system (see section 2.1.3).

Getting back to the fusion reaction rate, assuming Maxwellian distribution functions with *temperature T* for both reactants, one can express the factor $\langle \sigma v_r \rangle$ as a function of T only. This is shown in figure 1.3 where one can easily see that, in order to trigger in the most efficient way a large number of reactions, temperatures in the range between 10 to 100 keV are needed, roughly corresponding to more than a hundred million Celsius degrees.
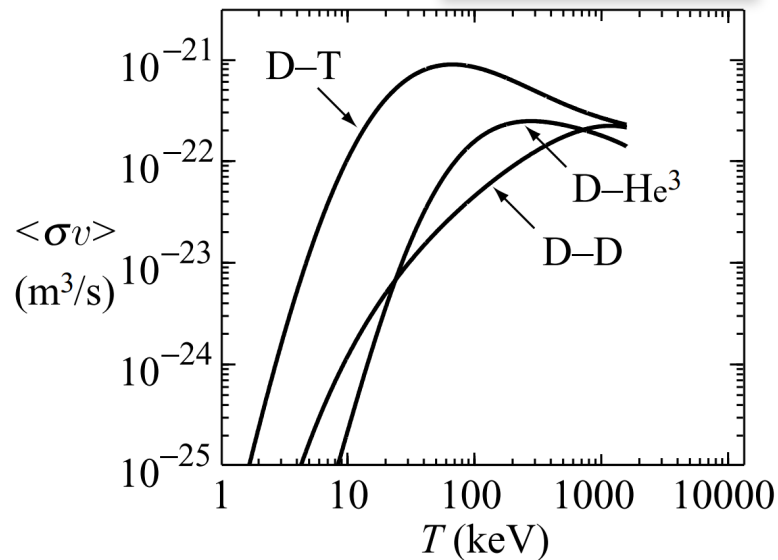
Figure 1.3: $\langle \sigma v_r \rangle$ as a function of T for commonest fusion reactions. Taken from [74].

1.1.2   The Plasma State

The large values of T required to achieve interesting fusion reaction rates imply that the reactants in fusion applications will be in the *plasma* state. A brief description of the main plasma state features is therefore here given in order to introduce concepts which will be useful in section 1.2.

The plasma state, usually attained at energies above the ionization energy threshold, is a state of matter characterized by a macroscopically neutral ensemble of particles with increased mobility which presents between its components at least two sufficiently large populations of oppositely charged particles, usually ions and electrons generated together in ionization processes. We also distinguish between partially and completely ionized plasmas depending on the presence of a neutral population between the plasma components.

Electromagnetic interactions, given the presence of charged populations, play a major role in determining the dynamics of matter in plasma state. The charged species, being affected by external electric and magnetic fields, make this system influenced by long-range collective effects, as opposed to short-range nearest-neighbour Coulomb collisions in ordinary matter such as solids, liquids and gasses. At the same

time the electromagnetic field is strongly affected by small-scale charge separation[5] and currents flowing as charged particles move. This strong coupling between electromagnetic fields and charged particles forms a self-consistent problem and a lot of efforts have been made in the field of plasma modeling to better comprehend this complicated subject. In this thesis, for example, we will focus mainly on a given modeling strategy for plasmas, namely the multi-fluid model (see section 2.2).

Another issue with the comprehension of the plasma state is that known examples of different plasmas may range among an extremely wide range of densities and temperatures. For example the density and the temperature may decrease of about 20 and 5 orders of magnitude respectively going from plasmas obtained in inertial fusion applications (see § 1.2) to plasmas in the ionosphere. It is then clear that it is not easy to compare the qualitative behaviour of these systems. A detailed analyses of the specific plasma state of interest for this thesis will be carried out between section 1.2.3 and chapter 2. Nonetheless, the usage of adimensional parameters, being dependent by their nature only on the relative magnitude of the quantities characterizing a plasma, may in general help in capturing some features of these systems without relying directly on the individual magnitude of each quantity. This approach has proven to be able to provide good results and was employed directly in the design of practical experiments, allowing scientists to determine complex plasma behaviour by means of a set of different adimensional parameters [91].

1.1.3 *Energy Balance for Fusion Power Plants*

In the following we will consider the $D - T$ reaction among the 3 reactions presented in section 1.1.1. This is because currently the $D - T$ reaction is believed to be the most promising one for fusion reactors [88] since it achieves the highest $\langle \sigma v_r \rangle$ value at the lowest temperature, as it can be seen in figure 1.3, while providing a large E output per reaction, as it is shown in table 1.1.

Considering the $D - T$ reaction, the neutron generated in the process, as it can be shown by elementary conservation balances in momentum and energy, will take on 4/5 of the energy produced. As the neutron, being electrically neutral, can't be confined in the same way we'll describe in detail later for charged particles, one may think of exploiting it to produce the required heat to sustain a thermodynamic cycle and produce electric energy. At the same time, the charged He_4 ions, together with the remaining 3.5 MeV of energy they gain from the reactions, will go on giving energy to the plasma maintaining its temperature on the required level to guarantee an adequate fusion reaction rate. This contribution can be modeled, exploiting expression 1.2, as

$$S_\alpha = 3.5 \ MeV * \frac{n^2}{4} \langle \sigma v_r \rangle \tag{1.3}$$

where we define $n = n_e = 2n_D = 2n_T$ assuming a completely ionized overall neutral $D - T$ plasma with the two species having the same density. Together with the

---

[5]A plasma is kept macroscopically neutral by electromagnetic restoring forces shielding out small scale charge separations. The typical scale of these phenomena is the *Debye Length* λ_D, in the simplest case equal to $\sqrt{T_e/4\pi ne^2}$ (in CGS units), where T_e is the electron temperature and n the plasma density [52].

energy provided by He_4 ions, an *external source* of power can be applied and we will refer to this as S_{ext}.

At the same time, energy loss mechanisms are active in the system. These can be divided into two categories. One is *radiative losses*, mainly composed by Brehemsstrahlung processes due to ion-electron scatterings, to which we'll refer as S_R and which can be computed [74] as

$$S_R = c_B Z_{eff}^2 n^2 \sqrt{T} \tag{1.4}$$

where c_B is a constant approximately equal to $10^{34} \ W/cm^2$ and Z_{eff} is the effective atomic number. The other loss contribution is due to *heat diffusion* through the boundary of the system, to which we'll refer as S_Q. The consistent definition of this term is definitely complicated and it is often modeled introducing an empirical factor called *energy confinement time* τ_E [99] which characterizes the typical diffusion time for internal energy of the system. The τ_E term actually embodies a lot of physical aspects of the fusion plasma mainly related to transport properties. The definition of the heat diffusion term then becomes

$$S_Q = \frac{3nT}{\tau_E} \tag{1.5}$$

In a steady state system it must hold $S_\alpha + S_{ext} = S_R + S_Q$. Working on this power balance imposing the input terms must be greater or equal than the losses, expressing each term as mentioned in formulas 1.3, 1.4 and 1.5 and introducing the factor $f_\alpha = S_\alpha/(S_\alpha + S_{ext})$, it is then possible to derive [74]

$$n\tau_E \geq \frac{12T}{(1/f_\alpha) * 3.5 MeV * \langle \sigma v_r \rangle - 4c_B \sqrt{T}} \tag{1.6}$$

Considering the ignition condition, namely the condition in which the fusion reactions are able to sustain the plasma by themselves only and hence $S_{ext} = 0$, the right hand side of expression 1.6 becomes a function of T only. For $D - T$ reactions its minimum is reached at $\sim 25 \ keV$ and we have

$$n\tau_E \geq 2 * 10^{14} \ s \ cm^{-3} \tag{1.7}$$

known as the *Lawson criterium* [79]. Lawson criterium will be the base to clarify the two currently adopted approaches to nuclear fusion power production presented in the next section. It sets a minimum requirement for the performances of the reactor in this case. It is also true that it can be reduced by applying an external power source, but this will come at the expense of the efficiency of the power production cycle. Indeed from the engineering side, the interesting parameter is the *engineering gain factor* Q_e, defined as $(S_{out}^{ele} - S_{in}^{ele})/S_{in}^{ele}$ where power contributions are intended in their electric forms, therefore considering in the balance all the conversion and absorption efficiencies, and where the total output contribution involves heat and radiation losses as well as the contribution related to the neutrons escaping the plasma[6] [74].

---

[6]Eventually corrected by taking into account also the energy released in breeding reactions with Li in the blanket in $D - T$ fueled fusion reactor concepts [74].

1.2   MAGNETIC CONFINEMENT FUSION

Expression 1.7 shows that there is some degree of freedom in achieving the required state to sustain a plasma in the conditions to run a fusion power plant. Indeed two main approaches were developed focusing independently on each of the two quantities at the left hand side of the same equation, namely the plasma density and the energy confinement time[7].

The first approach is *inertial confinement fusion*, often referred to simply as *ICF*. This is aimed at reaching the largest possible value for n relaxing the requirements on the needed energy confinement time. Indeed in this case the confinement is provided just by the inertia of the plasma and τ_E is around 10^{-9} s for usual applications [48]. Therefore the required plasma density which should be reached is near $\sim 10^{23}$ cm^{-3}, a very large value which is usually obtained through laser-driven compression techniques.

The second approach is *magnetic confinement fusion*, often referred to simply as *MCF*. This is aimed at reaching the largest possible value for τ_E relaxing the requirements on the needed plasma density, which is then usually limited to values around $\sim 10^{14}$ cm^{-3}, an extremely low value compared to ordinary gasses such as air ($\sim 10^{19}$ cm^{-3}) for example. Therefore the characteristic energy confinement time τ_E needs to reach values in the order of ~ 1 s. As its name implies, this strong confinement is meant to be reached by employing external magnetic fields.

In the framework of this thesis we'll focus on MCF only and we'll describe in more detail some of its features and its related physics in next sections.

1.2.1   *Magnetic Confinement Physics*

The main idea behind MCF is to employ magnetic fields in order to confine charged particles motions into confined orbits. Indeed it is well known [52] that a charged particle moving inside a magnetic field tends to move on an helical orbit along magnetic field lines characterized by a given frequency Ω_L, called *gyro-frequency*, and a given radius ρ_L, called *Larmor radius*, which are equal to

$$\Omega_L = \frac{eZB}{m} \qquad \rho_L = \frac{mv_\perp}{eZB} \qquad (1.8)$$

where Z is the particle charge in multiples of e, B is the magnetic field magnitude at particle position, m is the particle mass and $v_\perp$ is the magnitude of the particle velocity in the direction perpendicular to the magnetic field direction at the particle position. This peculiar behaviour, known as *gyro-motion*, provides in first approximation a way to confine particles in directions perpendicular to the magnetic field. The gyro-motion is the underlying dynamical pattern for charged particles in a magnetic field and this influences, for example, related transport properties (see section 2.1).

In order to provide confinement also in the parallel direction different strategies can be applied. A first option is the *open field configurations* employing open magnetic field lines starting and ending into solid walls. These are usually linear

---

[7]It is worth noticing that an intermediate approach, namely the magnetic inertial fusion, is also under study, even if its state-of-the-art is not as developed as with MCF and ICF [50].

machines exploiting the so-called mirror effect reflecting most of the charged particles inside the machine thanks to positive B gradients towards walls in the direction parallel to the magnetic field [71]. The other option is employing *closed field configurations* and these are currently the relevant candidates considered for fusion devices. In this kind of configuration the magnetic field is bent and enclosed inside a bounded region of space assuring charged particles endless available trajectories. This is the configuration we will focus on in the following.

The easiest natural choice, when it comes to thinking about a magnetic field configuration to be employed in closed field devices, is the toroidal one. The simple gyro-motion picture would then predict the charged particles will revolve around closed toroidal field lines in closed helical paths. Unfortunately the gyro-motion picture is just the zero order approximation of the motion of a charged particle in electromagnetic fields. Employing the first order *guiding center approximation*, drifts are identified which superimpose over the simple gyro-motion. In particular we define the following drifts

$$\mathbf{v}_E = \frac{\mathbf{E} \times \mathbf{B}}{B^2} \qquad \mathbf{v}_{\nabla B} = \frac{2K_\parallel}{eZB} \frac{\mathbf{B} \times \nabla B}{B^2} \qquad \mathbf{v}_{curv} = \frac{K_\perp}{eZ} \frac{\mathbf{R}_C \times \mathbf{B}}{B^2 R_C^2} \qquad (1.9)$$

where $K_{\parallel,\perp}$ are respectively the kinetic energies linked to particle velocity in parallel and perpendicular direction with respect to the magnetic field and R_C is the curvature radius of the magnetic field. Each of these drifts would eventually arise in a simply toroidal magnetic field configuration ending up spoiling the plasma confinement in the perpendicular plane. A possible solution to this problem is to employ together with the toroidal magnetic field, to which we'll refer as $\mathbf{B}_T$, an additional poloidal magnetic field $\mathbf{B}_P$, as shown in figure 1.4, which will help averaging out the drifts allowing charged particles to be confined inside a toroidal volume [52]. We distinguish between *tokamaks* and *stellarators* devices depending on the way this poloidal field is produced, respectively by means of a toroidal electrical current induced directly in the plasma or with an external system of coils.
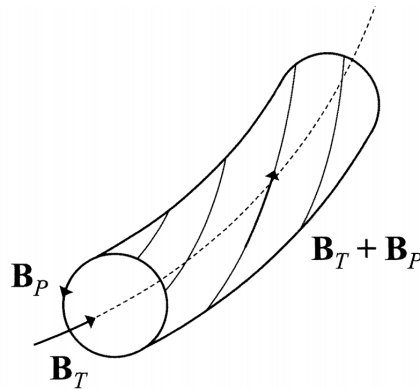
Figure 1.4: Representation of a magnetic field line resulting from the superposition of a toroidal and poloidal field.

Further forethought is required when one passes from a single particle picture to a macroscopic system of interacting particles. In this case it can be shown the presence of different forces acting on the plasma and leading to loss of confinement

in radial direction. The nature of these forces is directly linked to the toroidal geometry and the *MHD equilibrium model* can be employed for a detailed analysis of these physical aspects and their effects. Different techniques are then employed to counter these phenomena and we can briefly list the two most important ones, namely the employment of a straight vertical magnetic field and a nearly perfectly conducting material for the walls of the machine [74]. Despite these solutions, perfect confinement can never be recovered as it will be outlined in next section together with the consequences associated.

In addition, in a macroscopic picture also the drifts arising in the system must be redefined coherently employing macroscopic quantities. This will be seen in detail in sections 3.1.2 and 3.2.2.

1.2.2 *First Wall and Power Exhaust*

It was already outlined in section 1.1.3 that neutrons and electromagnetic radiation fluxes will be coming out of the plasma in a fusion reactor. Those fluxes will first meet the walls of the chamber containing the plasma. More precisely, we refer to the *first wall* as the group of all the components directly facing the plasma. In addition to this fact, despite all the efforts which can be made in trying to confine a plasma with the strategies defined in the previous section, perfect confinement is prevented by different mechanisms arising in the system, mainly *instabilities* and *transport phenomena*. The first wall is then subject to important energetic heat, radiation and charged particles fluxes.

These facts underline the importance of the first wall design, a crucial element on the pathway for a working fusion reactor. The first wall will have to perform 4 main functions [86]:

1. sustain the impact of the particles and radiation without releasing many impurities in the plasma and without a large degradation of its thermo-physical properties.

2. transfer the intense heat load coming from the plasma to a cooling medium and withstand the resulting thermal stress, while allowing the neutron flux to reach the blanket modules where the kinetic energy of the neutrons is used to heat up a coolant as in a primary loop of a conventional heat-power plant.

3. be able to withstand highly localized heat loads during events such as disruptions, edge-localized modes (ELMs) or generation of runaway electrons and the related electromagnetic loads.

4. minimize the tritium retention in accordance with the general objective of a low tritium inventory for reasons related to radiation safety.

The problem of controlling power exhaust in fusion reactors is double-sided. From the point of view of the first wall, one would like to allow the power to be removed on the largest possible surface, while from the point of view of the plasma one would like to reduce as much as possible the contamination induced by impurities generated mainly by charged particles impact on the first wall [86]. It is then crucial to carefully manage the contact between the plasma and the first wall limiting charged particles fluxes, and the associated heat fluxes, on restricted areas

where the impurities volume can be reduced and controlled. Different configurations can be used in general for this purpose. In each case the main idea behind these solutions is to place a solid target at some point along a magnetic field line in order to intercept charged particles and neutralize them, therefore acting as a sink for the plasma. The enormously larger parallel transport along magnetic field lines, compared to the slow transport processes in radial directions (see section 2.1), will then allow the first wall to be effectively isolated from the plasma [74, 86].

The two configurations which were studied the most in past years are the so-called *limited* and *diverted* configuration. A sketch of their schematics is presented in figure 1.5. The limited configuration consists in placing a solid protrusion inside the reactor chamber volume; the surface of this protrusion will then be subject to particle and heat fluxes from the plasma. The diverted configuration instead exploits an additional system of coils to modify the topology of outer magnetic field lines in order to direct charged particles towards a specific region of the reactor chamber where solid target plates are present.
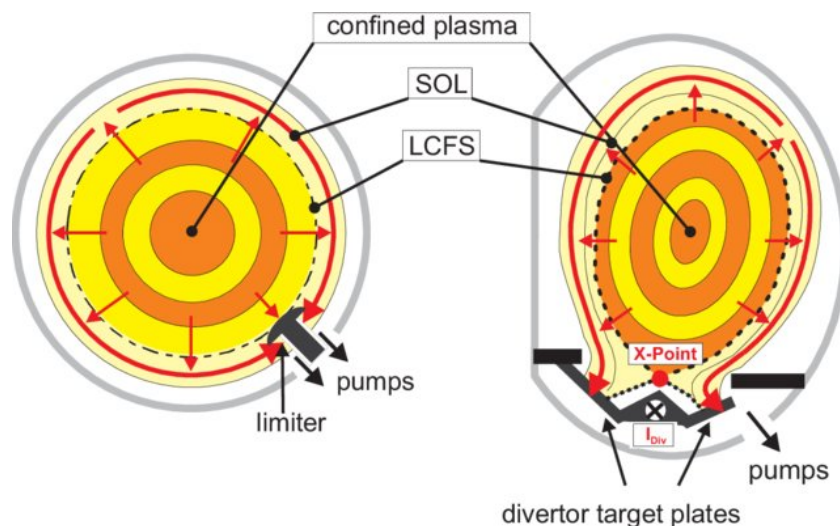
Figure 1.5: Limited (left) and diverted (right) configurations schematics.

The choice between limited and diverted configurations is not trivial and is still currently under study. The balance between beneficial aspects favours diverted configurations at the moment. In first place, this is because, by design, diverted configurations move the region of plasma-target contact away from the bulk plasma and therefore reduce the plasma contamination by impurities. This happens for two reasons at the same time: impurities should travel a longer distance to reach the bulk plasma and their yielding rate is reduced by the possibility of having negative temperature gradients[8] for the plasma temperature towards the diverted targets. Also other advantages were shown to be present in the diverted configuration, among which we can list the greater efficiencies of pumps in removing impurities (either generated in the plasma-target interaction or in the bulk plasma, such as He) and the fact that larger value for energy confinement time were reached in this configuration [99].

---

[8]Sputtering yield (see section 2.1.1) increases with charged particles energy [67].

1.2.3 *The Scrape-Off Layer*

As it was shown in the previous section, the unavoidable plasma-wall interaction is controlled by placing solid targets along magnetic field lines intercepting the charged particles stream along them. These field lines are therefore now open and we identify as *last closed field surface* (*LCFS*) the last magnetic field flux surface before this contact occurs. Despite this scheme allows for effective isolation of the first wall, the plasma is still able to diffuse for a short distance radially while streaming along open field lines towards targets; this creates an outer plasma layer to which we refer as *scrape-off layer* (*SOL*), extending from the LCFS up to usually a few centimeters in the radial direction. This can be seen both for the limited and diverted configuration in figure 1.5.

The SOL dynamics is of crucial importance in determining the overall performances of a fusion reactor. As it was already underlined, it establishes the boundary conditions for the core plasma, controlling the plasma-wall interaction. It controls also the impurity dynamics, the plasma refueling and it is responsible of power exhaust related to charged particle fluxes. The SOL width, for example, controls the wetted area of plasma facing components and, therefore, the maximum heat flux that needs to be evacuated. In addition, scrape-off layer physics is believed to play a crucial role in the L-H confinement modes transition. Improving the understanding and the predicting capabilities of SOL physics is therefore essential for the success of thermonuclear fusion [5, 29].

In the SOL region, a wide range of spatial and temporal scales is involved and its characteristics are fairly different from the inner plasma regions, as a number of approximations that are typically used in the study of the core plasma are not valid. In particular this region is highly turbulent, as shown in figure 1.6, and characterised by the presence of coherent turbulent structures, called blobs, that detach from the main plasma and move radially outwards. As their spatial scale is comparable to that of the SOL, separation of turbulent and equilibrium scale lengths can't be simply applied and strong nonlinearity arises in SOL dynamics. The analysis is complicated also by a magnetic geometry which can get particularly complex, especially in diverted configurations [45, 89]. The plasma in the SOL is not confined but rather it's lost continuously after reaching the solid targets, near which also the quasi-neutrality assumption $n_i \sim n_e$, usually holding in the whole fusion plasma, breaks down [82]. This induces fast drops in plasma density and temperature in the SOL which reach therefore low values with respect to the bulk plasma in the reactor [85]. Accordingly, the collision rates increase in the SOL [73] and thermodynamic equilibrium can be readily reached.

The SOL physics will be underlined further in chapter 2 of this thesis work, especially with respect to its transport properties. The knowledge of SOL characteristic features will be fundamental in order to identify possible strategies to model and simulate its dynamics.

1.3 Linear Plasma Devices in MCF Research

While the study of plasma confinement is intrinsically related to the employment of closed field line devices, some peculiar aspects of fusion reactor research can be
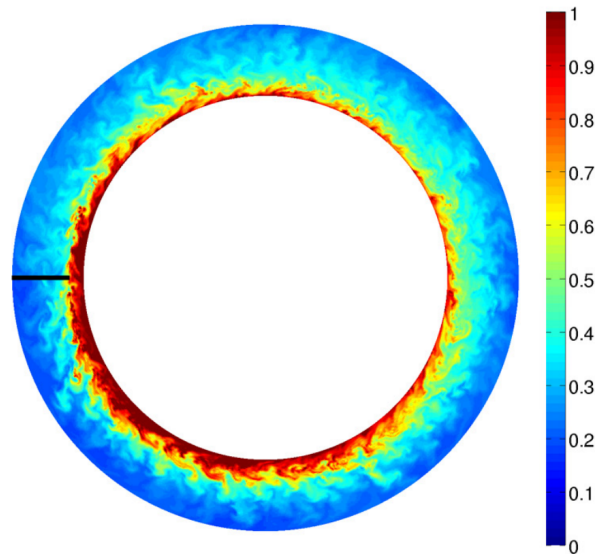
Figure 1.6: Plasma density (normalized to density at LCFS) simulated in the edge region of a tokamak including the SOL. The simulation was carried out with GBS code (§ 3.2) in a limited configuration. Taken from [24].

studied also in different devices, such as *linear plasma devices* (*LPDs*). This is true in particular for plasma-wall interaction studies and for other boundary phenomena. Nowadays, different kinds of nuclear fusion relevant studies have been already carried out in linear devices such as, for example, plasma heating mechanisms [70], plasma detachment [87], plasma-wall interaction and materials modification due to exposure to fusion-relevant plasmas [3]. Among the most important linear devices all over the world one can find for example:

- MPEX (Material Plasma Exposure eXperiment), planned to be built in 2023, and its precursor Proto-MPEX at Oak Ridge National Laboratory, in Tennessee, US. This machine will be able to produce high-intensity plasma source by RF technology to study long term effects of the contact of the fusion plasma with divertor components [27].

- Magnum-PSI at the Dutch FOM Institute for Plasma Physics, designed to study ITER-relevant plasma surface interactions [84]. This machine generate a plasma combining the effect of expanding hydrogen plasma arc and RF heating. It is able to produce plasma shots with a few seconds duration approaching high plasma fluxes expected in ITER divertor.

- Pilot-PSI is the forerunner of Magnum-PSI, built at the same institute and employed to study the production and transport of hydrogen plasma at flux densities that are required for Magnum-PSI [33]. Also this is a pulsed device.

- MAGPIE (MAGnetized Plasma Interaction Experiment) has been built in the Plasma Research Laboratory at the Australian National University, with the aim to study plasma surface interaction physics, advanced remote diagnostic development and plasma production and heating with helicon sources [92].

- GyM (Gyrotron Machine) is a medium-flux linear machine built at the Istituto di Fisica del Plasma (IFP) in Milan, Italy. It is aimed at the study of basic aspects of plasma physics, such as plasma heating and turbulence, and also material interaction with fusion relevant plasmas [76]. A more detailed description of this device will be given in section 2.4.

Linear machines are open field lines devices with a structure which in general can be summarized as follows: a cylindrical vacuum chamber is surrounded by coils in the axial direction in which electric current flows and generate a magnetic field. A plasma generated inside this machine will therefore share some important features with edge plasmas in closed field devices (see § 1.2.3), namely a strong anisotropic transport and the presence of solid targets acting as sinks and intercepting magnetic field lines. In addition, this kind of devices allows to reach densities and fluxes which are currently prohibitive in closed field lines devices but are compatible with expected future fusion reactors. Neutral particles presence is also an important feature in these systems and this enables the investigation of the physical aspects related to plasma-neutrals interactions. Therefore LPDs are able to capture a lot of important physical aspects of boundary plasma while simplifying at the same time some issues related to transport modeling using a simpler magnetic configuration with respect to closed field lines devices [23].

In conclusion, the relatively simple configuration of LPDs offers the possibility to build easier to manage and cost-effective facilities to address aspects of key importance for controlled magnetic fusion [37]. This description of their importance in magnetic fusion research will be fundamental in understanding the motivation and goals for this thesis, as described in section 2.5.

Modeling of the Scrape-Off Layer

In the chapter 1 we remarked the key-role of the scrape-off layer in nuclear fusion reactors and the importance of linear devices for studies linked to that topic. In this chapter we will discuss further details with respect to their modeling, both from the physical and the computational side.

First we will tackle the subject of transport in plasmas, beginning from the most general characteristics and then detailing some typical features related to the SOL. In particular, we'll underline the role of a solid wall (§ 2.1.1), of the turbulence (§ 2.1.2) and of the neutrals species (§ 2.1.3) in this region.

We proceed by introducing the multi-fluid physical model for plasmas, starting from its general description and then specifying it in the case of edge plasmas (§ 2.2.1). Its limits and related approximations will be also pointed out (§ 2.2.2).

As long as the physical model for the SOL will be presented, it will be also evident the need for corresponding numerical approaches to solve its dynamics. Two main approaches in this field will be presented, namely the mean-field (§ 2.3.1) and the first principle ones (§ 2.3.2), together with their principal characteristics and limits. The interest in a possible coupling between these two approaches will be also analyzed (§ 2.3.3).

The attention will be then drawn to the issue of modeling plasmas in linear devices, also with respect to aspects discussed previously (§ 2.4).

The presentation of all the previous themes will then naturally lead in conclusion to the definition of the goal and the motivation behind this thesis work (§ 2.5).

2.1 Transport in the Scrape-Off Layer

A strong complexity, which arises when one starts to deal with the analysis of a plasma as a macroscopic system, is related to transport of different quantities: energy, momentum and particles. A wide plethora of physical phenomena may be ascribed as the cause for transport mechanisms.

When just binary collisions are considered and only small deviations from thermodynamic equilibrium can be assumed (which is the case in the SOL, see section 1.2.3), the kinetic theory of transport in plasmas proves to be a natural generalization of the well known theory of transport in standard gases, taking into account also the influence of collective effects on charged particles due to the

external presence of electromagnetic fields [103]. In this case we speak of *classical transport theory* [66].

The first important feature which can be noticed when dealing with transport in magnetically confined plasmas is that this is completely anisotropic with respect to the direction of the magnetic field. We already know from section 1.2.1 that in a single particle picture the motion for charged particles is unconstrained in the direction parallel to a constant magnetic field while it is limited to an excursion equal to the Larmor radius in the plane perpendicular to magnetic field lines. Taking into account a large number of particles, and therefore collisions, this difference is smoothed out by enhancing radial diffusion and limiting the parallel mobility, but in any case the difference of transport coefficients in the two cases is significant. This can be seen in a simple way by applying the diffusion approximation [52] for transport phenomena. Take for example the case of particles transport: this means that we'll estimate the characteristic velocity v_i in the direction x_i for the transport of particles (with density n) as linear with respect to n variation in this same direction

$$v_i = -D_{n,i}\frac{1}{n}\partial_{x_i}n \tag{2.1}$$

with $D_{n,i}$ called *diffusion coefficient*. With the help of a simple *random walk model* [74] one can estimate $D_{n,i}$ as

$$D_{n,i}^{classic} = \nu\Delta l^2 \tag{2.2}$$

with Δl being the excursion of particles in x_i direction following collisions and ν the collision frequency. It is therefore clear that in a magnetized plasma the situation is pretty different with respect to the direction of the magnetic field lines: in the parallel direction Δl will be linked just to the mean free path between collisions while in the radial direction this will be limited by the Larmor radius.

The predictions of classical transport theory provided a really optimistic vision on the problem of radial transport in fusion reactors as they claimed $D_{n,\perp}^{classic} \sim 1/B^2$, which would have resulted in the possibility of achieving excellent confinement of a fusion plasma just by improving our capabilities in producing large B fields. Unfortunately, experiments have shown these predictions were wrong by different orders of magnitude and the radial transport was way larger than expected. A first correction in this direction was proposed introducing toroidal effects and combining the concepts of guiding center drifts and trapped particle trajectories in the definition of Δl [74], leading to the so-called *neo-classical transport theory*. This wasn't still enough to recover the large values of transport obtained in experiments though. Further mechanisms, mainly ascribed to different kinds of micro-turbulent fluctuations in plasma quantity, are indeed present in plasmas, causing perturbations in the guiding center orbit of particles. In this framework we speak of *anomalous transport theory*, a subject which is still far from being completely understood and which now represents one of the major challenges in theoretical plasma physics [59]. Further details on this last topic are provided in section 2.1.2.

Everything said so far is in general valid for any fusion plasma but it becomes particularly essential in the description of the SOL in fusion reactors as here transport processes are determining both the input from the core plasma, the geometry and the boundary conditions (either towards solid walls and in the radial direction) which will characterize this region. In addition, other peculiar

features which are going to be described in the following in this section, are strongly influencing transport properties and dynamics of the SOL.

2.1.1 *Plasma-Wall Interaction*

As it was already outlined in section 1.2.3, the SOL controls the plasma-wall interaction, establishing the boundary conditions for the plasma in a fusion reactor and the power exhaust related to charged particles striking on the wall.

Focusing on the plasma side, the plasma-wall transition plays a central role in establishing the density, the temperature and other properties of the plasma by mediating its fluxes of heat and particles towards the solid walls [99].

In order to comprehend the way in which this mediation occurs, one has to understand in which way the SOL plasma becomes aware of the presence of a solid wall. Let's start noticing that a solid wall acts as a sink for a plasma as it catches the charged plasma species striking on it, mainly by capturing electrons and by neutralizing ions. The complex set of reactions involving charged and neutral particles at solid walls will be described more in detail in section 2.1.3.

In first place, let's consider a simple 1-D unmagnetized quasi-neutral plasma in thermodynamic equilibrium and in contact with a solid wall. This same setup is a reasonable approximation when magnetic field lines are perpendicular to the solid wall surface. As the inertia of the electrons is much lower than the ions', when the plasma enters in contact with a solid wall, considered floating for simplicity, it first establishes a potential drop near the walls causing negative charges to be slowed down while positive charges are accelerated. The negative net charge accumulated on the wall is readily shielded out in the plasma by means of the *Debye shielding* [74] in an adjacent layer with a characteristic scale length in the order of the Debye length $\lambda_D = \sqrt{T_e/4\pi n e^2}$. This implies a net positive charge is accumulated before the wall in this layer breaking the quasi-neutrality condition in the plasma. This layer is referred to as *Debye sheath*. Moreover the shielding is not complete as a small fraction of potential drop is able to penetrate further than this region inside the quasi-neutral region of the plasma, in a layer called *pre-sheath*, causing ions and electrons to accelerate and decelerate respectively in the direction of the solid wall. Defining the location of the Debye sheath entrance as the point in which quasi-neutrality assumption breaks would be someway arbitrary. It is therefore usually defined according to the *Bohm criterion* [97], according to which in this simple case the existance of this layer region is correlated with ions reaching their *sound speed* $c_s = \sqrt{(T_e + T_i)/m_i}$ after being accelerated in the pre-sheath.

At the same time, the surface sink action, causing a depression in both electrons and ions densities, imposes a negative pressure gradient in the direction of the solid wall, making ions and electrons accelerating further towards it. On the electrons, this force almost balances out the deceleration due to the potential drop making them obey the so-called *Boltzmann factor relation* [99] and therefore $n_e = n_{e0}e^{[\Phi/T_e]}$, with n_{e0} as the density of electrons in the bulk plasma. This fact, together with the constraint of preserving quasi-neutrality in the pre-sheath, implies that in this simple case electrons must enter the Debye sheath with a velocity [82]

$$v_{se}^{ele} = c_s e^{[\Lambda - e(\Delta\Phi)/T_e]} \tag{2.3}$$

where $\Delta\Phi$ is the potential drop in the Debye sheath and Λ is the Coulomb logarithm [99]. The variation of different plasma quantities before the wall in this simple case is represented in figure 2.1.
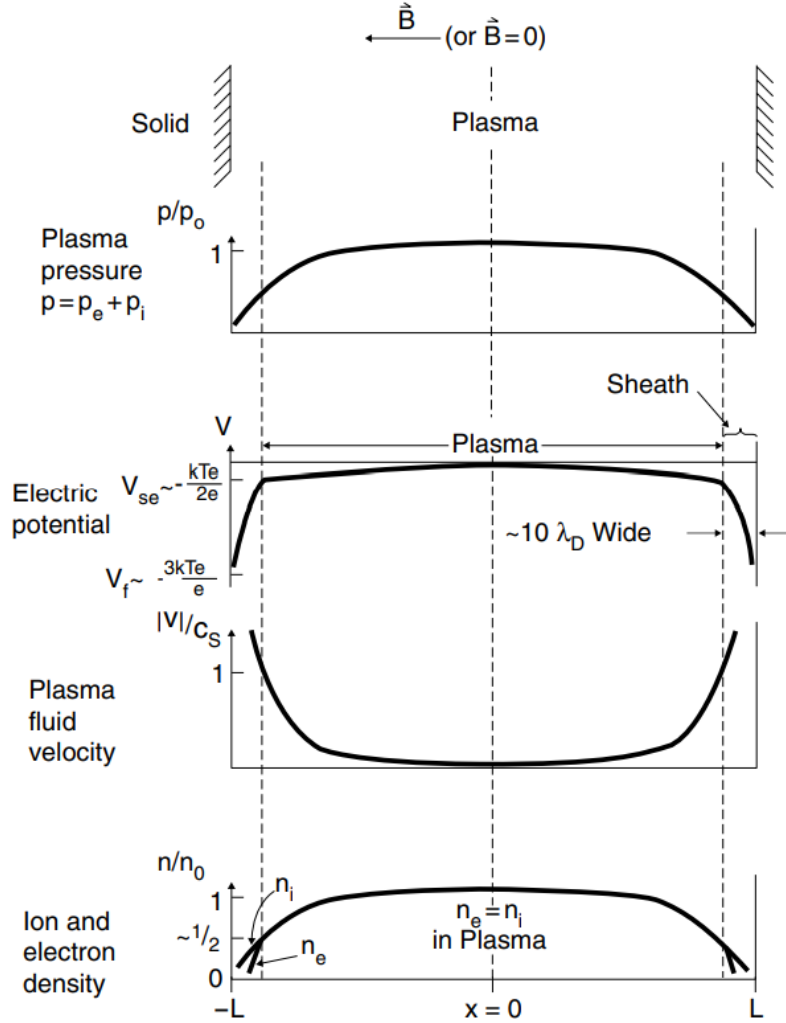
Figure 2.1: Variation of plasma pressure, velocity, densities and electric potential in plasma-wall interaction in the simplest case. Taken from [99].

Despite the simple model described above could provide the main physical insight about the effect of the plasma-wall interaction, a more general analyses could show more complex results. For example, the introduction of a magnetic field oblique to the solid wall surface leads to the formation of the well-known *Chodura* or *magnetic pre-sheath* [72], which acts as an intermediate layer of transition between the pre-sheath and the Debye sheath, respectively dominated by magnetic (as the potential drop is shielded out in the Debye sheath) and electric forces. In addition, also the presence of gradients for different quantities in directions parallel to the wall and strong deviations from thermodynamic equilibrium require a more involved special treatment [82, 99].

Studying the physics of plasma-wall interaction is therefore fundamental to understand how different plasma quantities vary and how this affects particles and heat fluxes. For example particles fluxes can be estimated by knowing particles

velocities and densities, while heat fluxes are estimated by means of *sheath transmission coefficients* which can be computed just by knowing the state of the plasma before entering the plasma-wall transition region [99]. In this way one could link in a consistent way the loads on solid walls to bulk plasma quantities.

2.1.2 *The Effect of Turbulence*

As we've already seen in section 1.2.3, SOL dynamics is characterized by strong non-linearities mainly related to turbulent processes developping on a wide range of spatio-temporal scales. This leads to intermittent transport, dominated by large fluctuations on spatial scales comparable to the one of the system. This doesn't allow for separation of scales in SOL between fluctuations and equilibrium profiles, whose meaning becomes therefore questionable in this context [96].

Fluctuation levels in plasmas grow through instabilities driven by inhomogeneities present both in plasma parameters and electromagnetic fields. Their coupling is able to either drive or suppress turbulence [10]. The randomness of fluctuation-driven processes leads to a "collision-like" diffusion of energy and particles causing a strong enhancement of transport [74]. The ratio between fluctuations and equilibrium values for different plasma quantities tends to increase in edge regions [99]. In addition, in edge plasmas there are evidences that the large collisionality (see section 1.2.3) present in this region plays a crucial role in destabilizing and increasing further these inhomogeneities. Among the wide range of micro-instabilities which can arise in a plasma, this is especially true with respect to the ones related to electrostatic fluctuations inducing drift-motion of particles, which are believed to be the main actor in fluctuation-driven cross-field transport in the SOL [86, 99].

The study of these mutual interactions between inhomogeneities is therefore fundamental to understand the development of turbulent structures and their effect on particles and energy transport [10]. This constitutes the main interest in the field of anomalous transport theory, which is still far from being completely understood and represents one of the major challenges for theoretical plasma physicists. As today a general theory is still not available, two main tools are employed mainly in order to drive research in this field. In first place a large effort has and is still being performed in conducting experiments and collecting information on this topic; this allows to understand empirical scalings between different quantities and confront theoretical predictions with actual results. At the same time, first principle simulations of SOL dynamics (see section 2.3.2) have become an invaluable tool for understanding basic physical processes at play and their increasing role in predicting results for future reactors, beyond plasma regimes currently obtainable in experiments, has become crucial [96].

To understand the importance of turbulent transport, it is useful to compare theoretical results coming from classical or at most neoclassical transport theory with actual experimental results. In general in a tokamak, heat transport coefficients for ions are underestimated by neoclassical transport theory by one order of magnitude. The situation is even worse when it comes to heat transport coefficients for electrons or particles transport coefficients for which the discrepancy between theory and experiments is usually around two orders of magnitude [74]. In addition, the

intermittent nature of turbulent transport causes heat and particles fluxes to be much more localized, both in time and space, than what it'll be predicted by neoclassical transport theory, enhancing the loads related to SOL power exhaust at walls [36].

2.1.3 *The Role of Neutral Species*

The presence of neutral species in the SOL can be due to different sources, the simplest one being *external puffing*, meant as the insertion of an external neutral gas in the fusion reactor through the SOL for different purposes.

Another important process generating neutral species in the SOL is *recycling* at the solid walls. Indeed, a large part of the ions impacting on targets in the SOL remains attached to them, neutralizes with electrons in the solid and gets thermalized. Since the wall is subject to a continuous flux of particles from the plasma, after an initial retention phase, it'll saturate and therefore the charged particles coming from the plasma, after being neutralized and thermalized, will be released back in the plasma as neutrals, where they'll be able to penetrate deep into the SOL thanks to the low plasma temperature [15]. The neutrals coming from the wall will be eventually ionized and therefore this whole chain of processes acts as an important passive re-fuelling mechanism for the plasma.

In any case, this is not the only way the plasma-wall interaction generates neutral species in the SOL. Indeed, also *sputtering* phenomena can occur, distinguished into two main categories. The first kind of sputtering is the physical one, mainly induced by energetic ions impacting on the solid wall and transferring enough momentum for lattice atoms to be ejected. This process presents by definition a threshold energy to be triggered [98]; this energy is provided to ions mainly by the acceleration they experience in the Debye sheath, as seen in section 2.1.1. Another possible sputtering phenomenon, mainly observed with carbon surfaces at walls subject to hydrogenic plasmas [99], is related to the formation of molecules on the solid surfaces, between impacting ions and lattice atoms, having a low enough binding energy which allows them to be released at usual wall temperatures.

In addition to these generation processes, the dynamics of neutral species is strongly affected by the large plethora of atomic and molecular processes which they can have between each other and with plasma species. These processes influence the transport and can act both as sources and sinks of neutral and plasma species in the SOL and they can be quantified and taken into account by knowing their rate coefficients $\langle \sigma v_r \rangle$ (see section 1.1.1) and studying plasma and neutral species evolution. Usually rate coefficients values, or simply cross section values, for different reactions are taken from databases (see [93, 94] as an example) where these data are present, obtained from experimental campaigns.

The kind of processes acting in the SOL and their rates can vary strongly for different plasma and neutral species. As an example, it is interesting to analyze the example of an hydrogen plasma. In figure 2.2 the most important processes are shown together with their rate coefficients presented in figure 2.3. In general, thanks to the lower inertia of electrons, processes involving electron-ion collisions are more important than processes relying on ion-ion collisions as the ratio of their collision rates scales as $\nu_{ie}/\nu_{ii} \sim \sqrt{m_i/m_e}$ [73].

Reaction	Name of the reaction
$e + \text{H} \rightarrow 2e + \text{H}^+$	H Ionization
$e + \text{H}_2 \rightarrow 2e + \text{H}_2{}^+$	H$_2$ Ionization
$e + \text{H}_2 \rightarrow e + 2\,\text{H}$	H$_2$ Dissociation
$e + \text{H}_2 \rightarrow 2e + \text{H} + \text{H}^+$	H$_2$ Dissociative ionization
$e + \text{H}_2{}^+ \rightarrow e + \text{H}^+ + \text{H}^+$	H$_2{}^+$ Dissociative ionization
$e + \text{H}_2{}^+ \rightarrow 2e + \text{H} + \text{H}^+$	H$_2{}^+$ Dissociation
$e + \text{H}_2{}^+ \rightarrow 2\,\text{H}$	H$_2{}^+$ Dissociative recombination
$e + \text{H}^+ \rightarrow \text{H}$	H$^+$ Recombination
$\text{H}^+ + \text{H} \rightarrow \text{H} + \text{H}^+$	H Charge exchange
$\text{H}_2 + \text{H}^+ \rightarrow \text{H}_2 + \text{H}^+$	H$_2$ Elastic collision
$\text{H}_2 + \text{H}^+ \rightarrow \text{H}_2{}^+ + \text{H}$	H$_2$ Ion conversion

Figure 2.2: Most relevant processes for an hydrogen plasma [31].

The importance of neutral species in the SOL is related to different reasons. Among these reasons, we start pointing out that neutrals coming from sputtering of solid targets or externally injected and having large atomic numbers increase dramatically the percentage of radiative power loss, cooling the plasma. While this problem must be taken into account carefully for the core plasma (together with the associated fuel dilution), it may be beneficial for edge regions as it allows to exploit volumetric power losses with radiations and therefore increasing the area on which power loads should be directed [99]. At the same time this is beneficial from the solid targets' side as it decreases sputtering since temperatures near walls reduce together with plasma density. This mechanism is currently being exploited in detached divertor configurations [80] which are currently considered among the best divertor concepts available and they're going to be adopted in near future experiments [8]. Moreover neutral species can play an important role increasing the energy transport and viscosity for ions [49], enhancing anomalous transport [63] and providing efficient energy loss mechanisms for electrons [23].

2.2 THE MULTI-FLUID MODEL FOR EDGE PLASMAS

In this section one of the most used physical models for describing edge plasmas, namely the *Braginskii model*, will be introduced together with its related limits. This will be the foundation of the physical model employed in this thesis.

We start pointing out that the most accurate macroscopic description for plasma dynamics is given by *kinetic theory*. In this approach we study the the *distribution function* $f_a(\mathbf{x}, \mathbf{v}, t)$, which provides the *ensemble average* of particles density in phase space [52]. Its evolution, for any given plasma species a, follows the *Boltzmann equation* [22]

$$\partial_t f_a + \mathbf{v} \cdot \nabla_{\mathbf{x}} f_a + \frac{q_a}{m_a}(\mathbf{E} + \mathbf{v} \times \mathbf{B}) \cdot \nabla_{\mathbf{v}} f_a = C(f_a) \tag{2.4}$$

together with the self-consistent coupling with the evolution of electromagnetic
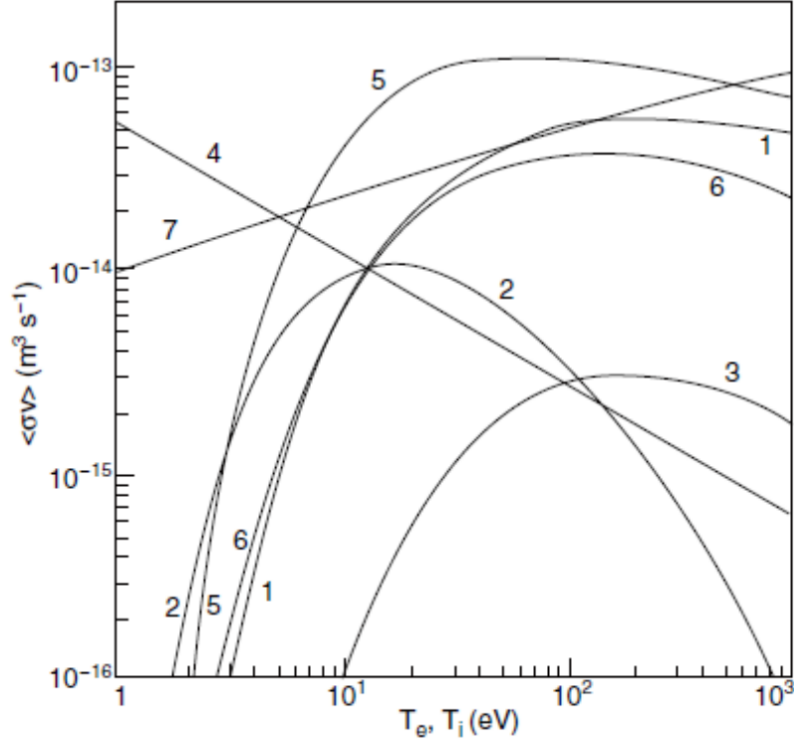
Figure 2.3: Rate coefficients for some of the most important processes for an hydrogen plasma. Taken from [99]. In particular the different numbers refer to: (1) H_2 ionization, (2) H_2 dissociation, (3) H_2 dissociative ionization, (4) H_2^+ dissociative recombination, (5) H_2^+ dissociation, (6) H ionization, (7) charge exchange.

fields as described by the *Maxwell equations*

$$\nabla \cdot \mathbf{E} = 4\pi \rho_{ext} + 4\pi \sum_a q_a \int f_a d\mathbf{v}$$

$$\nabla \times \mathbf{B} = \frac{4\pi}{c}\mathbf{j}_{ext} + \frac{4\pi}{c}\sum_a q_a \int \mathbf{v} f_a d\mathbf{v} + \frac{1}{c}\partial_t \mathbf{E} \qquad (2.5)$$

$$\nabla \cdot \mathbf{B} = 0$$

$$\nabla \times \mathbf{E} = -\frac{1}{c}\partial_t \mathbf{B}$$

where $\mathbf{E}$ and $\mathbf{B}$ are the electric and magnetic field respectively and ρ_{ext} and $\mathbf{j}_{ext}$ are external sources for charge density and current flux not related to any plasma population. The term $C(f_a)$ is the so-called *collision term*, representing collisional effects linked to the microscopical structure of the plasma components [52], and in general it can depend on all the plasma species. This system of coupled non-linear equations is therefore characterized by a high complexity and usually requires very expensive computational approaches to be solved. We further underline that in case the population a is made of neutral particles, the electromagnetic term in equation 2.4 drops and so does its coupling with Maxwell equations. The kinetic description for neutral particles is therefore easier to study, even if it still requires in general

the usage of computational approaches; we refer to sections 3.1.3 and 3.2.3 for the analyses of two possible different approaches for solving neutral particles kinetic equations.

In many situations, including edge plasmas, however a simpler physical model, the *multi-fluid model*, is usually employed being able to still capture the main features of their dynamics. This can be derived starting from kinetic theory when the information related to velocity distributions for different plasma species, contained in f_a, is neglected by multiplying equation 2.4 by suitable quantities $\psi(\mathbf{v}) \sim v_x^l v_y^m v_z^n$ and taking averages in the velocity space [52]. We define $l + m + n$ as the *order* of the related term. The evolution of the system will be therefore described by the evolution of a set of averaged quantities $\langle \psi \rangle_a$ where

$$\langle \psi \rangle_a(\mathbf{x}, t) \equiv \frac{1}{n_a(\mathbf{x}, t)} \int \psi(\mathbf{v}) f_a(\mathbf{x}, \mathbf{v}, t) d\mathbf{v} \tag{2.6}$$

with n_a being the *particles density* for the species a defined as

$$n_a(\mathbf{x}, t) \equiv \int f_a(\mathbf{x}, \mathbf{v}, t) d\mathbf{v} \tag{2.7}$$

With this approach, the following quantities[1] are defined for each plasma species

$\psi(\mathbf{v})$	$\langle \psi \rangle_a$	Name	Dimensions
1	n_a	*particles density*	L^{-3}
$\mathbf{v}$	$\mathbf{u}_a$	*fluid velocity*	$L\,T^{-1}$
$\frac{1}{2} m_a v^2$	E_a	*kinetic energy density*	$E\,L^{-3}$

In particular, E_a is usually decomposed into two contributions as $E_a = 1/2\, m_a n_a u_a^2 + n_a \varepsilon_a$ with the first term being related to the macroscopic fluid kinetic energy while ε_a is the *thermal energy density*, which can be defined as follows and rewritten in terms of the *temperature* T_a or the *pressure* p_a

$$n_a \varepsilon_a = \int |\mathbf{v} - \mathbf{u}_a|^2 f_a(\mathbf{v}) d\mathbf{v} \equiv \frac{3}{2} n_a T_a \equiv \frac{3}{2} p_a \tag{2.8}$$

The fluid approach described above provides therefore a set of 3 equations for each plasma species, describing the evolution of n_a, $\mathbf{u}_a$ and T_a fields, respectively representing conservation of particles, momentum and energy in the plasma system. The equations are the following

$$D_t(n_a) = n_a \langle C_a \rangle_a$$

$$D_t(m_a n_a \mathbf{u_a}) = -\nabla p_a - \nabla \cdot \underline{\underline{\pi_a}} + q_a n_a (\mathbf{E} + \frac{\mathbf{v}}{c} \times \mathbf{B}) + \mathbf{R}_a$$

$$D_t(\frac{3}{2} n_a T_a) = -p_a \nabla \cdot \mathbf{u}_a - \underline{\underline{\pi_a}} : \nabla \mathbf{u_a} - \nabla \cdot \mathbf{q_a} + Q_a \tag{2.9}$$

$$with \quad D_t(g_a) \equiv \partial_t(g_a) + \nabla \cdot (\mathbf{u}_a g_a)$$

with Q_a and $\mathbf{R}_a$ being related to collisions and expressing the heat and the change in momentum transferred in these events respectively. The above equations can't

---

[1]From now on, dependencies on $\mathbf{x}$ and t are intended whenever not directly written.

form a closed set as each of them depends on the next order term $\langle \mathbf{v}\psi \rangle_a$ with respect to the one $\langle \psi \rangle_a$ related to the corresponding equation [52]. Indeed the *conductive heat flux* q_a and *viscous stress tensor* $\underline{\underline{\pi_a}}$, as well as collisions related terms, are in general unknown. The so-called *closure problem* is crucial in providing a link between these quantities and $n_a, \mathbf{u}_a$ and T_a, allowing the actual usage of a fluid approximation. We'll see in the next section how the so-called *Braginskii closure* solves this problem exploiting a set of hypothesis particularly suitable for the description of edge plasmas [69, 96].

2.2.1　*Braginskii Equations*

The Braginskii closure provides expressions for unknown quantities present in equations 2.9 as functions of $n_a, \mathbf{u}_a, T_a$ and other parameters related to each plasma species a, allowing equations 2.9 to form a closed set and be solved. These define a peculiar version of the fluid model also known as the *Braginskii model*. The main hypothesis exploited in its derivation and their final form will be now described. It'll be in particular underlined why this model has found large employment in plasma modeling for the edge regions of fusion reactors. For the full derivation of the model we refer to [69].

Bragisnkii considered a fully ionized ion-electron plasma near local thermal equilibrium. In case multiple ion species are considered, the strategy followed by Braginskii can be still applied. Considering elastic collisions, thanks to particles number, momentum and energy conservation, it holds that [52]

$$\langle C_i \rangle_i = \langle C_e \rangle_e = 0 \qquad \mathbf{R}_{ei} = -\mathbf{R}_{ie} \qquad Q_{ei} + Q_{ie} = -\mathbf{R}_{ei}(\mathbf{u}_e - \mathbf{u}_i) \qquad (2.10)$$

where the label ab refers to the effect on particles from species a due to their collisions with particles from species b. In addition $\mathbf{R}_{ei}$ is usually further split in two contributions: $\mathbf{R}_{\mathbf{u}}$, related to the difference between ions and electrons velocity, and $\mathbf{R}_T$, related to spatial variations in T_e. The same applies for $\mathbf{q}_e$.

As the Braginskii closure holds for plasmas close to thermodynamic equilibrium [69], this implies that the relaxation processes, forcing distribution functions to approach a Maxwellian, must be related to a characteristic time scale, that is the collision time τ, much faster than the time variations of average plasma quantities

$$\frac{d}{dt} \ll \frac{1}{\tau} \qquad (2.11)$$

and that spatial variations of the same quantities are small along excursions of particles after collisions (see section 2.1)

$$\frac{1}{\nabla_\perp} \gg \rho_L \qquad \frac{1}{\nabla_\parallel} \gg l_{mfp} \qquad (2.12)$$

This last requirement on $1/\nabla_\perp$ is in particular valid as long as the magnetic field present in the system is strong enough, that is

$$\Omega_i \, \tau \ll 1 \qquad (2.13)$$

As it can be seen from its description in section 1.2.3, all of the above hypothesis usually hold in the SOL [96].

When a not completely ionized plasma is taken into account, hence the neutral population is not negligible, if the ion-neutral and electron-neutral collision times are much larger than the ion and electron Coulomb collision times, the Braginskii closure can still be applied. This is usually the case in the SOL [15]. In case this hypothesis doesn't apply, a different closure must be employed and this was derived by Helander et al. in [41].

The relation between quantities appearing in equations 2.10, as well as $\mathbf{q}_a$ and $\underline{\underline{\pi}_a}$, and n_a, $\mathbf{u}_a$ and T_a are provided in table 2.1 together with the coefficients appearing in them listed in table 2.2. In the expressions $\mathbf{j} = -en_e\mathbf{u}$ is the plasma current, where $\mathbf{u} = \mathbf{u}_e - \mathbf{u}_i$, and the reference frame is set with the z direction aligned to $\mathbf{B}$, where $\mathbf{b}$ is the magnetic field versor and labels $\parallel$ and $\perp$ are intended with respect to the magnetic field lines directions.

quantity	expression
$\mathbf{R_u}$	$-\frac{m_e n_e}{\tau_e}(0.51\mathbf{u}_\parallel + \mathbf{u}_\perp) = en_e(\frac{\mathbf{j}_\parallel}{\sigma_\parallel} + \frac{\mathbf{j}_\perp}{\sigma_\perp})$
$\mathbf{R}_T$	$-0.71n_e\nabla_\parallel T_e - \frac{3}{2}\frac{n_e}{\omega_e\tau_e}(\mathbf{b} \times \nabla T_e)$
Q_{ie}	$\frac{3m_e}{m_i}\frac{n_e}{\tau_{ei}}(T_e - T_i)$
$\mathbf{q}_\mathbf{u}^e$	$0.71n_e T_e\mathbf{u}_\parallel + \frac{3}{2}\frac{n_e T_e}{\omega_e\tau_e}(\mathbf{b} \times \mathbf{u})$
$\mathbf{q}_T^e$	$-k_\parallel^e\nabla_\parallel T_e - k_\perp^e\nabla_\perp T_e - \frac{5}{2}\frac{n_e T_e}{m_e\omega_e}(\mathbf{b} \times \mathbf{u})$
$\mathbf{q}_i$	$-k_\parallel^i\nabla_\parallel T_i - k_\perp^i\nabla_\perp T_i + \frac{5}{2}\frac{n_i T_i}{m_i\omega_i}(\mathbf{b} \times \nabla T_i)$
π_{zz}	$-\eta_0 W_{zz}$
π_{xx}	$-\frac{\eta_0}{2}(W_{xx} + W_{yy}) - \frac{\eta_1}{2}(W_{xx} - W_{yy}) - \eta_3 W_{xy}$
π_{yy}	$-\frac{\eta_0}{2}(W_{xx} + W_{yy}) - \frac{\eta_1}{2}(W_{xx} - W_{yy}) + \eta_3 W_{xy}$
$\pi_{xy} = \pi_{yx}$	$-\eta_1 W_{xy} + \frac{\eta_3}{2}(W_{xx} - W_{yy})$
$\pi_{xz} = \pi_{zx}$	$-\eta_2 W_{xz} - \eta_4 W_{yz}$
$\pi_{yz} = \pi_{zy}$	$-\eta_2 W_{yz} + \eta_4 W_{xz}$

Table 2.1: Expressions for the Braginskii closure [69].

2.2.2 *Limits of the Braginskii Model*

The Braginskii model introduced in the previous section is often employed in edge plasma modeling despite presenting some limits of applicability.

A first important limit is related to the fact that the Braginskii closure doesn't apply in case some peculiar instabilities are present in the system. These are the

	name	expression
τ_{ab}	$a - b$ particles collision time	$\sim \dfrac{(4\pi\varepsilon_0)^2\sqrt{m_a}\sqrt{T_a^3}}{q_a^2 q_b^2 n_b ln\Lambda_a b}$
$k_\parallel^e$	$\parallel$ electron thermal conductivity	$\dfrac{3.16 n_e T_e \tau_e}{m_e}$
$k_\perp^e$	$\perp$ electron thermal conductivity	$\dfrac{4.66 n_e T_e}{m_e \omega_e^2 \tau_e}$
$k_\parallel^i$	$\parallel$ ion thermal conductivity	$\dfrac{3.9 n_i T_i \tau_i}{m_i}$
$k_\perp^i$	$\perp$ ion thermal conductivity	$\dfrac{2 n_i T_i}{m_i \omega_i^2 \tau_i}$
η_0	-	$0.96 n_i T_i \tau_i$
η_1	-	$\dfrac{3}{10}\dfrac{n_i T_i}{\tau_i \omega_i^2} = \dfrac{1}{4}\eta_2$
η_2	-	$\dfrac{1}{2}\dfrac{n_i T_i}{\omega_i} = \dfrac{1}{2}\eta_3$
$\underline{\underline{W}}$	viscous stress tensor	$(\nabla\mathbf{u}_i + \nabla\mathbf{u}_i^T) - \frac{2}{3}(\nabla\cdot\mathbf{u}_i)\underline{\underline{I}}$

Table 2.2: Coefficients for the Braginskii closure [69]. We adopt the following notation: $\tau_a \equiv \tau_{aa}$.

instabilities characterized by spatial or time scales which are not resolved by the Braginskii model. Indeed, it was already outlined in section 2.1.2 that, in general, random fluctuations can induce strong mixing in the system. This could enhance transport way beyond the values predicted by this model [69]. In any case, the usual spatial and time scales for the most important instabilities occurring in the SOL satisfy the criteria of applicability for the Braginskii closure. They can be therefore, in principle, captured by the model.

Another limitation is related to kinetic effects, arising in particular in the direction parallel to the magnetic field as the particles flow is not constrained by the magnetic field in this direction [56]. This problem can happen in two different situations which we'll see now, together with strategies to tackle it within the frame of the Braginskii approximation:

- Inside plasma sheaths at targets strong distortions from Maxwellian distributions are induced in plasma populations [99] and therefore Braginskii closure can't be applied. In addition, also quasi-neutrality hypothesis breaks down (see section 2.1.1) and, as this is almost always assumed in SOL multi-fluid modeling for practical purposes (see chapter 3), this is a further reason to limit multi-fluid models to work up to the sheath entrance. This indeed means proper boundary conditions must be defined at the sheath entrance in order to provide meaningful results and their choice is dependent on the particular situation considered [82, 99]. As an example, we've already identified two expressions defining ions and electrons velocities at the sheath entrance in the simplest case in section 2.1.1. A more detailed discussion on this topic,

related to the work carried out in this thesis, will be addressed in section 4.3.1.

- When certain conditions on plasma parameters are met so that l_{mfp} becomes comparable with the characteristic dimension of the system in the direction parallel to magnetic fields, the applicability of the Braginskii model is limited and really large unphysical values for plasma fluxes can be predicted. Usually artificial *flux-limits* are applied to upper-bound those fluxes' values while still applying the Braginskii model. An example of this procedure will be discussed in section 3.1.2.

2.3   MULTI-FLUID COMPUTATIONAL APPROACHES

Even if the Braginskii model simplifies the problem with respect to a complete kinetic description, the related set of equations 2.9, together with Maxwell equations, forms a non-linear and coupled partial differential equations system. This implies one needs to rely on numerical approaches to solve these equations.

Different approaches exist in multi-fluid computational modeling for SOL plasmas, all based on Braginskii model with additional simplifications and/or refinements, or similar closures. We can categorize them into two main branches. The first group is *phenomenological* or *mean-field approaches*, which don't aim at recovering a complete physical description of the simulated system, introducing free parameters to be fitted against experimental values in order to evaluate qualitative SOL equilibrium profiles and identify trends for empirical scaling of different quantities which can't be assessed from theory. They are currently the reference tool in SOL modeling, thanks to their reliability, flexibility and relatively lower computational complexity, and they've been largely exploited for designs of important fusion experiments. The second group is *first principle approaches*, which instead aims at providing a complete physical picture of SOL dynamics, within the limits of the employed model, in a self-consistent way, also enabling advances in the understanding of the underlying physical processes characterizing this region. In particular, first principle approaches are able to capture directly turbulence features which are instead neglected or not self-consistently taken into account in mean-field approaches [4, 96].

In the next two sections more details will be provided for each kind of approach, discussing their goals and usage and how these two influences code designs and their features in general. It will be then shown why a possible coupling between the two approaches is nowadays considered interesting by the fusion research community.

2.3.1   *Mean-Field Approach*

In the framework of this thesis, where we focus mainly on physical aspects related to transport, it is important to outline that mean-field approaches describe time-averaged fluxes [51]. Indeed they model radial transport in the SOL, mainly related to turbulence, without self-consistently evaluating fluctuations and resolving temporal scales much larger than the typical ones involved in turbulent phenomena.

For example, they can employ directly models for the anomalous radial transport based on the diffusive approximation with the addition of convective terms related to drifts [51]. Let's consider the particles radial transport, in this case this means they evaluate the radial plasma velocity as

$$\mathbf{v}_\perp = \mathbf{v}_\perp^{drifts} - \sum_a D_{an}^{f_a} \frac{1}{f_a} \partial_r f_a \tag{2.14}$$

where the first contribution is related to drifts in general while the second term is a sum of radial diffusion velocities driven by the variation of different quantities f_a, usually plasma pressure and/or density. Also other similar formulations can be applied. A practical example of this approach will be described in section 3.1.2. Another possibility for mean-field approaches is to separate average values and fluctuations for different quantities and then introduce an averaging procedure, over time scales much longer than the ones characterizing turbulence, on leading equations together with approximations for terms related to different quantities' fluctuations coupling [25]. For example, applying this strategy to continuity equation (see equations 2.9), the advection term would become

$$\nabla \cdot (\langle n \rangle \langle \mathbf{v} \rangle + \langle \tilde{n} \tilde{\mathbf{v}} \rangle) \simeq \nabla \cdot (\langle n \rangle \langle \mathbf{v} \rangle + \mathbf{\Gamma}_\perp^{AN}) \tag{2.15}$$

where we identify with $\langle f \rangle$ and $\tilde{f}$ as the average and fluctuating part of the quantity f respectively and where $\mathbf{\Gamma}_\perp^{AN}$ is a model for $\langle \tilde{n} \tilde{\mathbf{v}} \rangle$ approximating it as a radial particle flux, usually employing also here the diffusion approximation. Mean-field approaches also maintain some free parameters in these models, such as diffusion coefficients for example, so that they can be set accordingly in order to match experimental results.

Mean-field approaches have been used for years as a design tool for important fusion experiments, such as ITER[2], and are still likely to remain the tool of reference for next years in this field.

They are employed for different purposes [51], like for example:

- understanding the basic physics processes

- deriving scalings for various quantities

- integrating all available experimental measurements

and they assist the process of empirical extrapolation, supported by basic theoretical concepts, on which the design of tokamak divertors, limiters and wall systems is mainly based currently [74]. They had also helped pointing out parameters playing a major role in determining SOL profiles and their analysis had an impact on the actual choice for designs in real experiments [4, 78].

As previously said, these computational models contain a number of free parameters representing quantities, mainly related to transport, about which the current state of knowledge proves to be incomplete. Therefore these codes, when run with an interpretative goal, adjust these parameters to fit experimental data in

---

[2]International Thermonuclear Experimental Reactor

the best way. On the other hand, when these codes are employed for predictive purposes, they need empirical relations to be applied and therefore their predicting capabilities are limited by the available experimental data [4]. Since the physical features described self-consistently by mean-field codes are therefore limited with respect to other kinds of codes, they're often coupled to codes addressing a specific physical aspect in particular [96], such as for example codes related to erosion of materials at targets and transport of impurities inside the system.

The radial transport modeling described above and employed by mean-field approaches has deep consequences on the code design which we'll now proceed to explain. First of all, as mean-field codes don't aim at modeling fluctuations and the related asymmetries they can introduce in a physical system, one can exploit symmetries present in the system to reduce the dimensionality of the problem. As an example, this can be done in general in tokamaks with toroidal symmetry [25] or in linear machines with poloidal symmetry [37]. This is the reason why codes based on mean-field approaches usually employ 2D modeling. This point is relevant with respect to the computational complexity of the simulations.

Another great simplification with respect to computational complexity is that, ignoring fluctuations, temporal scales to be resolved in these codes become much larger, as anticipated before. The increase in the resolved time scale passing from first-principle codes, self-consistently accounting for turbulence, to mean-field codes may vary usually between 2 to 4 orders of magnitude [51, 63].

In addition, Monte Carlo codes can be applied to solve kinetic neutrals dynamics in the system. This would have been unfeasible if turbulence would have been directly taken into account in these codes as the typical large noise introduced in the system by Monte Carlo approaches would have spoiled the correlation between fluctuations in the system governing the evolution of turbulence.

In this thesis work we'll employ and refer to SOLPS as an example of state-of-the-art level mean-field code. SOLPS has been the workhorse SOL simulation code for the ITER divertor design [47, 78], but it has also been applied intensively in studies for other devices. Its detailed description will be given in section 3.1.

2.3.2 *First Principle Approach*

First principle computational approaches simulate self-consistently the evolution and the structure of plasma quantities and fields starting from leading equations and resolving typical turbulent time scales. They are able to do this without any separation between average and fluctuating parts for quantities and without introducing any *ad hoc* model to describe transport. The formation of a self-consistent equilibrium in the SOL region is therefore obtained just as a balance between the plasma and energy sources, turbulent transport and losses at targets along field lines [45]. They are not limited in principle to rely on experimental results in their predicting capabilities, as opposite to mean-field approaches as described in the previous section.

In the last years significant progress has been made in the first principle approach to simulate SOL dynamics as the need for their support to mean-field codes is increasingly felt by fusion research community in view of the design of future fusion devices [96]. Thanks to their simulations, first-principle approaches have also helped

in understanding basic physical features underlying SOL turbulence [6, 43]. One of
their aim is therefore also to shed light on main processes at play in the SOL.

Despite being more straightforward from the conceptual side, as they don't
involve any additional assumption apart from the ones done in deriving the employed
physical model, first principle simulations are more complex from the computational
side when compared to mean-field approaches for different reasons.

First principle codes often study fully 3D plasma dynamics in the SOL. Even
if already good results were recovered using 2D fluid turbulence codes [26, 62],
3D effects, such as drift-wave instabilities and magnetic fluctuations, may have a
strong influence on edge turbulence [12]. In general, as they deal self-consistently
with fluctuations which are not reflecting the symmetry of the simulated system,
first principle approaches can't exploit freely symmetries in order to reduce the
dimensionality of the problem at hand.

As they need to follow the evolution of fluctuations and instabilities arising
in the system, first-principle codes need to resolve spatio-temporal scales related
to these physical phenomena. This means they need to resolve scales in space
ranging from the *ion sound Larmor radius* $\rho_s = c_s/\Omega_{Li}$ (usually around $\sim mm$) up
to the system size (usually around $\sim m$) [24] and they need to resolve scales in
time ranging usually from μs up to s [51]. With respect to mean-field approaches,
the time scales range is in particular much larger for first principle codes implying
heavier computational costs.

As the randomness in fluctuations patterns may be influenced in simulations by
the coupling of Monte Carlo routines for neutrals to first principle codes, providing
an additional source of noise in the system, it is usually preferred to avoid using
this solution to evaluate neutrals dynamics. The inclusion of neutral dynamics in
first principle codes is still in its infancy as today [15]. Works with a fluid neutral
model had been reported [21, 40] as well as kinetic models self-consistently evolved
with plasma equations thanks to the method of characteristics [15] (see section
3.2.3).

In this thesis work we'll employ and refer to GBS as an example of state-of-the-art
level first principle code. GBS has been employed mainly to carry out SOL turbulence
simulations of medium size tokamaks and it has helped characterizing non-linear
turbulent regimes and investigating origin and nature of different turbulence-related
physical mechanisms [44]. Its detailed description will be given in section 3.2.

2.3.3   *Complementarity of the Approaches*

As we've outlined in the two previous sections, two main different approaches
exist when it comes to SOL multi-fluid numerical simulations. First principle and
mean field approaches have different goals and this reflects their structural and
conceptual differences. As mean field approaches are more suitable to describe
long time scale, quasi-steady plasma profiles [61], they're the most employed choice
as design tools for fusion reactors. The lack of self-consistency with respect to
transport phenomena otherwise limits their applicability for predicting results
beyond current experimental experience and they can't help in understanding the
nature of transport beyond current theoretical knowledge. In this scenario, the
need for first principle approaches to SOL simulations is increasingly felt [96].

As first principle codes, by their own nature, are more suitable to investigate short time scale phenomena it would be really expensive to run them for longer transport time scales. At the same time the separation of scales between turbulent phenomena and quasi-steady plasma profiles evolution allows mean-field and first principle codes to work on different time scales and a possible coupling between the two methods can be therefore potentially applied [51]. The complementarity of the two approaches is expected to improve mean-field codes results by implementing in them an additional physical feature that they don't self-consistently simulate.

Only a few investigations have been carried out in this direction to our knowledge [51, 61, 63]. Two different strategies for mean-field and first principle codes coupling have been identified in these works:

- *direct coupling* strategy, in which the two kinds of codes are called alternately each providing a set of inputs for the other. In particular the mean-field code can provide profiles of needed quantities to the first principle code, such as directly plasma quantities profiles and the corresponding gradients or sources and sinks for particles and energy. In return, first principle codes are used to evaluate particles and energy fluxes and compute from them effective transport coefficients to be employed by the mean-field code. Despite promising results have been recently obtained with respect to the convergence of this method [63], some authors suggest it is less robust from the numerical stability point of view [51, 61].

- *indirect coupling* strategy, in which a large number of first principle code runs are employed in order to parametrise turbulent fluxes on a given set of parameters and therefore prepare a numerical database beforehand for effective transport coefficients and their dependencies on the investigated parameters. It is therefore crucial to know in advance the parameters to be investigated in the parametrisation and to be able to reproduce from scratch meaningful plasma profiles for the situation of interest with the first principle code. The biggest advantage of this method is in its increased numerical stability. At the same time large number of parameters scans may prove extremely expensive from the computational side if a lot of dependencies are expected for the transport coefficients. [51, 61].

2.4 Modeling of Linear Plasma Devices

We have already underlined in section 1.3 the important role of linear plasma devices in magnetically confined fusion research and their similarities with SOL regions in fusion reactors.

Despite their extensive deployment in experimental investigations, the application of multi-fluid codes for SOL simulations on linear machines has been only seldom exploited and the corresponding literature is limited. This is mainly because, as these codes are originally meant to simulate tokamak machines, they're quite not optimized for linear geometries and peculiar solutions must be adopted and/or additional features must be introduced.

Among the few studies carried out in this context, for example, we recall:

- for mean-field approaches: (a) SOLPS simulations of the GyM linear device, with the aim of performing sensitivity scans for different parameters and comparisons with experimental results [23, 37], and of MAGPIE, to study radial transport [34], (b) B2-EIRENE simulations of MPEX, to study the feasibility to reach target densities similar to those expected with burning plasmas [28], and of Magnum-PSI, to underline the role of neutral species on plasma profiles [35], (c) SOLEDGE2D-EIRENE code has been applied to Pilot-PSI to study the role of atomic and molecular processes in plasmas also in comparison with experimental results [32].

- for first-principle approaches: (a) 3D two-fluid turbulent simulations, based on the Braginskii model, of the LAPD machine, to explore plasma turbulence features [14], (b) the BOUT++ code was applied for simulations of the CSDX linear plasma device, to study the impact of insulating and conductive endplates on turbulence [46], and of the LAPD machine, to study its energy dynamics and to compare experimental results with simulated turbulent profiles [13, 54].

Within the framework of this thesis, we'll focus on the *Gyrotron Machine*, or simply *GyM*, which is a linear plasma device designed and built by ISTP (Institute for Plasma Science and Technology) in Milan, Italy. As mentioned in section 1.3, it is employed in studies of both elementary plasma physics phenomena and plasma material interactions in the context of magnetically confined nuclear fusion research [76].

Its structure is presented in figure 2.5 together with its most relevant dimensions in figure 2.4. The axial magnetic field is produced by 10 azimuthal coils which are placed around the vacuum vessel, each one composed by 36 copper windings carrying a current which can be varied up to 1000 A. In figure 2.5 one can also see the positions of other important components of the machine:

- the diagnostic system, represented by a Langmuir probe with which electron temperature, density and plasma potential can be measured.

- the pressure meter, to measure the neutral gas pressure inside the chamber.

- the two ducts, at the end of which there are the pumps to keep the system in high-vacuum conditions.

- the gas puffing system, to inject neutral gas into the chamber.

- a 3 kW radio frequency (RF) source to generate and heat up the plasma.

- the sample holder for fusion-relevant materials exposure.

The plasma is generated inside the chamber exploiting the *electron cyclotron resonance heating*, or simply *ECRH*, mechanism with the RF source exciting free electrons and providing them enough energy to ionize neutral particles injected by the puffing system. More details on the modeling of the *ECRH* energy source will be provided in section 4.2.2. A complete description of the simulation setup considered in this thesis and its modeling, will be provided in section 4.1.

Dimension	[cm]
Cylindrical vacuum chamber length	205.8
Cylindrical vacuum chamber internal diameter	25.0
Total length, from coil 1 to coil 10	276.6
Coil external diameter	83.0
Coil internal diameter	55.2
Coil width	9.2

Figure 2.4: Most relevant dimensions for the GyM machine.
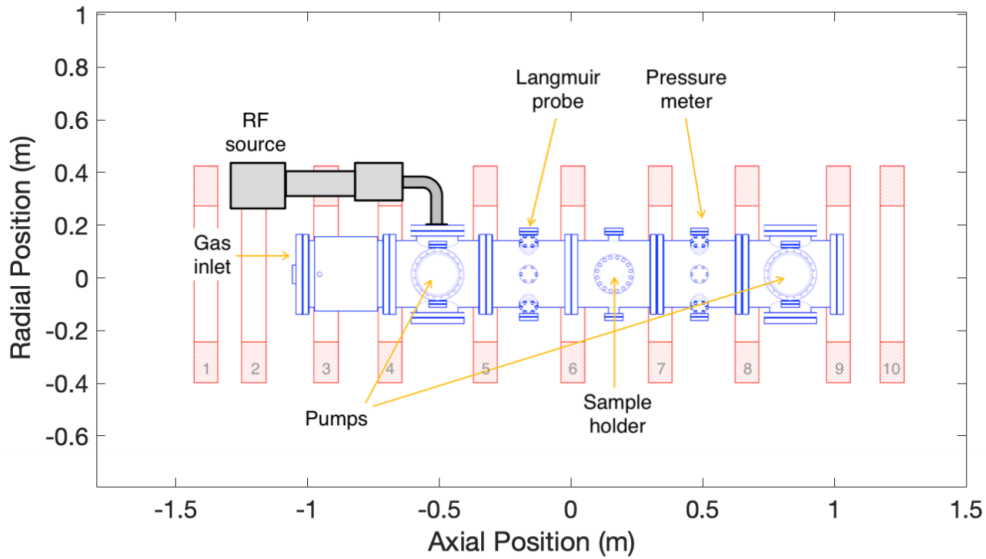
Figure 2.5: GyM machine structure.

As already said, GyM has been already subject to simulation studies with SOLPS code [23, 37], coherently adapted to run in a linear plasma device configuration. Among the different results obtained, they have shown the effects on main plasma quantities of different parameters, namely absorbed power, pumping efficiency and effective transport coefficients. They've also investigated quantitatively the role of different mechanisms in particles and energy balances in the system shedding light on their relative importance.

2.5 MOTIVATION AND SCOPE OF THE WORK

A brief resume is displayed here as a recap for the elements presented in the first two chapters. These elements are meant to provide the general basis to understand the motivations and the goal of this thesis work.
In chapter 1 we started with a general overview regarding the interest in nuclear fusion for power production. Then we presented one of the main challenges currently limiting its development, namely the power exhaust and first wall design problem.

We've also analyzed the general characteristics of the SOL, the plasma region in the reactor which mediates the interaction between the bulk plasma and solid walls in the chamber and controls power exhaust. Finally, we underlined the important role linear plasma devices have in nuclear fusion research and SOL-related studies. In chapter 2 we focused more on the physical description of the SOL. Transport phenomena have been described in detail in order to underline the main actors affecting them; in particular we've emphasized the role of turbulence in this context. The multi-fluid model, together with a suitable closure applying in the SOL region, and its limits were presented as a reasonable way to describe SOL dynamics. This also pointed out the need for computational tools to tackle the problem and we recognized and confronted two main approaches in this direction, the mean-field and the first principle ones. It was also highlighted how they can be complementary and how they could be coupled in a direct or in an indirect way. In addition the modeling question was also addressed for linear plasma machines discussing their related specific issues and presenting in detail one example of these devices, namely the GyM machine.

This thesis work has been developed in the framework of numerical investigations of nuclear fusion relevant plasmas in linear plasma devices, through the usage of dedicated multi-fluid codes specific for SOL conditions. These computational tools are playing a fundamental role in nuclear fusion research as they support experimental results interpretation and they help predicting future devices' performances. One of the most employed codes in this field is SOLPS, which is the reference tool for the design of the ITER machine, the most important nuclear fusion project worldwide. SOLPS has already been also exploited on linear machines and in particular on the GyM machine. SOLPS is a state-of-the-art level example of a mean-field code and therefore it presents their characteristic limits: it relies largely on experimental results to assess transport properties of the simulated system as it can't self-consistently capture the effect of turbulence. Therefore its predicting capabilities beyond experimental experience and the possibility of exploiting it to study the underlying physical mechanisms in plasma profiles evolution are limited. These limits may prove to be important in the framework of linear plasma machines simulations due to the corresponding limited literature available and their studies of plasma scenarios currently never approached experimentally in fusion reactors. In addition, when employed in a linear configuration, SOLPS can't include plasma drifts in its physical model, as it'll be explained in section 3.1.2.. Codes relying instead on the first-principle approach could support SOLPS by providing it directly reliable information about transport properties of the simulated system, as they can solve self-consistently turbulent profiles. A coupling strategy is therefore reasonable in this picture and we decided to consider the GBS code for this purpose. GBS is a state-of-the-art level example of a first principle code and it has been exploited mainly on medium-size tokamaks up to now, helping in understanding the physics governing SOL-related phenomena. In order to employ GBS for this role, it must be modified coherently to be adapted to a linear plasma machine configuration. In addition, GBS can be also used to recover information about plasma drifts in this simulation setup, missing in the SOLPS analyses.

The main goal of this thesis is therefore to perform a preliminary investigation of this coupling strategy between SOLPS and GBS for the simulation of the GyM

linear plasma device. An He plasma with relatively low density will be considered for the simulations, characterized by plasma quantities values which are realistic for the GyM machine. We underline that He plasmas are currently an important topic in nuclear fusion research and, for example, they'll play a major role in the next pre-power operation phase in the ITER experiment [38]. The first important result which needs to be obtained in this direction is the adaption of GBS to a linear plasma device configuration. This will be done by modifying directly the GBS code: limitations related to the intrinsic assumption of a tokamak geometry in the code will be removed and suitable modifications will be introduced, allowing it to treat linear configurations. Nevertheless, some approximations will still be present in the application of this modified GBS code to a linear plasma device, among which the lack of self-consistent neutrals dynamics evolution. Once this step will have been performed, actual simulations will be carried out with SOLPS and GBS together with the required post-processing. The adopted coupling strategy will follow a direct approach, meaning that the two codes will be called iteratively providing each other needed inputs. In particular, an initial SOLPS simulation will be performed, employing values obtained from previous literature studies to set free parameters related to effective diffusion coefficients. Its results will be exploited then to build up important neutrals-related sources for the GBS simulation. The GBS simulation will be then run and its results will be analyzed. Particular attention will be drawn to turbulent profiles and also to plasma drifts velocities profiles. From its post-processing, self-consistent values for the same diffusion coefficients will be extracted and employed in the next SOLPS simulation, whose results will be compared to those of the previous one. The outcome of this work will help us in understanding the criticalities associated to this strategy and in pointing out perspectives and needed refinements for potential future developments.

In the following, more details on SOLPS and GBS will be provided in chapter 3, focusing on aspects related to the geometries they can take into account and the way they model plasma and neutrals dynamics. The description of the simulation setup will be then the subject of chapter 4, together with specific points and approximations which characterize the modeling of the GyM linear device for each of the two codes. In addition, the modifications which were carried out on the GBS code to adapt it to linear configurations will be also presented there. Actual results from the simulations carried out with the two codes will be shown in chapter 5, focusing also on the description of the coupling approach between SOLPS and GBS and on the details of their post-processing needed to build up inputs for each other. Finally, in chapter 6, conclusions on obtained outcomes are drawn and perspectives and possible refinements for future works are identified.

CHAPTER 3

Codes for Scrape-Off Layer Simulations

In chapter 2 the need for computational tools to address the investigation of edge plasma physics and plasma wall interaction was presented. We've also seen in section 2.3 that two main approaches are employed for this task, underlining their differences and their characteristic features, as well as possible coupling strategies. In this thesis work two codes had been used, each of them representing one of the two above mentioned approaches: SOLPS for the mean-field approach and GBS for the first-principle approach.

In this chapter, for each of them a detailed description will be provided. After a brief introduction and a brief description of their structures, the kind of geometry implemented in each code will be presented (§3.1.1; §3.2.1). Then the physical model describing the plasma species dynamics employed in each code is illustrated together with the related numerical scheme needed to solve the corresponding set of equations (§3.1.2; §3.2.2). The same will be done also for neutral species dynamics (§3.1.3; §3.2.3).

Additional technical aspects about GBS code spatial discretization will be introduced (§3.2.4), mainly referring to issues related with code parallelization and boundary conditions imposition. This section will be useful for the understanding of the modifications which were applied to the GBS code in order to apply it to a linear plasma device configuration (see section 4.3).

It is important to underline here that the level of detailed knowledge required for working with the two different codes in this thesis work was not the same. A deep analysis of the GBS code was carried out, related to its physics, its numerics and other technical aspects, in order to be able to modify it, apply it to linear configuration and underline its limits in this application and possible future refinements. At the same time, for SOLPS the code was already ready to be employed in linear configurations and its analysis was carried out just from a user-perspective restricted to the considered simulation setup. Hence its description in the following will be limited just to the aspects needed for this thesis work and we refer to [18, 53] for a complete report on SOLPS.

3.1   SOLPS-ITER code

The SOLPS code is a code package which has found large employment in the development of the ITER experiment. Its two main packages, B2.5 and EIRENE, described in the following, have been developed by different institutes: B2.5 by KU Leuven, IPP Garching and Saint Petersburg State University, while EIRENE by FZ Julich. SOLPS is the reference for mean-field approaches in SOL simulations at the current state-of-the-art. Its latest version, more precisely addressed as *SOLPS-ITER* [53], couples the most recent MPI parallelized version of the EIRENE code (see section 3.1.3), for kinetic neutral species description, with the B2.5 plasma solver code (see section 3.1.2), for multi-fluid plasma species description.

The first version of the code was originally developed by B. Braams during his Ph.D. thesis [68] and then improved and firstly coupled with the EIRENE Monte Carlo code by M.Baelmans during her PhD thesis [65]. The model proposed by Braams and Baelmans has been improved in the following years as several mechanisms, originally neglected in the adopted plasma physics modeling, such as currents and drifts, have been added to the code by different groups. Regarding the EIRENE code, the first version was presented in 1992 [95] and also in this case, many updates have been introduced since then. In particular, the latest version includes: large variety of many atomic and molecular processes (also thanks to the development of specific external databases), the possibility to simulate radiation losses and the neutral-neutral and photon-neutral non linear collision processes and the possibility to run the code using the parallelized version, in order to strongly reduce the computation time.

SOLPS can be employed both in *standalone* or *coupled* mode. Standalone runs imply either only B2.5 equations or only EIRENE equations are solved. In the first case both plasma and neutral species are treated with a multi-fluid approach. In the second case neutral species dynamics are treated kinetically over a fixed plasma background. Nevertheless in this thesis work we'll focus on the coupled mode for SOLPS simulations. Charged plasma species are described using the fluid model, while the transport of neutral species and their interaction with plasma particles is implemented by means of a Monte Carlo method in EIRENE. The latest version of the EIRENE code allows to take into account not only atoms, but also molecules and molecular ions. To suitably describe all the relevant collision processes, databases like HYDHEL [94] and AMJUEL [93] for atomic and molecular processes are used. The possibility offered by the SOLPS code to simulate impurities requires other two elements: (a) the introduction of models for the impurities production by physical and chemical sputtering [16] according to the wall composition; (b) dedicated databases, describing collision processes among a given impurity family, such as hydrocarbons [19], and plasma particles. The sputtering yield is usually computed by EIRENE from the TRIM (TRansport of Ions in Matter) code. The iterative coupling procedure between B2.5 and EIRENE consists in the following steps:

1. preparation of the numerical grid structures for the two codes.

2. computation of the source and sink terms into the fluid balance equations for each plasma species from Monte Carlo routines on neutrals.

3. solution of the plasma balance equations in terms of density, velocities and temperatures

4. update of the plasma background, which is used to evaluate the collision terms in the second step.

The SOLPS code includes multiple packages which are needed for different tasks, such as the implementation of equilibrium magnetic fields in the configuration and the preparation of the different grids employed in B2.5 and EIRENE. In addition, different MATLAB scripts and commands has also been developed for post-processing. In this thesis work we'll focus only on the description of the two packages related to the physical modelling employed in SOLPS, B2.5 and EIRENE, respectively in section 3.1.2 and 3.1.3.

3.1.1 *Geometry*

As a mean-field approach code, SOLPS is able to exploit symmetries in the system to reduce the dimensionality of the physical problem (see section 2.3.1). Thanks to this possibility, SOLPS is meant to solve a reduced set of 2D equations exploiting rotational symmetries in the system, thus reducing the domain of interest for the simulations to a single cross section plane parallel to the corresponding axis of rotation. As SOLPS has been originally developed to be applied on tokamaks, its natural simulation setup is a poloidal cross section of a tokamak machine exploiting the toroidal symmetry in the system. Nonetheless, the same idea can be applied on a linear plasma device exploiting the polar symmetry in the system and in this case the simulation domain becomes a plane parallel to the cylinder axis spanning from the center of the machine to its external radius. In SOLPS the direction of rotational symmetry is defined by a unit vector $\mathbf{e}_z$. Other two unit vectors are usually employed to define the bi-dimensional simulation domain: $\mathbf{e}_y$, which is orthogonal to the magnetic flux surfaces on the bi-dimensional simulation domain, and $\mathbf{e}_x$, which is along the projection of $\mathbf{B}$ on the bi-dimensional simulation domain. These three unit vectors forms the so-called *geometrical reference frame* in SOLPS. The representation of the geometrical reference frame together with simulation domains in a tokamak and in a linear plasma device can be seen in figure 3.1.

Another coordinate system is also used in SOLPS. This is the *dynamical reference frame* which is constituted by the following set of three orthogonal unit vectors: the same $\mathbf{e}_y$ employed in the geometrical frame, $\mathbf{e}_\parallel$ in the direction along $\mathbf{B}$ and $\mathbf{e}_\perp$ which becomes tangent to the corresponding flux surface and orthogonal to $\mathbf{B}$. This coordinate system follows the characteristic plasma motion. The difference between the geometrical and the dynamical reference frames in the case of a tokamak machine can be seen in figure 3.2. The dynamical reference frame is best suited to build the equations of motions for the plasma species.

The equilibrium magnetic field can be loaded in SOLPS by uploading the equilibrium 2D map of the magnetic field flux function ψ on the bi-dimensional simulation domain. This can be also imported from external files. This equilibrium configuration is required to intersect the solid walls of the machine considered just at two solid targets. These are the divertor targets for X-point tokamak configuration for which SOLPS has been originally developed, but they can also represent the two
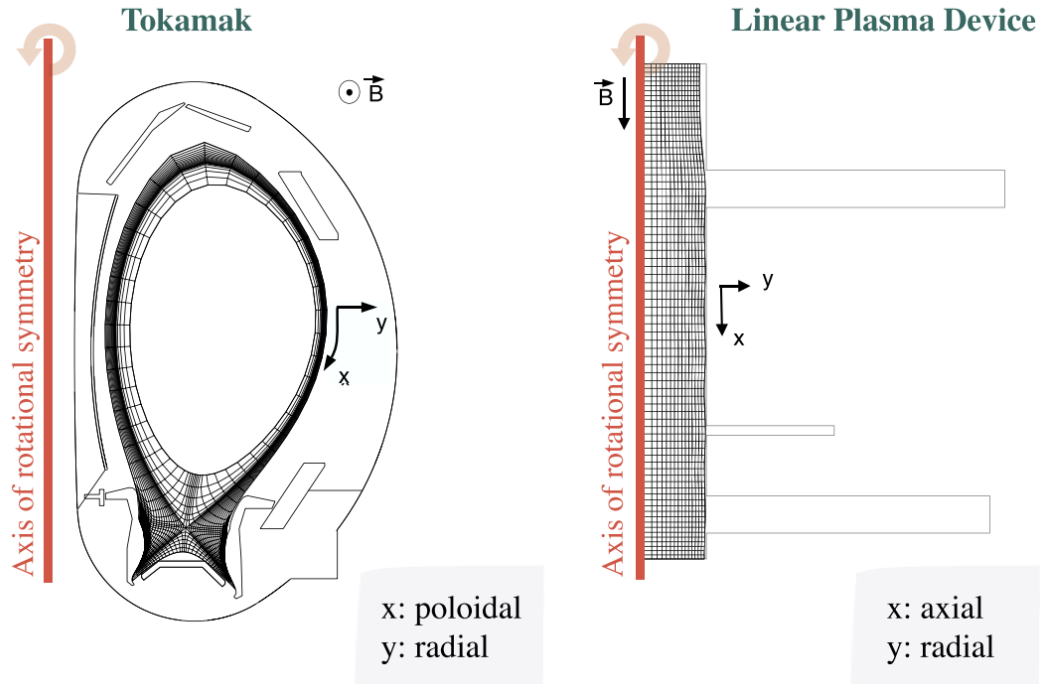
Figure 3.1: Geometrical reference frame in a tokamak and in a linear plasma device (in particular, the GyM machine). In both cases the z direction can be ignored as rotational symmetry around the axis reported in red is assumed. Taken from [37].
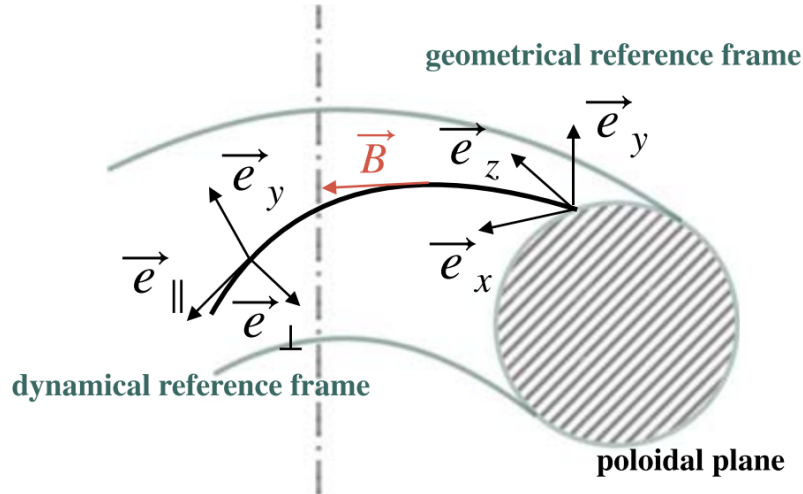
Figure 3.2: Geometrical and dynamical reference frames in a tokamak machine. Taken from [37].

axial targets in a linear plasma device configuration. This requirement implies the magnetic field doesn't intercept any other solid wall but the two defined targets. The cross section of the solid walls of the machine considered must be also loaded in SOLPS, both from available SOLPS databases or from external technical drawing files. From the equilibrium magnetic field and the machine solid walls cross section

the meshes for B2.5 and EIRENE can be built.

The B2.5 mesh is a curvilinear rectangular field-aligned grid where two sides of the mesh cells are aligned to magnetic field lines. The resolution of the grid can be chosen by the user. As the equilibrium magnetic field doesn't intercept any solid wall but the two defined targets, in both tokamak and linear plasma device configurations the B2.5 mesh doesn't extend up to the solid walls in the radial direction. This mesh defines the so-called *physical domain* for plasma species simulations while numerical calculations are carried out in the so-called *computational domain*, which is a topologically rectangular mesh obtained from the physical domain. As an example, in figure 3.3 the corresponding physical and computational domains for an X-point tokamak configuration is displayed. The transformation between the two domains can be carried out with the usage of suitable metrics coefficients.

As opposite, the EIRENE mesh is a triangular mesh which is now extending from the B2.5 mesh up to the machine solid walls. This is built from a triangularization of the B2.5 mesh and at the same time a triangularization of the remaining vacuum region up to the machine walls. The merging of these two elements provides the final form of the EIRENE mesh. As a reference, in figure 3.4 the EIRENE mesh is displayed again for an X-point tokamak configuration.

3.1.2 *B2.5 Package for Plasma Species*

B2.5 is, together with EIRENE, one of the two fundamental packages of SOLPS. It solves the plasma species dynamics by means of a multi-fluid mean-field approach. Its code is entirely written in FORTRAN 90 and its numerical scheme is based on the *finite volume discretization* method. At each time step, volumetric and surface source terms are computed and used to solve momentum, density and energy conservation equations. This procedure is carried out for a number of internal iterations, whose convergence is checked by monitoring the norm of the residual for each conservation equation, to relax the solutions before proceeding to the next time step. The time evolution stops when a steady state is reached, where no major variation in time of the plasma parameters is observed. By means of some input files written in ASCII format the user can specify the geometry, the initial conditions, the boundary conditions and other physical parameters for the simulation such as for example the resolution of the mesh, the sources in the system and the transport coefficients.

In B2.5 the transport equations will be rewritten in curvilinear coordinates. For this reason one needs to introduce the metric coefficients h_x, h_y, h_z and $g = (h_x h_y h_z)^2$ with respect to the geometrical reference frame[1]. It is also useful to introduce here the normalized components of the magnetic field $b_x = B_x/B$ and $b_z = B_z/B$. The full derivation of the transport equations in curvilinear coordinates can be found in [65] for the simpler original model neglecting radial drifts.

Considering a plasma with a single ion species and a given external magnetic field which is static and known, assuming quasi-neutrality, the plasma transport problem has ten unknowns: the ion density, ion and electron temperatures, the three components of ion velocity, the three components of the current density vector

---

[1]Here and later in this section I will make use of the notation introduced in section 3.1.1.

(a) *Physical mesh of B2.5.*

(b) *Computational mesh of B2.5.*

(c) *Regions on the physical mesh.*

(d) *Regions on the computational mesh.*
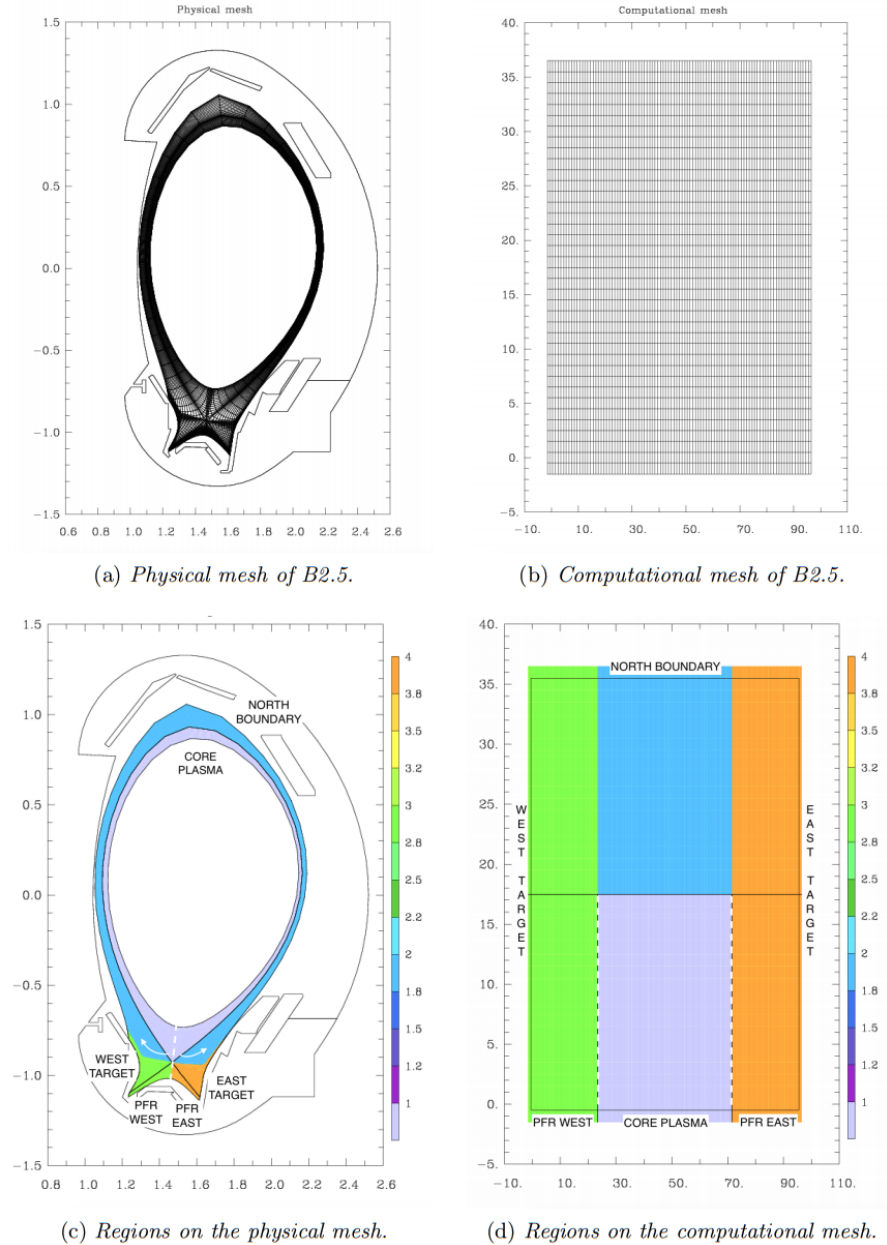
Figure 3.3: Physical and computational domains for an X-point tokamak configuration simulation in SOLPS. Taken from [100].

and the electrostatic potential. The corresponding ten equations to be solved are those represented in the system of equations 2.9 together with the Poisson equation.

Parallel transport coefficients are assumed to be classical and Braginskii closure is employed in this direction, eventually corrected with the flux-limits approach when kinetic effects become important (see section 2.2.2). Taking as an example parallel heat conductivity, the flux-limits approach [51] imposes

$$k_\parallel = \frac{k_{cl}}{1 + |q_{cl}/q_{fl}|} \tag{3.1}$$

where k_{cl} is any chosen classical formulation for heat conductivity, $q_{cl} = -k_{cl}\partial_\parallel T$ is
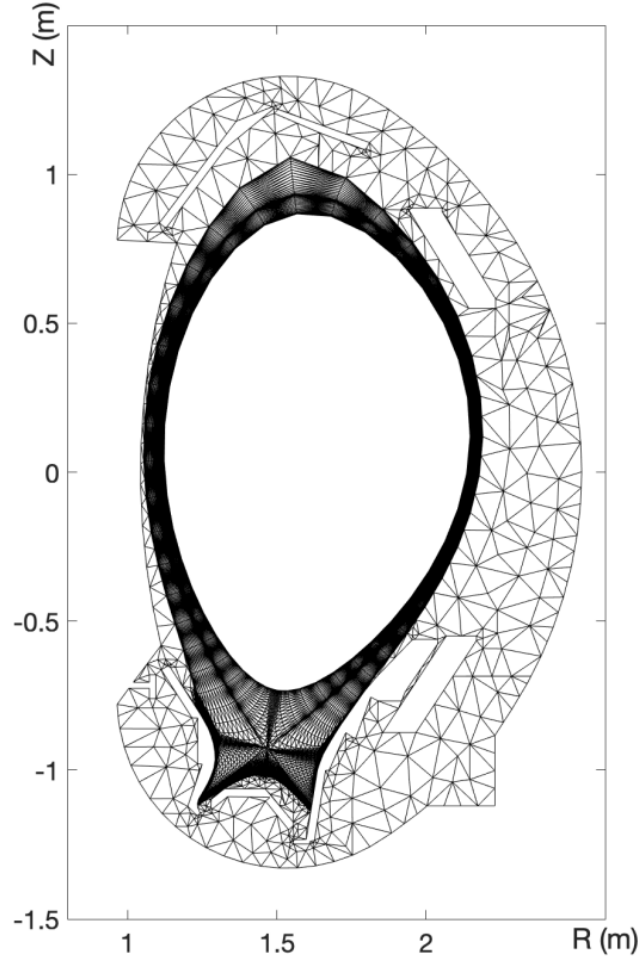
Figure 3.4: Eirene triangular mesh for an X-point tokamak configuration. It can be observed this mesh is obtained by merging a triangularization of the corresponding B2.5 mesh for this configuration (see figure 3.3) and of the remaining vacuum region up to the solid walls.

the classical heat flux and $q_{fl} = \alpha n_e T_e^{3/2} \sqrt{m_e}$ is the limited flux, with α being an arbitrary scaling factor.

As opposite, cross-field transport is instead assumed to be anomalous and corresponding transport coefficients can be specified by the user from input files. These parameters are usually fitted against experimental data (see section 2.3.1) and aren't self-consistently evaluated. Indeed SOLPS is not able to solve turbulent transport and it approximates perpendicular motion of the plasma with a superposition of drifts due to different forces and artificial effective diffusion terms [65]. To show this, let's take the cross product between momentum balance equation for ions in 2.9 and the unit vector $\mathbf{b} = \mathbf{B}/B$ and then project the results on both the y and the perpendicular direction. If one considers the Braginskii expression for the friction force then the result is

$$\mathbf{V}_\perp = \mathbf{V}_\perp^a + \mathbf{V}_\perp^{dia} + \mathbf{V}_\perp^{in} + \mathbf{V}_\perp^{vis} + \mathbf{V}_\perp^s \tag{3.2}$$

$$\mathbf{V}_y = \mathbf{V}_y^a + \mathbf{V}_y^{dia} + \mathbf{V}_y^{in} + \mathbf{V}_y^{vis} + \mathbf{V}_y^s \tag{3.3}$$

$\mathbf{V}^a$ is the so-called *ambipolar velocity.* This contribution is charge-independent and identical for ions and electrons. In this contribution the effective diffusion terms are implemented both in terms of density and pressure variation if anomalous transport is considered [51]. Therefore the most general form for $\mathbf{V}^a$ is

$$\mathbf{V}^a_\perp = \mathbf{V}^{\mathbf{E}\times\mathbf{B}}_\perp - \frac{D}{T_e + T_i}\frac{b_z}{h_x}\left(\frac{1}{n}\partial_x p - \frac{3}{2}\partial_x T_e\right) - D^n_{AN}\frac{1}{h_x n}\partial_x n - D^p_{AN}\frac{1}{h_x n}\partial_x p \quad (3.4)$$

$$\mathbf{V}^a_y = \mathbf{V}^{\mathbf{E}\times\mathbf{B}}_y - \frac{D}{T_e + T_i}\frac{1}{h_y}\left(\frac{1}{n}\partial_y p - \frac{3}{2}\partial_y T_e\right) - D^n_{AN}\frac{1}{h_y n}\partial_y n - D^p_{AN}\frac{1}{h_y n}\partial_y p \quad (3.5)$$

where $D^{p,n}_{AN}$ are the anomalous diffusion coefficients for respectively pressure and density-driven diffusion velocities and $D = (T_e + T_i)\nu_{ei}/eb\omega_{ei}$ is the classical diffusion coefficient. The other terms appearing in the previous equations are

- the *diamagnetic velocity*

$$\mathbf{V}^{dia}_\perp = -\frac{1}{enB}\frac{1}{h_y}\partial_y(nT_i) \qquad \mathbf{V}^{dia}_y = -\frac{b_z}{enB}\frac{1}{h_x}\partial_x(nT_i) \qquad (3.6)$$

- the $\mathbf{E}\times\mathbf{B}$ *velocity*

$$\mathbf{V}^{\mathbf{E}\times\mathbf{B}}_\perp = -\frac{1}{B}\frac{1}{h_y}\partial_y\Phi \qquad \mathbf{V}^{\mathbf{E}\times\mathbf{B}}_y = -\frac{b_z}{B}\frac{1}{h_x}\partial_x\Phi \qquad (3.7)$$

- the non-ambipolar velocities terms caused respectively by inertia, viscosity and ion-neutral friction expressed in terms of the related currents

$$\mathbf{V}^{in} = \frac{\mathbf{j}^{in}}{en} \qquad \mathbf{V}^{vis} = \frac{\mathbf{j}^{vis}}{en} \qquad \mathbf{V}^s = \frac{\mathbf{j}^s}{en} \qquad (3.8)$$

In addition one can also rewrite $\mathbf{V}_x = b_z\mathbf{V}_\perp + b_x\mathbf{V}_\parallel$.

With these terms being defined the transport equations can be rewritten in the following way:

- the continuity equation becomes

$$\partial_t n + \frac{1}{\sqrt{g}}\partial_x\left(\frac{\sqrt{g}}{h_x}n(b_x V_\parallel + b_z V_\perp)\right) + \frac{1}{\sqrt{g}}\partial_y\left(\frac{\sqrt{g}}{h_y}nV_y\right) = S_n \qquad (3.9)$$

with S_n being the ionization source in the system.

- the ion parallel momentum equation, obtained taking the component in the **b** direction of the corresponding balance equation, is further simplified by many assumptions on the relative importance of the different contributions

to velocities and their associated fluxes [57, 58] and becomes

$$m_i[\partial_t(nV_\parallel) + \frac{1}{h_z\sqrt{g}}\partial_x(\frac{h_z\sqrt{g}}{h_x}n(V_\perp b_z + V_\parallel b_x)V_\parallel)$$

$$+ \frac{1}{h_z\sqrt{g}}\partial_y(\frac{h_z\sqrt{g}}{h_y}nV_yV_\parallel)] =$$

$$= -\frac{b_x}{h_x}\partial_x(nT_i) - b_x\frac{en}{h_x}\partial_x\Phi + F_k +$$

$$+ \frac{4}{3}b_xB^{3/2}\frac{1}{h_x}\partial_x[\frac{\eta_0 b_x}{B^2}\frac{1}{h_x}\partial_x(\sqrt{B}(V_\parallel + b_xV_\perp^{dia} + b_xV_\perp^{\mathbf{E}\times\mathbf{B}}))] + \qquad (3.10)$$

$$+ B^{3/2}b_x\frac{1}{h_x}\partial_x[\frac{b_x}{\nu_{ii}B^2}\frac{1}{h_x}\partial_x[\sqrt{B}(q_{i,\parallel} + b_xq_{i,x}^{dia})]] +$$

$$+ \frac{1}{h_z\sqrt{g}}\partial_y(\frac{h_z\sqrt{g}}{h_y^2}\eta_2\partial_yV_\parallel) + \frac{1}{h_z\sqrt{g}}\partial_x(\frac{h_z\sqrt{g}}{h_x^2}\eta_2\partial_xV_\parallel) +$$

$$+ S_\parallel^m + R_{ei,\parallel}$$

where F_k is the Coriolis force. The fifth term in the RHS of the above equation is not present in the classical Braginskii closure and it accounts for a neoclassical correction of the parallel Braginskii viscosity arising in a tokamak toroidal geometry. At the same time η_2, the classical perpendicular viscosity, is usually replaced by the anomalous value $\eta_2 = m_i n D_{AN}$. Finally $S_\parallel^m$ is the momentum loss due to ion-neutrals interaction or neutral beam injection and $R_{ei,\parallel}$ is the classical Braginskii electron-ion friction term.

- the electron momentum equation is simplified neglecting the electron inertia and obtaining the so-called *generalized Ohm law* [56] for the parallel current

$$j_\parallel = \sigma_\parallel[\frac{b_x}{e}\frac{1}{h_x}(\frac{1}{n}\partial_x(nT_e) + 0.71\partial_xT_e) - \frac{b_x}{h_x}\partial_x\Phi] \qquad (3.11)$$

Besides $j_\parallel$, to compute the full current $\mathbf{j}$, other contributions are needed

$$\mathbf{j} = \mathbf{j}^{dia} + \mathbf{j}^{in} + \mathbf{j}^{vis} + \mathbf{j}^s + \mathbf{j}_\parallel \qquad (3.12)$$

which can be obtained from the current continuity equation. We refer to [18, 57, 58] for a full derivation of each term.

- The electron energy balance becomes

$$\frac{3}{2}\partial_t(nT_e) + \frac{1}{\sqrt{g}}\partial_x(\frac{\sqrt{g}}{h_x}q_{e,x}) + \frac{1}{\sqrt{g}}\partial_y(\frac{\sqrt{g}}{h_y}q_{e,y}) +$$

$$+ \frac{nT_e}{\sqrt{g}}\partial_x[\frac{\sqrt{g}b_x}{h_x}(V_\parallel - \frac{j_\parallel}{en})] = \qquad (3.13)$$

$$= Q_e + nT_eB\frac{1}{h_xh_y}[\partial_y\Phi\partial_x(\frac{1}{B^2}) - \partial_x\Phi\partial_y(\frac{1}{B^2})]$$

while the ion energy balance becomes

$$
\frac{3}{2}\partial_t(nT_i) + \frac{1}{\sqrt{g}}\partial_x(\frac{\sqrt{g}}{h_x}q_{i,x}) + \frac{1}{\sqrt{g}}\partial_y(\frac{\sqrt{g}}{h_y}q_{i,y}) + \frac{nT_i}{\sqrt{g}}\partial_x(\frac{\sqrt{g}}{h_x}V_{\parallel}b_x) =
$$

$$
= \frac{3m_e}{m_i}n\nu_{ei}(T_e - T_i) + \frac{\eta_0}{3}(2b_x\frac{1}{h_x}\partial_x V_{\parallel})^2 + \tag{3.14}
$$

$$
+ nT_i B\frac{1}{h_x h_y}[\partial_y\Phi\partial_x(\frac{1}{B^2}) - \partial_x\Phi\partial_y(\frac{1}{B^2})]
$$

where the heat fluxes $q_{e,x}, q_{e,y}, q_{i,x}$ and $q_{i,y}$ account for contributions from drifts, currents and anomalous heat transport. Their expressions are reported in [18, 57, 58]. Notice that in SOLPS the ion temperature is unique and shared by all ions species and neutrals species.

It is worth noticing here that when SOLPS is applied to a linear plasma device configuration the plasma drifts included in the evaluation of the perpendicular plasma velocity (see equations 3.4 and 3.5) are turned off [37]. Equations for plasma quantities are therefore coherently simplified. Technically, this is related to the fact that they would be either in the direction of rotational symmetry for the system, not simulated by SOLPS, or either null as the polar component $b_z = 0$ in this configuration (see equations 3.4 and 3.5). From the physical point of view, the drifts would usually develop only in the direction of rotational symmetry for the system, that is the polar direction, which is not simulated by SOLPS. This can be seen, for example, also in the self-consistent drifts profiles evaluation from GBS, shown in section 5.2.2 for this kind of configuration. In particular, their effects in the axial and radial direction would be null. Indeed, in SOLPS the evaluation of drift velocities is meant to simulate only their effects in the 2D plane resolved in simulations and not directly compute their profiles.

3.1.3 *EIRENE Package for Neutral Species*

SOLPS, when operated in coupled mode (see the introduction of section 3.1), applies a kinetic treatment for neutral species employing the EIRENE package to solve the Boltzmann transport equation (2.4) by Monte Carlo methods. The EIRENE package is entirely written in FORTRAN 90 and, even though the Monte Carlo method employed is meant to solve the transport equation in a 3D volume, the dimension of rotational symmetry is neglected and the volume of each cell of the mesh is computed by taking a fixed length ds in that direction.

The advantages of employing a Monte Carlo method are in its ability to handle complicated geometries and make a detailed description of the system at the kinetic level. On the other side, the statistical noise introduced by the method requires a large number of repeated Monte Carlo histories, and therefore a large computational time, to be smoothed out and in most of the cases it can't be completely removed. This approach can be nevertheless applied in SOLPS as it employs a mean-field approach (see section 2.3.1).

Consider a neutral species a, to which we'll refer as *test particles*, and a fixed *background* of another generic species b whose distribution function is known (take

just one background species for simplicity). Equation 2.4 is rewritten [95] as

$$\partial_t f_a(\mathbf{x}, \mathbf{v}, t) + \mathbf{v} \cdot \nabla_{\mathbf{x}} f_a(\mathbf{x}, \mathbf{v}, t) = -\Sigma_t^a(\mathbf{x}, \mathbf{v})|\mathbf{v}|f_a(\mathbf{x}, \mathbf{v}, t) +$$
$$+ \int C(\mathbf{x}, (\mathbf{v}'; \mathbf{v}))|\mathbf{v}' - \mathbf{V}'|f_a(\mathbf{v}')d\mathbf{v}' + Q(\mathbf{x}, \mathbf{v}, t) \tag{3.15}$$

where the collision term was split into two parts and a general external source Q, not related to species a collisions[2], was added. The first term at RHS represents losses in phase space for the test species due to the collisions of particles of species a with background species b: the loss mechanisms are multiple and they're embodied in the *total macroscopic cross section* $\Sigma_t^a = 1/\lambda_t^a = \nu_t^a/|\mathbf{v}|$, where λ_t^a and ν_t^a are respectively the test particles' *mean free path* and *collision frequency*. The collision frequency is evaluated as

$$\nu_t^a = \sum_k \nu_k^a, \quad \nu_k^a = \sum_{a'} \int \sigma_k(\mathbf{v}, \mathbf{V}, a; \mathbf{v}', \mathbf{V}', a')|\mathbf{v} - \mathbf{V}|f_b(\mathbf{x}, \mathbf{V}, t)d\mathbf{V}d\mathbf{v}'d\mathbf{V}' \tag{3.16}$$

with k corresponding to any different collision that the test species can undergo[3]. The integral at the RHS represents instead a source of particles in phase space for the test species due to collisions of particles of species a with background species b: again gain mechanisms are multiple and they're written in terms of the *collision kernel*

$$C(\mathbf{x}, (\mathbf{v}'; \mathbf{v})) = \sum_k \nu_k^a(\mathbf{x}, \mathbf{v}')c_k(\mathbf{x}, (\mathbf{v}'; \mathbf{v})) \tag{3.17}$$

where $c_k(\mathbf{x}, (\mathbf{v}'; \mathbf{v}))$ is the conditional probability distribution specific for the k process for the post-collision species a to have velocity in the interval $[\mathbf{v}, \mathbf{v} + d\mathbf{v}]$.

The simplest Monte Carlo approach for solving equation 3.15 derives from the physical interpretation of the terms inside it. A neutral test particle is generated in phase space by a given source process and then it travels along straight lines and undergoes collisions with background particles with frequencies $\nu_k^a(\mathbf{x}, \mathbf{v})$ or interacts with domain walls. In each interaction the particle can either vary its velocity or its type. In the Monte Carlo approach this single particle history is followed until the particle is absorbed by computing the particle trajectory between collisions and reproducing collisions' stochastic nature by means of machine generated pseudo-random samples in a process called *analog sampling*. By following a large number of particle histories for a given species the Monte Carlo approach is able to approximate the solution of equation 3.15 in the domain.

An important aspect of the EIRENE code is that it is able also to implement the physics of plasma wall interaction in the system. In particular, one can specify recycling sources on the boundary corresponding to solid targets on the B2.5 mesh, where ion fluxes are available.

The problem-specific part of the Monte Carlo approach design in EIRENE, linked to the definition of the sources Q and collision related terms for each species,

---

[2]But it could be related to other species' collisions generating particles of species a as a result.

[3]In equation 3.16 and in the following we'll adopt the following notation for cross sections or similar collision-related quantities: when writing $\sigma(\mathbf{u}, \mathbf{U}, p; \mathbf{w}, \mathbf{W}, q)$, the first three arguments represent respectively the test and background particles velocities and the type of the test particle *before* the collision, while the other three arguments refer to the result *after* the collision.

is described in detail in [95]. One important feature which must be underlined is that EIRENE also takes into account the transport of molecular ions, whose dynamics is not compatible with B2.5 routines, by employing the so-called *static approximation*: their trajectories between collisions are not followed and the test particles are destroyed immediately at its point of birth by a collision. This approximation allow to effectively take into account molecular ions transport, whose complete kinetic dynamics would have been computationally unfeasible to solve (see the introduction to section 2.2). The underlying requirement for the physical soundness of this approach is that the test ions mean free path is much smaller than the numerical space resolution in the computational grid. Practically, this requirement is satisfied only for large-enough values of background plasma density, usually obtained in the SOL of tokamaks.

3.2   GBS code

GBS is a code developed by the working group of the Swiss Plasma Center at École Polytechnique Fédérale de Lausanne (EPFL). It is currently one of the most advanced state-of-the-art level first-principle approach codes available.

The philosophy behind the development of GBS, carried out for over more than ten years now, is to approach a very complex problem, such as SOL turbulent dynamics, in steps of increasing complexity [24]. The first simulation of a limited tokamak configuration became available in 2010 [45], employing a drift-reduced Braginskii model (see section 3.2.2) assuming cold ions together with other simplifications such as the Boussinesq approximation in the treatment of the poloidal drift. Since then, the code has been subject to several improvements over time among which we underline the inclusion of hot-ion effects, the development of a complete set of boundary conditions for all fluid moments, the relaxation of the Boussinesq approximation in the treatment of the polarization drift, the extension to diverted configurations and the inclusion of neutrals dynamics and electromagnetic effects.

Despite a neutral dynamics module has been added into GBS in 2015 [15], the code can be employed either with or without self-consistently evaluating neutral species evolution. Indeed, most of the works currently available in literature related to GBS aren't including neutral species dynamics. In this thesis work we'll focus only on the plasma species simulation in GBS and we don't deal with the neutrals module. The charged species physics included in GBS is described in detail in section 3.2.2. An overview of the way GBS tackles the neutral species transport problem is still offered in section 3.2.3 in order to analyze potential opportunities for future refinements of this work (see chapter 6).

The whole code is written in FORTRAN 90 and it is built as a collection of several modules related to different peculiar features of the code, specifying either physical or computational parameters for the simulation and managing the input/output routines or the execution of the code. Most of the required inputs to the code can be also loaded through an external file which can be edited by the user through a text editor, overwriting default values in the code. A set of MATLAB scripts and commands has also been developed and is available for post-processing.

3.2.1 *Geometry*

As a first-principle approach code, GBS studies the full 3D dynamics of the simulated system in order to catch the effects of fluctuations also in the direction of possible symmetries (see section 2.3.2). Nevertheless, the code, being originally developed to be applied on tokamaks, still applies different approximations and features related to the assumption of periodicity in the system in the direction parallel to the dominant component of the magnetic field lines (in a tokamak device, the toroidal direction). This fact proved to be the main obstacle in the adaption of the GBS code to a linear plasma device configuration and strategies to overcome this problem are described in section 4.3.

Even if other different coordinate systems have been employed and studied in GBS [89], in this work we've adopted a GBS version employing a cartesian coordinate system. The employed set of orthogonal unit basis vectors is left-handed and defined as follows: $\mathbf{e}_z$ refers to the direction of the dominant component of the magnetic field, *i.e.* the direction in which GBS assumes periodicity, while $\mathbf{e}_x$ and $\mathbf{e}_y$ refer respectively to the horizontal and vertical directions perpendicular to $\mathbf{e}_z$. This is shown in figure 3.5 for a tokamak configuration. For a comparison, the different sets of reference frames employed in the SOLPS and GBS simulations are reported in figure 3.6.
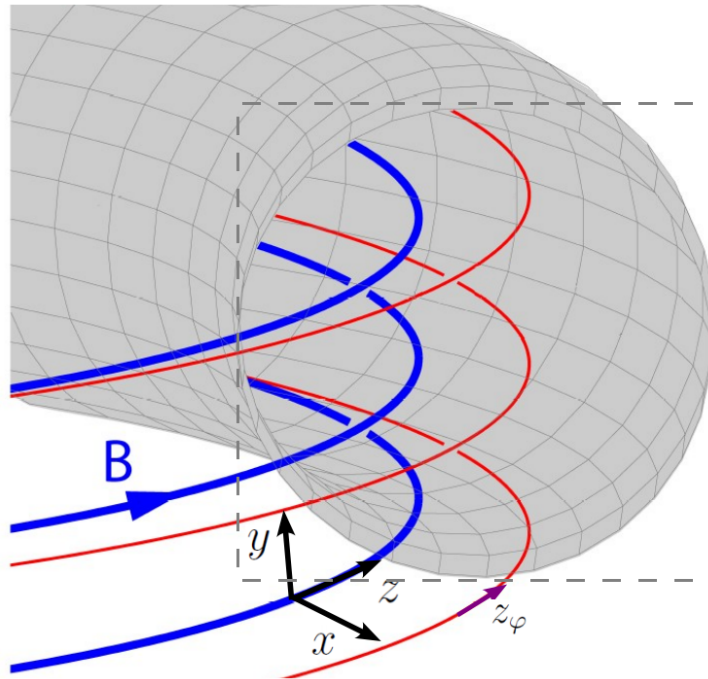
Figure 3.5: Coordinate system for GBS in a tokamak configuration. Taken from [82].

The **B** field dominant component's sign can be specified by the user, as this will influence the direction of the ion-∇B drift. The component of the magnetic field in the $x - y$ plane (in a tokamak device, the poloidal component) is instead loaded by specifying the related magnetic flux function by an analytical definition or importing it from an external file generated in an experimental equilibrium reconstruction or a Grad-Shafranov solver. The cross section of the solid walls of

Type of reference frame	Coordinates		
SOLPS *Dynamical*	**r (equal to y)**	**⊥**	****
	Radial outward, perpendicular to flux surfaces	Perpendicular to the magnetic field, tangent to flux surfaces	Along the magnetic field
Geometrical	**y (equal to r)**	**x**	**z**
	Radial outward, perpendicular to flux surfaces	Along the projection of the magnetic field on the plane perpendicular to the direction of rotational symmetry	Along the direction of rotational symmetry
GBS *Cartesian*	**x**	**y**	**z**
	Perpendicular to the main magnetic field component, perpendicular to *y*	Perpendicular to the main magnetic field component, perpendicular to *x*	Parallel to the main magnetic field component, periodicity assumed in this direction

Figure 3.6: Different sets of reference frames in SOLPS and GBS simulations.

the machine considered are not directly implemented in GBS. Suitable boundary conditions are introduced at the edges of the $x - y$ domain in order to reproduce the contact of the simulated system with the main solid targets subject to plasma flow. In figure 3.7, this is shown in the case of a diverted tokamak configuration. There is no way to simulate a solid wall (and its related effects) directly inside the cartesian domain in GBS at the moment. Even if rotational symmetry in the z direction is not assumed for the whole system, the equilibrium magnetic field loaded in a GBS simulation is required to satisfy this property and an equilibrium magnetic field varying along the z direction can't be currently simulated with the code.

The GBS mesh employed in this work is a 3D structured non-field-aligned cartesian grid. The resolution of the grid can be chosen by the user in each direction. The grid is staggered in y and z directions for different quantities. The implementation of staggering also in the x direction is going to be the subject of next developments in the code. The reason for applying staggering is to avoid checkerboard patterns which can arise in solutions as even and odd grid points in the mesh can decouple in a physical system governed by equations such as the one employed in GBS [89]. Details on its practical implementation will be described more in detail in section 3.2.4. The quantities are divided on staggered grids as follows: on one grid electrons and ions parallel velocities are evolved, on the other grid any other GBS variable (see next section) is evolved, including density. For this reason the two grids are referred to as $v - grid$ and $n - grid$. The n-grid can be obtained by translating forward by half a spatial step the v-grid.

3.2.2   *Drift-Reduced Braginskii Model for Plasma Species*

GBS utilizes a first-principle two-fluid model to solve the plasma species dynamics in its simulations. The plasma species simulated must be atomic ions. The adopted numerical scheme for evolution equations is based on a 4th order Runge-Kutta algorithm for advancing in time and spatial differential operators discretization is based on 4th order accuracy finite differences employing a 5-points stencil, except
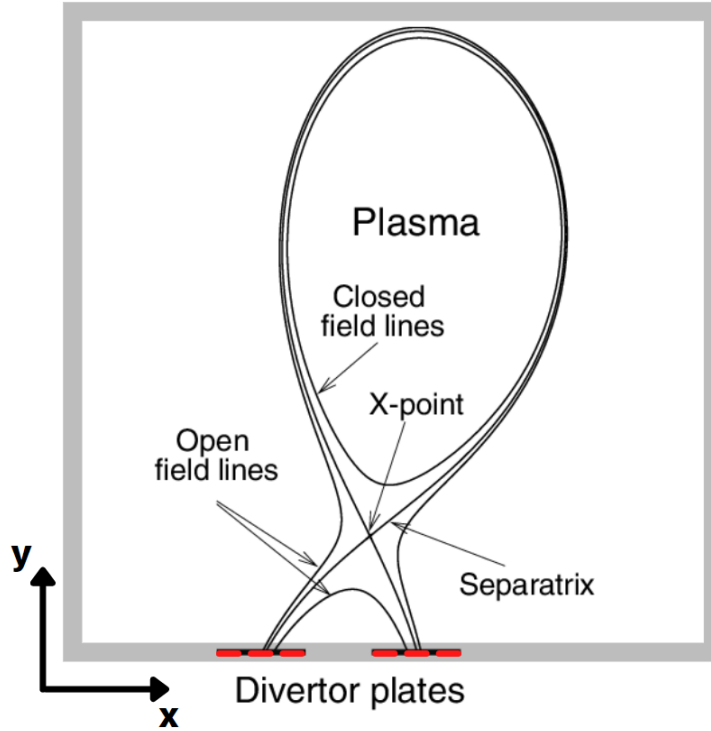
Figure 3.7: Schematic of a diverted tokamak configuration cross section inside the $x - y$ perpendicular grid in GBS. The main plasma targets are located on the bottom edge in red-dotted lines. Suitable boundary conditions are imposed on that edge to represent their presence.

for $\mathbf{E} \times \mathbf{B}$ non-linear advection terms which are discretized employing the Arakawa scheme [64, 90]. Poisson and Ampère equations are instead solved by means of sparse matrix methods or using stencil-based multigrid solvers [24]. The typical work-flow for a GBS simulation not employing the neutrals module is reported in figure 3.8.

The physical model employed is based on Braginskii equations (see section 2.2.1) further simplified by means of the *drift-ordering procedure*. For a complete derivation of the drift-reduced Braginskii model we refer to [11, 102].

The main reason behind this approach is to obtain a model that can be used to numerically investigate plasma turbulence in the SOL. Indeed, the Braginskii model describes the plasma dynamics occurring on a too wide range of time and spatial scales which varies from macroscopical scales to the fast gyromotion, making its use challenging from the numerical side. However turbulence in the SOL is characterized by time variations on scales much slower than ion gyromotion and spatial variations on the scale of the *ion sound Larmor radius* $\rho_s = c_s/\omega_i$, with c_s being the sound speed in the plasma. Therefore one can assume

$$\partial_t \sim \mathbf{V}_{\mathbf{E} \times \mathbf{B}} \cdot \nabla \sim \frac{\rho_s^2}{L_\perp^2} \omega_i \ll \omega_i \qquad (3.18)$$

where $\mathbf{V}_{\mathbf{E} \times \mathbf{B}}$ is the usual $\mathbf{E} \times \mathbf{B}$ drift velocity. In addition, the plasma is also assumed to be quasi-neutral as turbulence takes place on spatial scales much larger

Set IC for $\mathbf{u}^{[1]} = [n^{[1]},\ T_{e,i}^{[1]},\ v_{\parallel e,i}^{[1]},\ \omega^{[1]}],\ \phi^{[1]}$

    for n = 1:Tmax/dt

        $\mathbf{u}^n = [n^{[1]},\ T_{e,i}^{[1]},\ v_{\parallel e,i}^{[1]},\ \omega^{[1]}],\ \phi^n = \phi^{[1]}$

        for i = 1:4

            $\mathbf{k}_i = \text{RHS}(\mathbf{u}^{[i]}, \phi^{[i]})$

            j = mod(i,4)+1

            if j = 1 $\mathbf{u}^{[j]} = \mathbf{u}^n + \text{dt}/6(\mathbf{k}_1 + 2\mathbf{k}_2 + 2\mathbf{k}_3 + \mathbf{k}_4)$

            if j = 2,3 $\mathbf{u}^{[j]} = \mathbf{u}^n + \text{dt}/2\ \mathbf{k}_{j-1}$

            if j = 4 $\mathbf{u}^{[j]} = \mathbf{u}^n + \text{dt}\ \mathbf{k}_{j-1}$

            Apply BC to $\mathbf{u}^{[j]}$

            $\nabla_\perp^2 \phi^{[j]} = \omega^{[j]} - \tau\nabla_\perp^2 T_i^{[j]},\ +$ BC for $\phi^{[j]}$

    end

  end

Figure 3.8: GBS work-flow for simulations not employing the neutrals module. Taken from [89].

than the Debye scale.

The basic idea behind the drift-reduced approximation is to split charged species dynamics into the parallel and the perpendicular direction with respect to the magnetic field and express ions and electrons perpendicular velocities as

$$\mathbf{V}_{\perp,e} = \mathbf{V}_{\mathbf{E}\times\mathbf{B}} + \mathbf{V}_{*,e}$$
$$\mathbf{V}_{\perp,i} = \mathbf{V}_{\mathbf{E}\times\mathbf{B}} + \mathbf{V}_{*,i} + \mathbf{V}_{pol} \tag{3.19}$$

where $\mathbf{V}_{*,a} = -(c/enB)\mathbf{b} \times \nabla p_a$ is the diamagnetic drift, providing together with the $\mathbf{E} \times \mathbf{B}$ drift the 0th order approximation of the perpendicular velocity, and $\mathbf{V}_{pol}$ is the 1st order correction to the perpendicular ion velocity, also called polarisation drift, which can be evaluated as

$$\mathbf{V}_{pol} = \frac{\mathbf{b}}{\omega_i} \times D_t\mathbf{V}_{\perp,i,0} + \frac{1}{nm_i\omega_i}\{\mathbf{b} \times [p_i(\nabla \times \frac{\mathbf{b}}{\omega_i}) \cdot \nabla\mathbf{V}_{\perp,i,0}] +$$
$$+ \mathbf{b} \times \nabla_\perp[\frac{2p_i}{\omega_i}\nabla \cdot \mathbf{b} \times \mathbf{V}_{\perp,i,0}] - \nabla_\perp[\frac{p_i}{2\omega_i}\nabla_\perp \cdot \mathbf{V}_{\perp,i,0}]\} + \tag{3.20}$$
$$+ \frac{1}{nm_i\omega_i}\mathbf{b} \times [G\mathbf{k} - \frac{\nabla G}{3}]$$

where $D_t = \partial_t + (\mathbf{V}_{\mathbf{E}\times\mathbf{B}} + \mathbf{V}_{\parallel,i}) \cdot \nabla$, $\mathbf{k} = \mathbf{b} \cdot \nabla\mathbf{b}$ is the field curvature and $G = -\eta_0(2\nabla_\parallel\mathbf{V}_\parallel - \mathbf{k} \cdot \mathbf{V} - 1/3\nabla \cdot \mathbf{V})$ is the stress function. The polarisation drift is neglected for electrons since its contribution in transport equations would be smaller than the ions one by a factor $\sqrt{m_e/m_i}$.

A further simplification is done excluding compressional Alfvén waves from the dynamics of the simulated system, since they're much faster than turbulent fluctuations [85]. This is done by choosing the vector potential **A** to be purely parallel to the magnetic field. Employing also a low-β assumption, that is $\beta = 8\pi(p_e + p_i)/B^2 \ll 1$, it is then possible to rewrite the perturbed magnetic field as

$$\delta B \simeq \mathbf{b} \times \nabla_\perp \varphi \tag{3.21}$$

and therefore the parallel derivative operator as

$$\nabla_\parallel = \mathbf{b} \cdot \nabla + \frac{\mathbf{b}}{B} \times \nabla_\perp \varphi \cdot \nabla \tag{3.22}$$

The following terms are rewritten as

$$\nabla \cdot (n\mathbf{V}_{*,e}) = -\frac{2c}{eB}C(p_e)$$
$$\nabla \cdot (n\mathbf{V}_{\mathbf{E}\times\mathbf{B}}) = \frac{c}{B}[\Phi, n] + \frac{2cn}{B}C(\Phi) \tag{3.23}$$

where $C(f)$ is the curvature operator defined as

$$C(f) = \frac{B}{2}(\nabla \times \frac{b}{B}) \cdot \nabla f \tag{3.24}$$

and $[\Phi, f]$ is the Poisson Bracket operator defined as

$$[\Phi, f] = \mathbf{b} \cdot (\nabla\Phi \times \nabla f) \tag{3.25}$$

and this also allows to rewrite for both electrons and ions

$$G_a = -3\eta_{0,a}[\frac{2}{3}\nabla_\parallel V_{\parallel,a} + \frac{1}{3}C(\Phi) - \frac{c}{enB}C(p_a)] \tag{3.26}$$

At this point it is possible to rewrite the transport equations in the form employed in GBS after some further manipulation and neglecting the least important terms:

- the continuity equation

$$\partial_t n = -\frac{c}{B}[\Phi, n] + \frac{2c}{eB}[nC(T_e) + T_eC(n) - enC(\Phi)] -$$
$$- n\nabla_\parallel V_{\parallel,e} - V_{\parallel,e}\nabla_\parallel n + D_n(n) + S_n \tag{3.27}$$

- the ion and electron momentum balance equations

$$m_e n\partial_t V_{\parallel,e} + \frac{en}{c}\partial_t\varphi = -m_e n\frac{c}{B}[\Phi, V_{\parallel,e}] - m_e nV_{\parallel,e}\nabla_\parallel V_{\parallel,e} - \frac{2}{3}\nabla_\parallel G_e -$$
$$- \frac{e^2 n^2}{\sigma_\parallel}(V_{\parallel,e} - V_{\parallel,i}) + en\nabla_\parallel \Phi - T_e\nabla_\parallel n -$$
$$- 1.71n\nabla_\parallel T_e + D_{V_{\parallel,e}}(V_{\parallel,e}) + S_{V_{\parallel,e}} \tag{3.28}$$
$$m_i n\partial_t V_{\parallel,i} = -m_i n\frac{c}{B}[\Phi, V_{\parallel,i}] - m_i nV_{\parallel,i}\nabla_\parallel V_{\parallel,i} - \frac{2}{3}\nabla_\parallel G_i -$$
$$- n\nabla_\parallel T_e - T_e\nabla_\parallel n - T_i\nabla_\parallel n + D_{V_{\parallel,e}}(V_{\parallel,i}) + S_{V_{\parallel,i}}$$

- the ion and electron energy balance equations

$$\partial_t T_e = -\frac{c}{B}[\Phi, T_e] - V_{\|,e}\nabla_\| T_e + \frac{4}{3}\frac{c}{eB}[\frac{7}{2}T_e C(T_e) + \frac{T_e^2}{n}C(n) - eT_e C(\Phi)]+$$

$$+\frac{2}{3e}\{T_e[0.71\nabla_\| V_{\|,i} - 1.71\nabla_\| V_{\|,e}] + 0.71 T_e(V_{\|,i} - V_{\|,e})\frac{1}{n}\nabla_\| n\}+$$

$$+D_{T_e}(T_e) + \nabla_\|(\chi_{\|,e}\nabla_\| T_e) + S_{T_e}$$

$$\partial_t T_i = -\frac{c}{B}[\Phi, T_i] + \frac{4}{3}\frac{cT_i}{eB}[C(T_e) + \frac{T_e}{n}C(n) - eC(\Phi)]+$$

$$+\frac{2}{3}\{T_i(V_{\|,i} - V_{\|,e})\frac{1}{n}\nabla_\| n - \frac{2}{3}T_i\nabla_\| V_{\|,e}\} - V_{\|,i}\nabla_\| T_i-$$

$$-\frac{10}{3}\frac{cT_i}{eB}C(T_i) + D_{T_i}(T_i) + S_{T_e}$$

(3.29)

- the vorticity equation (in this work we'll employ its version assuming the Boussinesq approximation [85])

$$\partial_t\omega + \tau\partial_t\nabla_\perp^2 T_i = -\frac{c}{B}[\Phi, \omega] - \frac{c}{B}[\varphi, \nabla_\perp^2 T_i] - V_{\|,i}\nabla_\|\omega - V_{\|,i}\nabla_\|\nabla_\perp^2 T_i+$$

$$+\frac{m_i\omega_i^2}{e}[\nabla_\|(V_{\|,i} - V_{\|,e}) + (V_{\|,i} - V_{\|,e})\frac{\nabla_\| n}{n}]+$$

$$+\frac{2B}{cm_i}[C(T_i) + \frac{T_i}{n}C(n) + C(T_e) + \frac{T_e}{n}C(n)]+$$

$$+\frac{B}{3cm_i n}C(G_i) + D_\omega(\omega) + S_\omega$$

(3.30)

where $\tau = T_i/T_e$ and $\omega = \nabla_\perp^2 \Phi + (\tau/e)\nabla_\perp^2 T_i$ is the vorticity, which is related to the plasma fluid rotation in the plane perpendicular to the magnetic field.

In each of these equations an artificial perpendicular diffusion term $D_f(f) = D_f\nabla_\perp^2 f$ is included for numerical stability reasons and a generic source S_f appears, which can be defined by the user or, when the neutrals module is employed, it can account for neutral sources in transport equations.

The actual form of the above equations implemented in GBS is adimensionalized. More precisely, the following quantities are adimensionalized to the following reference values: n to the reference density n_0, T_e to the reference density T_{e0}, T_i to the reference density T_{i0}, Φ to T_{e0}/e, $V_{\|,e}$ and $V_{\|,i}$ to $c_{s0} = \sqrt{T_{e0}/m_i}$, ψ to $\beta c m_i c_{s0}/2e$ and time t to $L_\|/c_{s0}$. Lengths in the parallel direction are adimensionalized to $L_\|$ while lengths in the perpendicular direction to $\rho_{s0} = c_{s0}/\omega_i$.

The full set of equations is then completed by Poisson and Ampère equations which, in their adimensionalized form, read respectively

$$\nabla_\perp^2\tilde{\Phi} = \tilde{\omega} - \tau\nabla_\perp^2(\tilde{T}_i)$$

$$(\nabla_\perp^2 - \frac{\beta_{e,0}}{2}\frac{m_i}{m_e}\tilde{n})\tilde{V}_{\|,e} = \nabla_\perp^2(\tilde{V}_{\|,e} + \frac{m_i}{m_e}\tilde{\psi}) - \frac{\beta_{e,0}}{2}\frac{m_i}{m_e}\tilde{n}\tilde{V}_{\|,i} + \frac{\beta_{e,0}}{2}\frac{m_i}{m_e}\tilde{j}_\|$$

(3.31)

where we have identified with $\tilde{f}$ adimensionalized quantities, which can be obtained as described just above. $j_\|$ is the plasma current and $\beta_{e,0}$ is the ratio of the reference electrons pressure to reference magnetic pressure in the system. The Boussinesq approximation is employed here in the Poisson equation.

3.2.3 *Method of Characteristics for Neutral Species*

Even if not directly employed in this thesis work, in this section a brief description of the neutrals module in GBS is reported. We refer to [15] for a more detailed derivation and explanation. This approach treats neutrals dynamics at the kinetic level.

The evolution equation for f_n is rewritten as

$$\partial_t f_n + \mathbf{v} \cdot \partial_{\mathbf{x}} f_n = -\nu_{iz} f_n - \nu_{cx}(f_n - \frac{n_n}{n_i} f_i) + \nu_{rec} f_i \qquad (3.32)$$

where $n_{i,n}$ are the ions and neutrals densities respectively and where the ionization, charge-exchange and recombination frequencies are computed as

$$\nu_{iz} = n_e \langle v_e \sigma_{iz} \rangle \quad \nu_{rec} = n_e \langle v_e \sigma_{rec} \rangle \quad \nu_{cx} = n_i \langle v_i \sigma_{cx} \rangle \qquad (3.33)$$

with effective cross-sections taken from the OpenADAS database [1].

The following boundary condition is imposed at solid targets: saturation is assumed so that any impacting particles, either charged or neutral, is re-emitted instantly inside the domain. Some particles are reflected and some are absorbed and released with a velocity depending on the wall structure and its temperature, that is

$$\begin{aligned} f_n(\mathbf{x}_w, \mathbf{v}) =& (1 - \alpha_{refl})\Gamma_{out}(\mathbf{x}_w)\chi_{in}(\mathbf{x}_w, \mathbf{v}) \\ &+ \alpha_{refl}[f_n(\mathbf{x}_w, \mathbf{v} - 2\mathbf{v}_p) + f_i(\mathbf{x}_w, \mathbf{v} - 2\mathbf{v}_p)] \end{aligned} \qquad (3.34)$$

with α_{refl} depending on the wall material, Γ_{out} being the ions and neutrals outflowing flux and $\mathbf{v}_p$ the perpendicular velocity with respect to the wall. The inflowing velocity distribution χ_{in} is set according to the Knudsen cosine law [83].

Equation 3.32 is solved by using the method of characteristics under the assumption that plasma-related quantities are known. The formal solution reads

$$f_n(\mathbf{x}, \mathbf{v}, t) = \int_0^{r'_w} \left[\frac{S(\mathbf{x}', \mathbf{v}, t)}{v} + \delta(r' - r'_w)f_n(\mathbf{x}'_w, \mathbf{v}, t'_w) \right] e^{-\int_0^{r'} \nu_{eff}(\mathbf{x}'', t'')dr''/v} dr' \quad (3.35)$$

with $\mathbf{x}' = \mathbf{x} - r'\mathbf{\Omega}$, $t' = t - r'/v$, $\mathbf{\Omega} = \mathbf{v}/v$ (and similar definitions for $\mathbf{x}''$ and $\mathbf{t}''$) and the volumetric source S is evaluated as

$$S(\mathbf{x}', \mathbf{v}, t) = \nu_{cx}(\mathbf{x}', t')n_n(\mathbf{x}', t')\Phi_i(\mathbf{x}', \mathbf{v}, t) + \nu_{rec}(\mathbf{x}', t')f_i(\mathbf{x}', \mathbf{v}, t) \qquad (3.36)$$

with Φ_i being a Maxwellian distribution for the ions.

As S depends on $n_n(\mathbf{x}', t') = \int f_n(\mathbf{x}', \mathbf{v}, t')d\mathbf{v}$, equation 3.35 is an integral equation for f_n in both space and velocity domain. Some approximations are then introduced to simplify the problem: a neutral adiabatic regime is assumed, meaning that it holds $\partial_t f_n \simeq 0$ and therefore $t \simeq t'$, and the neutrals λ_{mfp} is assumed to be negligible with respect to the characteristic dimension of the system in the direction parallel to the magnetic field, meaning that it holds $\mathbf{x}' = (\mathbf{x}'_\perp, x'_\parallel) \simeq (\mathbf{x}'_\perp, x_\parallel)$. With these assumptions, the dependencies on $x_\parallel$ and t for equation 3.35 are now just parametric and the equation can be solved directly just on the plane perpendicular to the main magnetic field component.

Some analytical manipulations are carried out then to obtain the final form for equation 3.35 as a linear integral equation for n_n and Γ_{out}, the perpendicular component of neutrals and ions outward flux at boundaries, which is then implemented in GBS. The spatial discretization of the problem allows then to recast this last equation in the form of a linear algebraic problem which can be solved with standard full matrix solvers. Since its solution is particularly expensive from the computational side, a short cycling scheme is applied where neutrals density and related quantities are recalculated every Δt_n interval, with this time step being much larger than the typical time step used to advance numerically the plasma transport equations.

3.2.4   *Technical Details on Spatial Discretization*

It is useful to introduce in this section some additional details related to technical aspects of the GBS code, in particular with respect to spatial discretization. This is helpful for the comprehension of the modifications implemented in GBS in this thesis work with the goal of applying the code to a linear plasma device. Those will be discussed in detail in section 4.3.

The first important feature we'll discuss here is parallelization. The GBS code exploits parallelization to speed up its computation by both running the plasma and the neutrals module in parallel and parallelizing operations in each module. In the framework of this thesis work, having focused our attention only on the plasma module, we've dealt only with the parallelization method applied to it. Since finite differences are employed to discretize spatial derivatives operators in transport equations, an effective parallelization by means of *MPI domain decomposition* can be applied in each direction. These communications are carried out by means of *ghost cells* and standard MPI functions. Given a domain of $n_x \times n_y \times n_z$ points, the number of decomposed domains in each direction N_x, N_y and N_z is chosen by the user and this implies that in any given direction k the domain is divided in N_k intervals. As a 5-points stencil is employed to compute spatial differential operators, 2 ghost cells are applied on each side of a decomposed domain region, meaning that each of these sub-domain regions is composed by $(n_x/N_x + 4) \times (n_y/N_y + 4) \times (n_z/N_z + 4)$ points. The actual communication between adjacent domain regions is performed copying the last two "real"[4] cells' values in a given direction inside the first two ghost cells in the next adjacent sub-domain in that direction. This is shown in figure 3.9.

This method can't fill the ghost cells at the boundary of the total simulation domain. On the z direction, since periodicity is assumed (see section 3.2.1), an automatic MPI communication is carried out and it copies cells' values between the first and the last sub-domains in the z direction, in the same way it is done with inner adjacent sub-domains. On other edges, where other boundary conditions should be imposed, filling routines are applied in the $x - y$ directions. Some boundary conditions routines are employed to compute the values which are then used to fill the external layer of ghost cells in the $x - y$ direction. Those values

---

[4]Here and in the following, with "real" we refer to a point of the domain which is not a ghost cell and whose value is therefore not determined by copying adjacent sub-domains values but by evolving the plasma transport equations.
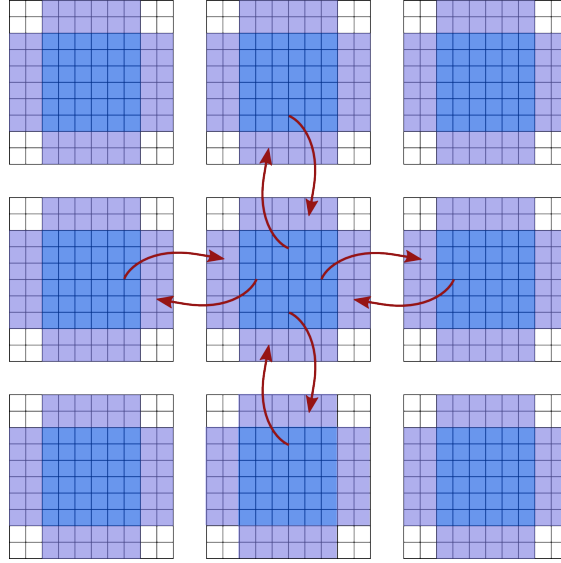
Figure 3.9: Schematic example of domain decomposition. This is the kind of paralleliza-
tion approach applied for plasma transport equations in GBS.

depend on the kind of boundary condition to be imposed over a given edge and it
can depend on internal points values. As an example, consider the left side in the
x direction: labelling the first "real" point inside the simulated domain with the
index 0, and therefore adjacent ghost cells with indexes -1 and -2, and calling
f_{BC} the actual boundary condition value, one can have in general:

- for *Dirichlet* boundary conditions either

$$\begin{cases} f_{-1} = f_{BC} \\ f_{-2} = f_{BC} \end{cases} \quad or \quad \begin{cases} f_{-1} = 2f_{BC} - f_0 \\ f_{-2} = 2f_{BC} - f_1 \end{cases} \tag{3.37}$$

the latter option making the boundary condition applied at the midpoint
between the last "real" point in the domain and the first ghost cell.

- for *Neumann* boundary conditions usually just

$$\begin{cases} f_{-1} = f_0 - f_{BC}\Delta x \\ f_{-2} = f_{-1} - f_{BC}\Delta x \end{cases} \tag{3.38}$$

In directions where staggering is applied (see section 3.2.1), asymmetries arise
in the exploitation of the numerical grid if physical boundaries are imposed on
cells belonging to the same grid. These asymmetries must be taken into account
when imposing boundary conditions. As an example, see figure 3.10: in this
simplified example only 1 direction and 4 "real" points were assumed and no
domain decomposition was performed to simplify the picture. Physical boundaries
are imposed to be on the first and the last point of the n-grid. This implies on
the left side of the domain 3 points for the v-grid are out of the simulated domain
while on the right side they're just 2. On these points boundary conditions must
be imposed. The values of the two points on the right and on the first two points

on the left outside the simulated domain on the v-grid are imposed according to the scheme for boundary conditions described above. The value for the third point on the left outside the simulated domain on the v-grid is instead not important as this point is never used by any 5-points stencil for "real" points inside the domain. It is also important to notice that the first point on the left outside the simulated domain on the v-grid is not a ghost cell and its value is going to be updated at each step according to plasma transport equations before getting overwritten by boundary conditions.
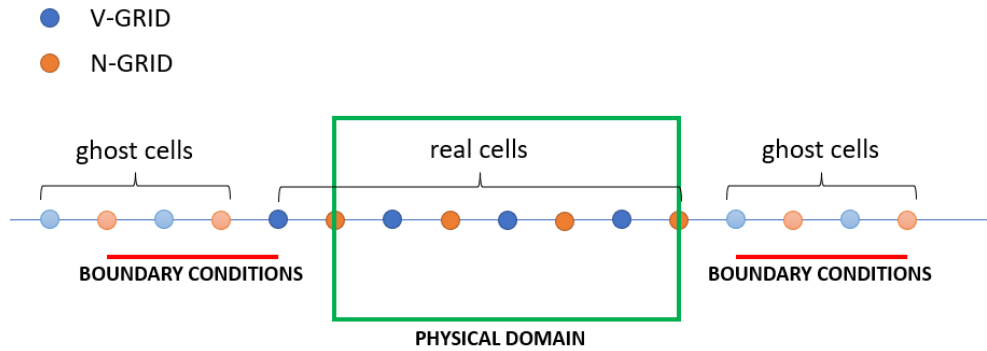

Figure 3.10: Schematic example to show asymmetries in GBS numerical grid exploitation when staggering is applied.

Modeling of the
LPD Configuration

In this chapter, the numerical modeling of the chosen linear plasma device configuration, based on the GyM machine (see section 2.4), for the simulations is presented.

First, the simulation setup chosen for this thesis work will be introduced (§ 4.1), describing and motivating the geometrical structure and the parameters of the setup and the choice for the employed neutral and plasma species.

Then peculiar aspects and choices related to the linear plasma device configuration modeling in the two employed codes will be addressed. We'll start by describing how the SOLPS code can be applied for this kind of configuration, as already done in previous examples from literature [23, 37]. It'll be presented the problem of the mesh construction (§ 4.2.1) and of the electron cyclotron resonance heating (ECRH) source modelling (§ 4.2.2). Peculiar attention will be drawn also to the aspect of boundary and initial conditions definition (§ 4.2.3).

About the GBS code we'll start by detailing and motivating the approximations and the boundary conditions employed (§ 4.3.1). We'll then go on showing the needed modifications which had to be carried out to the structure of the code in this thesis work in order to apply for the first time this GBS version to a linear plasma device configuration (§ 4.3.2; § 4.3.3). Finally, a presentation of the sources and initial profiles definitions (§ 4.3.4) used in the simulations will be given.

4.1   SIMULATION SETUP

The GyM linear plasma device main characteristics were described in section 2.4.

The simulation setup chosen for this thesis work is shown in figure 4.1, together with a 2D map in the radial and axial direction of the magnetic field intensity. A metallic sample holder is placed on the cylindrical GyM chamber axis at a distance of $L_\parallel = 1.18\ m$ from the left metallic target at the bases of the cylindrical camera in the figure. The sample target is placed with its plane face parallel to the metallic targets at the bases of the cylindrical camera and the cross section of this face can be well approximated by a circle of radius $r = 0.05\ m$.

With respect to other important parameters for the simulation, we'll start setting a current $I = 600\ A$ in coils in order to generate the equilibrium magnetic
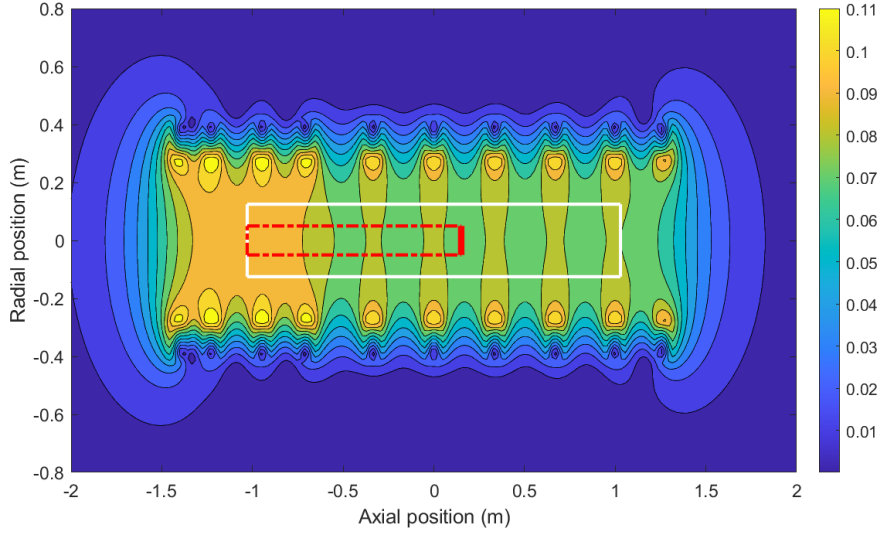
Figure 4.1: Geometrical setup for the simulations carried out in this thesis work. A 2D map of the magnetic field intensity is also shown. White solid lines represent the contour of the walls of the GyM vacuum chamber. Solid red line represents the metallic sample holder. Dashed-dotted red lines, together with the solid red line, represent approximately the region in which the simulated plasma column is formed.

field. The gas puffing system is set to inject a flux $G = 20 \ sccm/s$ of neutral He in the system. This neutrals flux is heated up and transformed into a plasma by the radio frequency source, set to deliver an effective power $P = 1 \ kW$ to the system by electron cyclotron resonance. More details on this heating system will be provided in section 4.1.2.

From the geometrical point of view, the configuration presented above is able to describe, as a first approximation, a peculiar experimental scenario actually employed in GyM machine. This is the case of experimental campaigns devoted to plasma-material interaction studies. It corresponds to the situation in which a metallic sample is put inside GyM vacuum chamber to be exposed to certain fusion-relevant plasma conditions.

The motivations which have driven the choice of this particular simulation setup are the following:

- the values of injected neutral flux G and effective power P introduced in the system are chosen so that the simulated plasma quantities approach the realistic values obtained in previous SOLPS studies on the GyM machine [23, 37]. In this way the choice of free parameters in the SOLPS simulations and the evaluation of the importance of different effects in the system will be more straightforward, basing our choice on previous results in literature. At the same time, these values are chosen because they're thought to be consistent with GBS physical model basis assumptions by *a priori* estimates.

- the choice of He as the neutral and plasma species is justified by three reasons. The first one is that He is currently a material of strategic importance in
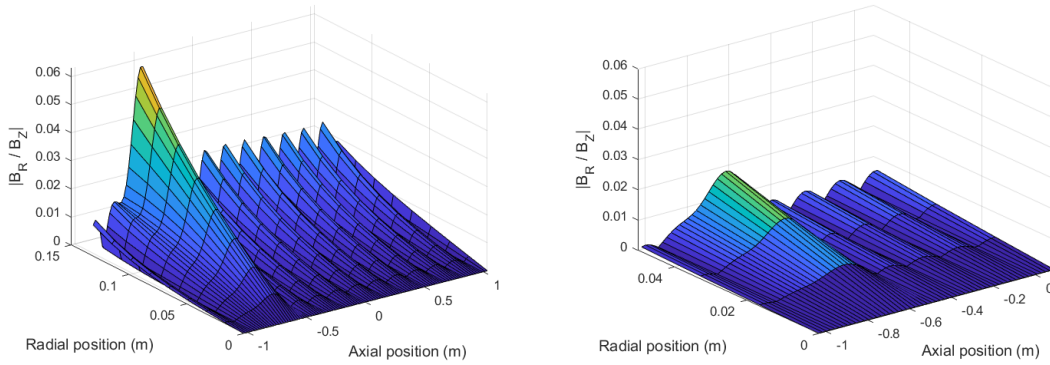
(a) In the whole GyM vacuum chamber.

(b) In the reduced plasma column region (see figure 4.1).

Figure 4.2: Radial to axial magnetic field component intensity ratio.

nuclear fusion research, both as a plasma component and as a neutral species [38, 39, 60]. The second reason is that He, being an inert gas, can't form molecules, thus simplifying in an important way the neutrals dynamics to be simulated and avoiding the presence of molecular ions in the system. The third reason is that the analysis of an He plasma was already carried out in the GyM machine [23]. The simplified neutral dynamics and the previous results in literature allow to identify in an easier way neutrals-related mechanisms, which is a fundamental aspect for building GBS sources, as it'll be explained in section 4.3.4. In addition, the presence of only atomic ions is coherent with the requirement of the GBS code (see section 3.2.2) and it avoids simulating the transport of molecular ions with EIRENE in SOLPS, which would imply relying on assumptions which are hardly met on a low density plasma device such as the GyM machine (see section 3.1.3).

- as it'll be explained in section 4.3.1, in the GBS simulation a constant magnetic field directed along the axis of the cylindrical chamber will be assumed. By restricting the approximate region in which the simulated plasma column is formed to the area delimited by the red lines in figure 4.1, the simulated plasma region is moved further from the coils producing the magnetic field, thus reducing the relative importance of the radial component with respect to the axial component of the magnetic field in the region of interest and making the GBS approximation more sounded. This is shown in figure 4.2.

- as it'll be explained in section 4.3.1, in the GBS simulation no solid walls in the radial directions will be assumed. By restricting the approximate region in which the simulated plasma column is formed to the area delimited by the red lines in figure 4.1, the simulated plasma region is moved far enough from the lateral solid surfaces in radial direction of the GyM vacuum chamber, thus implying their effects on the evolution of the simulated plasma dynamics can be effectively considered negligible.

4.2   SOLPS Simulations

As it was already outlined in section 3.1.1, the SOLPS code is originally developed to be applied to tokamak diverted geometries.

Its application to linear plasma devices configurations is not straightforward and mainly relies on the careful readaption of the equilibrium magnetic field definition and the mesh generating processes for this case. As mentioned in the introduction of this chapter, this work was already carried out in previous studies on the GyM machine [23, 37] and, in this thesis work, we exploit their strategies for our case. Nevertheless in the next section the problem of generating the B2.5 and EIRENE meshes in SOLPS for the simulation setup chosen in this thesis work will be briefly addressed.

In addition, the adopted electron cyclotron resonance heating (ECRH) source physical modeling will be described together with its implementation in SOLPS and the related weaknesses of the model.

Finally, the adopted set of boundary and initial conditions in SOLPS for each side of the B2.5 mesh will be described. The limits related to the imposed set of boundary conditions, in particular with respect to plasma quantities profiles in the radial direction, will be also addressed.

4.2.1   *Mesh Construction*

As already discussed in 3.1.1, a 2D mapping of the value of the magnetic flux function in each point of the axial-radial plane is necessary to construct the computational B2.5 grid and from this, later, the EIRENE grid. The B2.5 mesh will be a rectangular-cell mesh with two parallel sides aligned with magnetic field lines and the remaining two parallel sides aligned with the radial cross-field coordinate. The EIRENE mesh will be instead built by the merging of the triangularization of the B2.5 mesh and the triangularization of the remaining empty volume between it and the walls of the simulated machine.

Since the original SOLPS graphical interface can't be used to construct the B2.5 mesh, as it can treat only toroidal geometries, an *ad-hoc* mesh generator needs to be employed for a linear plasma device configuration. It performs the following steps:

- Grad-Shafranov equation [74] is solved to compute the flux function φ in the configuration, given the coils distribution and the current they carry.

- many $iso - \psi$ lines are computed in the region of interest of the axial-radial plane for the simulation. It must be noted that these lines must cross the metallic sample face (see figure 4.1) on one side and the metallic target at the bases of the cylindrical chamber on the other end. The number of isolines defines the number of cells in the radial direction n_y.

- the domain is divided into n_x cells in the axial direction by cutting isolines orthogonally to the cylinder axis, along the radial direction.
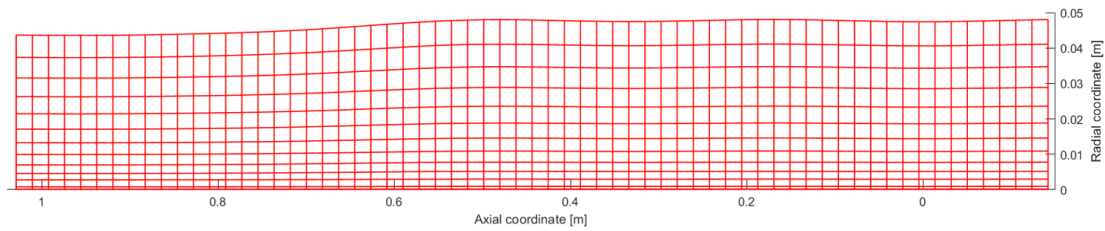
(a) B2.5 mesh (axis in scale 1:4).
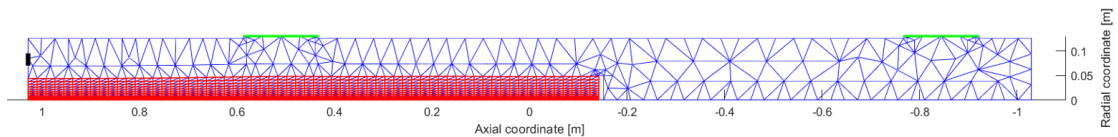
(b) Superposition of the two meshes (axis in scale 1:1).

Figure 4.3: The two different meshes employed in the SOLPS simulation. Edges in which pumping is imposed are shown in green while the puffing system is shown in black. Only half of the radial-axial plane can be considered thanks to rotational symmetry in the polar direction.

- finally, one more cell outside each boundary cell is added: these cells are called guard cells, they are much smaller than other cells and are used to set the boundary conditions.

Once this grid is ready, an ASCII file is prepared containing the axial and radial coordinates of cell vertexes and centers and the values of the axial and polar (which is null in this case) components of the magnetic field at the cell center. This file becomes the input for one of the SOLPS packages managing the B2.5 mesh creation. It is important to underline here that the B2.5 mesh, on which the plasma transport equations are solved, is limited in its radial extension by the requirement that the iso-ψ lines used for its construction must cross the two solid targets placed in the axial direction.

Once this step is performed, and also the coordinates of the walls of the machine are provided, the EIRENE grid can be created in the usual way by SOLPS routines. It is important to notice that in the definition of the walls of the machine also two turbo-molecular pumps and a puffing system are present acting in the domain. The former are defined as surfaces in which a non-zero absorption probability is set. The pumping speed can be then linked to this probability [95]. On the puffing surface a given injected flux is instead set. EIRENE is therefore able to follow completely the neutrals gas dynamics in the vacuum chamber, in addition to its interaction with the plasma.

The two obtained mesh are presented in figure 4.3. Take care that a different notation is employed for the axial coordinate with respect to previous figures in this section but the orientation of the elements is maintained.

4.2.2 ECRH Source Modeling

As it was outlined in section 2.4, a micro-wave source at 2.45 GHz is employed to heat up the plasma by electron cyclotron resonance heating (ECRH) in the GyM machine.

It is well known that resonant phenomena are able to transfer energy from an electromagnetic wave to a plasma [52, 74]. ECRH is one example of these mechanism and it is related to an efficient energy coupling between the electromagnetic wave and the electron population, occurring when the frequency of the electromagnetic wave ν_{em} is equal to the electron Larmor frequency (see section 1.2.1). By ECRH, electrons resonantly absorb energy from the electromagnetic wave, increasing their kinetic energy.

In the GyM case, an electromagnetic wave is injected in the system by the micro-wave source with a frequency $\nu_{em} = 2.45\ GHz$. Since the electron Larmor frequency depends only on the magnetic field intensity, this translates into a condition for ECRH to be effective: electrons are able to couple and gain energy from the electromagnetic wave when $B = B_{res}$. For $\nu_{em} = 2.45\ GHz$, it holds $B_{res} = 0.0875\ T$. As the actual way in which this electromagnetic wave is is absorbed in the system, and in which fraction, is not known, we employ the following simple approximation for the modelling of the ECRH source. Plotting the iso-line related to a magnetic field intensity value equal to B_{res}, one assumes energy is spatially deposited by the ECRH mechanism in these corresponding regions. These iso-lines are shown in figure 4.4 for different values of current in the coils generating the magnetic field in the GyM machine. It can be seen that, for the value of current assumed in this thesis work, $i.e.\ I = 600\ A$, the resonance region is almost a straight line radially crossing the whole chamber at a fixed axial position.
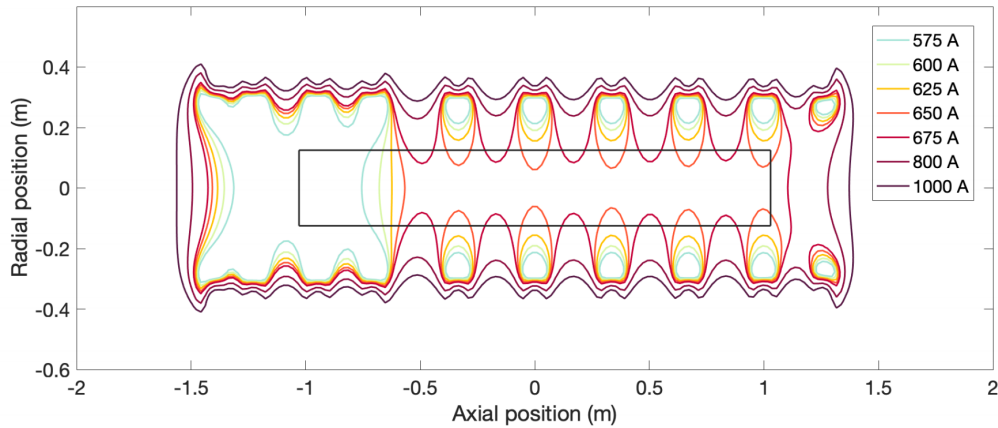
Figure 4.4: Iso-lines for a magnetic field intensity value $B = B_{res} = 0.0875\ T$ in the GyM machine. Solid black lines represent the chamber walls.

In the SOLPS simulation this plasma heating mechanism is introduced as an external source term in the electron energy balance (see equation 3.13). The power density deposited in the system is then modelled with the following profile inside the B2.5 domain: in the axial direction a narrow gaussian centered at the resonant axial coordinate is assumed, while in the radial direction a constant profile is assumed

up to large radii, where a steep tanh profile brings down the value to 0. This profile will be shown in section 5.1.2.

The main weaknesses of this power source modeling are the following: (a) additional resonant mechanisms might be present in the system but their location in the machine would be difficult to predict since it would depend on the local plasma density, which is not known *a priori* [37], (b) direct measurements of the ECRH absorbed power are not available, implying that the actual absorption, propagation and reflection patterns of electromagnetic wave in the system might be more complicated with respect to the modeling used in this thesis work, (c) the employed model for ECRH source implies power density is deposited constantly in the system in the radial direction, but only up to the radial extension of the B2.5 mesh which, as explained in section 4.2.1, is limited by technical requirements to a radius which is approximately that of the metallic sample holder (see figure 4.1).

4.2.3 *Boundary Conditions and Initial Conditions*

The kinds of boundary conditions imposed on the different edges of the B2.5 mesh are the following:

- at solid targets, representing the extremes of the simulation domain in the axial direction, boundary conditions are evaluated at the sheath entrances so that Bohm criterion (see section 2.1.1) can be applied. Parallel plasma velocity is then set to be equal to the local plasma speed of sound. About plasma density and ions and electrons temperatures, flux densities are instead imposed. As the magnetic field is perpendicular to the solid target, the particles flux is set to $\Gamma_{BC} = n c_s$ in the direction of the target itself. At the same time, heat fluxes are specified as $q_{BC} = \gamma \Gamma_{BC}(T_e + T_i)$, where γ is the sheath transmission factor [99].

- at the cylindrical chamber axis, that is a symmetry axis for the system and the lower extreme in the radial direction, zero particle, momentum and energy fluxes are set.

- at the external radius exponentially decaying profiles for density, temperature and plasma potential, together with zero parallel momentum flux, must be set. Their corresponding decay lengths are indicated with Λ_n, Λ_{T_e}, Λ_{T_i}, Λ_Φ.

A complete reference about boundary conditions in SOLPS is found in [18].

The main limit of this approach is in the definition of the boundary conditions at the external radius. Indeed, this imposition derives from the fact that this edge of the B2.5 mesh corresponds to the edge facing the radial first wall when diverted tokamak configurations are considered, for which SOLPS is originally developed. The exponential decay in radial direction is strictly correlated to the diffusive approximation for transport in the perpendicular direction [42]. The sink action of targets in the SOL implies plasma temperatures, density and potential, sustained by fluxes coming from the core, tend to drop exponentially radially. As the B2.5 mesh doesn't extend up to the radial wall, SOLPS can't take into account consistently the role of the wall itself. Nevertheless, as the distance between the radial wall and the separatrix is usually much larger than decay lengths in the plasma, this approach

is often able to recover pretty well the experimental results. The same strategy is instead problematic when dealing with the GyM machine. While the experimental density drop in the radial direction near lateral walls is pretty well recovered by this approximation, the same doesn't apply for temperatures and potential [37]. As it can be seen in section 5.1.1, the shape of electron temperature profile, and therefore plasma potential as $\Phi \sim \Lambda T_e/e$, tends to be strongly influenced by the applied ECRH source. The fact this source has always been assumed to be constant radially almost up to the outer radius of the B2.5 mesh [37] creates therefore a conflict between this kind of profile and the imposed exponential decay.

In our simulation setup this kind of boundary condition implies therefore that both density, temperatures and plasma potential will be subject to an artificial drop at the outer radii of the B2.5 mesh, whose steepness can be arranged setting the corresponding decay lengths. This would be problematic therefore with respect to a possible comparison with experimental results. Nevertheless, this is not the aim of this thesis work and the chosen configuration for the simulations is meant to provide a suitable simulation setup for working with both SOLPS and GBS without penalizing much any of the two, as explained in section 4.1.

The kinds of initial conditions imposed for the SOLPS simulations are the following: (a) flat initial profiles for electrons and ions temperatures, plasma potential and plasma and neutrals densities, (b) parallel velocity and plasma current are uniform and set to 0 in the whole domain.

4.3   GBS Simulations

In the framework of this thesis work, the main challenge which was faced was the adaption of the GBS code to a linear plasma device configuration. This is the first time the current version of GBS is employed for simulating this kind of machine. Indeed, as it was already outlined in section 3.2, many aspects and features in the code are related to a tokamak geometry. Therefore, many technical modifications on the code were introduced to simulate the configuration of interest and these will be presented in the following in this section. In addition, further approximations employed for the simulations carried out with the GBS code will be presented and motivated in section 4.3.1.

The general work-flow followed for the original modifications introduced in the current GBS version in this thesis work is based on 3 main steps:

0. the initial version of the GBS code assumes a toroidal magnetic field plasma configuration and therefore periodicity in the toroidal direction.

1. the first modification is carried out by introducing a straight and constant equilibrium magnetic field. An infinite and periodic plasma column configuration is now assumed in the code. This step will be the subject of section 4.3.2.

2. the second modification is carried out by removing the periodicity assumption along the axis of the assumed plasma column and introducing boundary conditions which are suitable to simulate the presence of two metallic targets

at both ends of the column. A finite plasma column generated between two metallic targets is now assumed in the code. This step will be the subject of section 4.3.3.

3. finally, a realistic set of sources and initial conditions will be implemented. This step will be the subject of section 4.3.4.

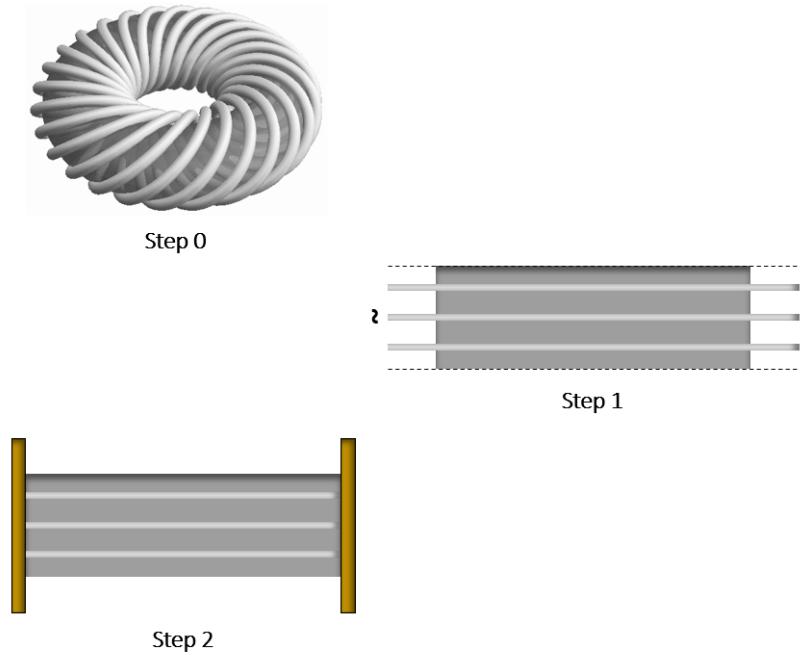The previous steps are reported schematically in figure 4.5.

Figure 4.5: Different configurations obtained in subsequent steps in the GBS code modifications: (0) a toroidal magnetic field plasma configuration, (1) an infinite and periodic plasma column configuration, (2) a finite plasma column between two metallic targets.

4.3.1 *Approximations and Boundary Conditions*

Additional approximations are employed in the GBS modeling of the simulation setup presented in section 4.1. These are mainly justified by technical limitations in the current version of the code. Further work on the code will be needed to overcome these limitations and relax the introduced approximations. In any case, for the goals of this thesis work (see section 2.5), the modified GBS code which was developed is able to catch the features of the simulation setup which were identified as the most important in this kind of configuration: an approximately straight magnetic field lines configuration, the presence of open field lines intersecting metallic targets and the presence of neutrals-related particles and energy sources and sinks.

The additional approximations employed in the GBS modeling of the simulation setup are the following:

- neutrals are not simulated and their effect on the plasma is not included self-consistently. Indeed, the GBS neutrals module was not employed in these

simulations, as no attempt to adapt it to a linear plasma device configuration was carried out within this thesis work. In section 4.3.4 we will explain how fundamental neutrals-related mechanisms for the simulated configuration were taken into account.

- the magnetic field was assumed to be constant and aligned with the axis of the cylindrical chamber, along the z direction in the GBS reference frame (see section 3.2.1). Indeed, as it was explained in section 3.2.1, the equilibrium magnetic field configuration loaded in GBS must be constant along the z direction and, as it was explained in section 4.1, the radial component of the magnetic field in the domain of interest can be considered negligible.

- the radial walls of the cylindrical GyM chamber are not simulated. Indeed, as it was explained in section 3.2.1, the $x - y$ computational grid, oriented in the perpendicular direction with respect to the main magnetic field component and therefore to the cylindrical chamber axis, has a rectangular cross section since the GBS grid is cartesian. This fact, together with the fact that GBS is not able to implement machine walls inside its computational grid (see section 3.2.1), makes the code unable to simulate the lateral circular solid surfaces of the cylindrical chamber. Nevertheless, in the chosen simulation setup (see section 4.1), their influence is reduced as they're not enclosing directly the domain of interest.

- the Boussinesq approximation was employed in the plasma transport equations and the Poisson equation [24]. This choice was applied as the code proved to be more stable in this way from the numerical side. Nevertheless, the GBS code has been run for different studies in previous years employing this approximation [6, 45], still being able anyway to catch the main physical aspects of the physical situation under study.

- ions were supposed to be cold and their temperature evolution was not followed. This choice was not linked to any technical issue with the GBS code but it was just employed for simplifying the physical model. Nevertheless this approximation is sounded in the simulated physical system (see section 4.1) as a low density plasma is expected and therefore thermal equilibration mechanisms are strongly inhibited [23], making the electrons gain an important energy with the ECRH mechanism while hardly sharing it with ions generated from neutrals initially at room temperature.

- the semi-electrostatic approximation is employed, meaning that magnetic fluctuations are neglected and therefore $\psi = 0$. Also this approximation is not related to any technical issue with the GBS code. Nevertheless this is sounded in the chosen simulation setup, characterized by an open field line configuration. Indeed in this case a really low $\beta_{e,0}$ is expected [45] and, in the limit for $\beta_{e,0} \to 0$, the Ampère equation (see equations 3.31) turns into a constraint for ψ to be equal to zero.

Another important aspect related to simulation setup physical modeling in GBS is the choice of boundary conditions to be applied at the metallic targets

position in the axial direction to simulate the presence of solid walls. We've already suggested in section 2.2.2 that in a multi-fluid code based on the Braginskii model and assuming quasi-neutrality, such as GBS, boundary conditions must be defined at the sheath entrance.

The Debye sheath main characteristics were described in section 2.1.1, where two conditions at the sheath entrance, based on Bohm criterion, were identified for ions and electrons parallel velocities for the case of a solid wall perpendicular to magnetic field lines. This is the same case considered in GBS simulations, hence the boundary conditions at targets employed for these two quantities are

$$
\begin{aligned}
V_{\parallel,i}^{BC} &= \pm\, c_s \\
V_{\parallel,e}^{BC} &= \pm\, c_s e^{[\Lambda - e(\Delta\Phi)/T_e]}
\end{aligned}
\tag{4.1}
$$

where the $\pm$ signs are set accordingly in order to have the plasma flow directed towards the solid targets.

For other GBS variables the situation is more complicated. The problem of defining a set of boundary conditions at sheath entrance for plasma quantities in GBS at solid targets has already been tackled for toroidal geometries [6, 82]. In that case, the magnetic field in the configuration intersects obliquely the solid targets. Instead, in the simulation setup for GBS in this thesis work, the magnetic field intersects perpendicularly the solid targets and the same boundary conditions can't be applied. From the physical side, this limit is mainly due to the fact that in the perpendicular case no magnetic sheath develops (see section 2.1.1).

Based on the fact that evolution equations for density, temperatures and vorticity in GBS are advection-like PDE and the advection velocity at targets is approximately sonic, as shown in equations 4.1, from the physical side no boundary conditions should be imposed on those edges for these quantities as no information related to them is able to back-propagate inside the system [75, 81]. Nevertheless, boundary conditions are still required for the numerical scheme used in GBS to work. We decided to use the simplest standard choice usually employed in fluid dynamics as an artificial boundary conditions for sonic outflows [55, 75], that is setting homogeneous Neumann conditions for each of these quantities, therefore

$$
\begin{aligned}
\partial_\parallel n^{BC} &= 0 \\
\partial_\parallel T_e^{BC} &= 0 \\
\partial_\parallel T_i^{BC} &= 0 \\
\partial_\parallel \omega^{BC} &= 0
\end{aligned}
\tag{4.2}
$$

No boundary conditions at targets are instead required for the electric potential, neither from the physical nor from the numerical point of view, as it can be seen from equations 3.31 where only derivatives in the direction perpendicular to the axial coordinate are involved.

Finally, boundary conditions for any plasma quantity in the direction perpendicular to the axial coordinate are made not relevant, since no solid walls is considered, by moving the computational grid edges far enough from the region in which the actual plasma is formed in simulations.

4.3.2   *Modifications to Differential Operators*

The original modifications introduced in this thesis work on the GBS code, in order to adapt it to a linear plasma device configuration, will start being presented here.

The first modification which was carried out on the GBS code is the introduction of a straight and constant equilibrium magnetic field in the simulation setup. As already seen in section 3.2.1, the GBS code allows to load the equilibrium configuration by specifying the sign of the main magnetic field component along the z direction of the cartesian reference system and by defining the magnetic flux distribution in the perpendicular $x-y$ plane in order to define the perpendicular components of the magnetic field.

In our case, given the simple equilibrium magnetic field employed, we didn't exploit this last feature. Since the magnetic field enters explicitely the equations governing the physical system in GBS (see section 3.2.2) only by influencing the differential operators appearing in them, we decided to directly modify their definitions in the code in a coherent way with respect to the chosen equilibrium magnetic configuration.

In our simulation setup, considering the $x-y-z$ cartesian reference frame defined in 3.2.1, the employed equilibrium magnetic field can expressed as

$$\mathbf{B} = (0, 0, B_0) \tag{4.3}$$

with $B_0 = 0.1\ T$. Taking as a reference figure 4.1, this means the magnetic field is straight along the cylindrical chamber and directed from the left target to the right target. Given this, the following expressions for the differential operators in the system can be straightforward derived

$$
\begin{aligned}
\nabla_{\parallel} f &= \partial_z f \\
C(f) &= 0 \\
\nabla_{\parallel}^2 f &= \partial_{zz} f \\
\nabla_{\perp}^2 f &= \partial_{xx} f + \partial_{yy} f \\
[\Phi, f] &= [\Phi, f]_{xy} = \partial_x \Phi \partial_y f - \partial_x f \partial_y \Phi
\end{aligned}
\tag{4.4}
$$

4.3.3   *Removal of Periodicity in the Axial Direction*

The second modification which needed to be applied to GBS was the removal of the periodicity assumption in the axial direction, identified by the z coordinate in the code. Indeed, as it was explained in section 3.2.1 and 3.2.4, the GBS code intrinsically assumes periodicity in the system in the z direction and technically this implies that an automatic MPI communication is carried out copying in the first and last layers of ghost cells in the z direction the values contained in "real" cells on the extreme opposite side. As a consequence of this modification, suitable structures, not originally present in the code, must be introduced to compute boundary conditions at targets and impose the corresponding correct values in the external layer of ghost cells in the z direction.

In order to carry out these modifications the following steps were performed:

- first the MPI functions managing parallelization were modified. Communications between the first and the last layer of sub-domains in the z direction were inhibited.

- the definitions of the staggered n-grid and v-grid (see section 3.2.1) in the z direction were modified so that now the coordinates referring to solid walls in the axial direction are placed on the first and the last "real" points of the n-grid. This is shown in figure 4.6. This choice was carried out as in this way
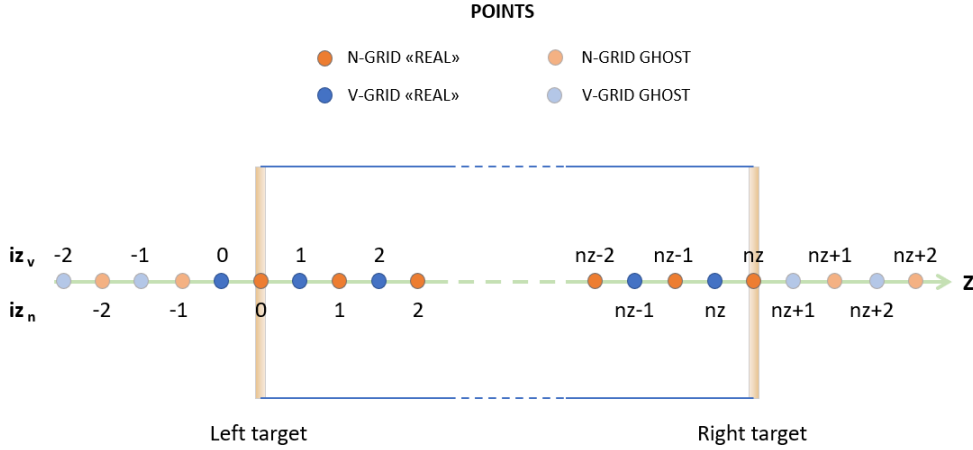
POINTS

- N-GRID «REAL»
- N-GRID GHOST
- V-GRID «REAL»
- V-GRID GHOST

Figure 4.6: Modified GBS staggered z grid. Only the most external points at each side of the domain are represented. Indexes iz_v and iz_n refer to the v-grid and n-grid points respectively. The distance between two subsequent points in each grid is $dz = L_\parallel / n_z$, where $L_\parallel$ is the length of the simulation setup.

the electric potential Φ, involved in the definition of the boundary condition for $V_{\parallel,e}$, would have been free to evolve up to the targets without applying any artificial extrapolation to evaluate it at those positions, as it doesn't have any boundary condition in the z direction (see section 4.2.1).

- suitable structures were implemented to compute boundary conditions values for the different GBS variables at each target in the axial direction. These structures are composed by different routines which, taking into account actual plasma quantities values in the system, are able to evaluate the expressions for the boundary conditions as reported in section 4.2.1.

- suitable structures were also implemented to assign the correct values to each different plasma quantity in cells outside the physical domain in the simulation, that is the first and last layer of ghost cells in z direction for the n-grid and the first and last layer of ghost cells and the first "real" cell in the z direction for the v-grid, as shown in figure 4.6. For plasma quantities defined on the n-grid, that is density, ions and electrons temperature and vorticity, for which homogeneous Neumann conditions are considered, this is straightforward and follows exactly the strategy described in section 3.2.4 imposing $f_{BC} = 0$. For quantities defined on the v-grid, that is ions and

electrons parallel velocities, for which Dirichlet conditions are considered, using as a reference the notation in figure 4.6, the following scheme is applied

$$
\begin{cases}
f_0 = \min(f_{BC}^{left}; \; 2f_{BC}^{left} - f_1) \\
f_{-1} = \min(f_{BC}^{left}; \; 2f_{BC}^{left} - f_2) \\
f_{-2} = f_{-1}
\end{cases}
\qquad
\begin{cases}
f_{n_z+1} = \max(f_{BC}^{right}; \; 2f_{BC}^{right} - f_{n_z}) \\
f_{n_z+2} = \max(f_{BC}^{right}; \; 2f_{BC}^{right} - f_{n_z-1})
\end{cases}
$$

(4.5)

where $f = V_{\parallel,e}, V_{\parallel,i}$ and the corresponding f_{BC} are defined as stated in section 4.3.1. It is important to recall that, for both $V_{\parallel,e}$ and $V_{\parallel,i}$, it holds $f_{BC}^{left} < 0$ and $f_{BC}^{right} > 0$. On an additional note, we underline that the cell with index 0 on the v-grid is a "real" cell, meaning that its value will be updated by the GBS code automatically at each time step according to transport equations, before getting overwritten by routines imposing boundary conditions. This scheme is basically extrapolating the values of cells on the v-grid outside the physical domain in the simulation so that corresponding plasma quantities at targets positions are exactly equal to the imposed boundary condition. The min and max functions triggers when the local slope between subsequent points at targets positions would become negative, cutting off the original values to be set on those points and setting them equal to f_{BC}. An example of this feature is shown in figure 4.7 and in this way the boundary conditions imposition proved to be more robust from the numerical side for these quantities, since the slope for both $V_{\parallel,e}$ and $V_{\parallel,i}$ is expected to be positive along the z direction, reducing local oscillations arising from the extrapolation. This of course implies a small error is accepted on the extrapolated value for these quantities at the targets positions when cutoffs trigger.

- in addition, coherent changes had to be introduced also in other structures already present in the code which were previously exploiting the periodicity assumption. This includes diagnostic, profiles initialization, output generation and restart routines among the most important ones.

4.3.4 *Sources and Initial Profiles Definition*

In the GBS simulation three different sources/sinks were implemented in the transport equations. Their profiles are extracted from the post-processing of a preliminary SOLPS simulation, as it'll be described in details in section 5.1.2. The idea here is defining constant sources/sinks, derived from the equilibrium profiles in SOLPS when a steady-state solution is reached, to be passed to GBS. They will drive the evolution of the different plasma quantities until a balance is reached between these different sources/sinks, the turbulent transport and the losses at the solid targets in the axial direction. These sources are not therefore evaluated self-consistently from GBS.

The three different implemented sources, along with the motivation for which they were included, are the following:

- a source term for density is applied in the continuity equation and this is related to *ionization density rate* in the system. This term couldn't be evaluated directly in the GBS simulation as neutrals module is not employed
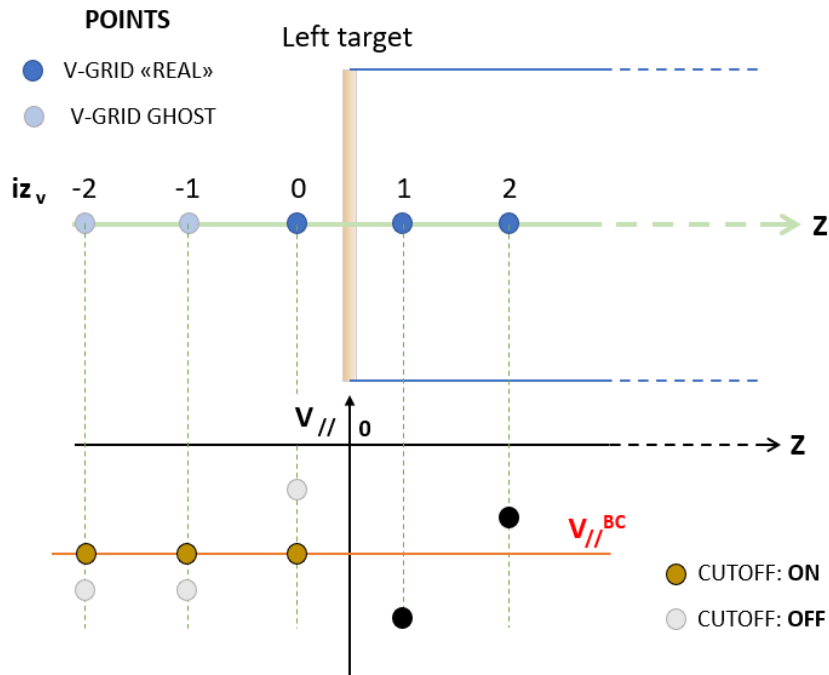
Figure 4.7: A practical example showing the effect of a cutoff in $V_{\parallel,e}$ and $V_{\parallel,i}$ boundary conditions imposition. $V_{\parallel,e}$ and $V_{\parallel,i}$ values are negative near the left target and so is their boundary condition. Their slope is expected to be positive inside the simulated physical domain. When the cutoff triggers, oscillations are sensibly reduced and the code results more robust from the numerical side.

and therefore this input must have been necessarily provided by a previous SOLPS simulation.

- a sink term for electron temperature is applied in the electron energy balance and this is related to *ionization* and *excitation of neutrals* in the system. Also this term couldn't be evaluated directly in the GBS simulation for the same reason described above.

- a source term for electron temperature is applied in the electron energy balance and this is related to the *ECRH mechanism* (see section 4.2.2). This term could have been introduced directly in the corresponding equation employing the same modeling defined in section 4.2.2, but we decided to extract it from a previous SOLPS simulation to be consistent with the definition of the sink term in the same equation. More details on this will be provided in section 5.1.2.

We underline that this choice, for the set of sources to be implemented in GBS simulations, is still missing some mechanisms which could play a non-negligible role in the chosen simulation setup. Among them, the most relevant is ions-neutrals friction, which is known to have an important role in this kind of configuration [23].

As previously stated, the sources introduced in the GBS equations for density and electron temperature characterize the steady-state profiles of a preliminary

SOLPS simulation. For this reason, initial profiles in the GBS simulation for these two quantities are defined so that they recover at least the same order of magnitude with respect to the results obtained in the preliminary SOLPS simulations (see section 5.1.1) inside the approximate region where these sources are defined (see section 5.1.2). Outside this region a lower value for these two quantities is defined and a steep tanh profile in the radial direction mediates the transition between the two different values. These profiles are shown in figure 4.8. This choice also helped in making the GBS simulation more stable from the numerical side.

Other quantities for which a peculiar initial profile is imposed are ions and electrons parallel velocities. In this case again a double tanh profile along the z direction mediates the transition from the value of $-c_{s0} = \sqrt{T_{e0}/m_e}$ at the left target to $+c_{s0}$ at the right target imposing a 0 velocity at the center of the simulated domain. Also these profiles are shown in figure 4.8. This is done in order to impose an initial profile for parallel velocities which is coherent with the boundary conditions applied at targets. As in the initial state $V_{\parallel,e}$ is imposed to be equal to $V_{\parallel,i}$, this implies no current is assumed to be present in the simulation at the beginning.

In any other case initial profiles are defined as uniform in the simulated domain. The long term evolution of the system is indeed expected to be independent from initial conditions in a GBS simulation in general, but rather it will be driven by the implemented sources/sinks [89]. At the same time, this strategy allows initial profiles for quantities different from parallel velocities to match their homogeneous Neumann boundary conditions at targets.
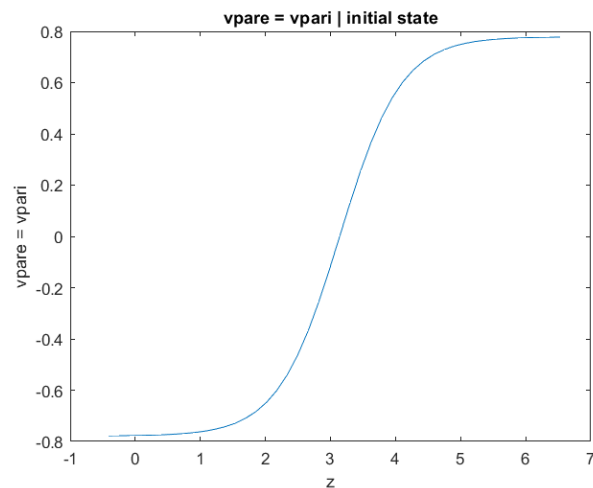
Finally, for any quantity, a small 3D random noise is added to initial profiles to seed plasma turbulence.
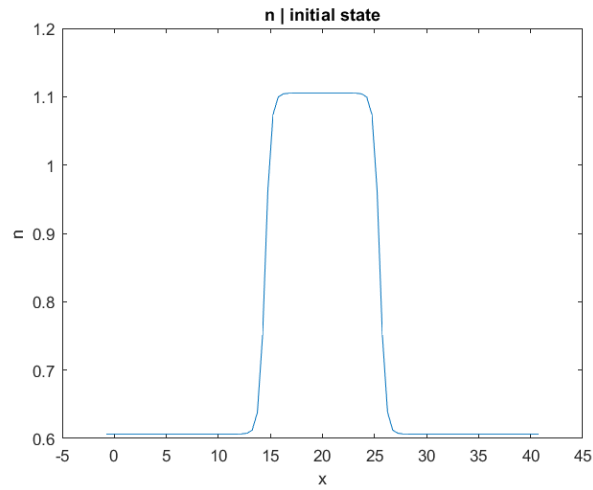
(a) Plasma density.
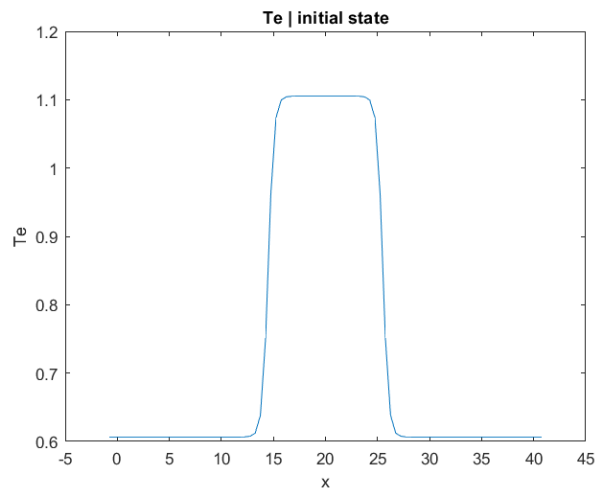
(b) Electron temperature.

(c) Electrons and ions parallel velocity.

Figure 4.8: Peculiar initial profiles in the GBS simulation. Quantities are adimensionalized to the values reported in table 5.3. These profiles are taken at the center of the simulated domain.

5 | Simulations Results

In this chapter the results of the simulations of the GyM linear plasma device, carried out with both SOLPS and GBS, will be presented and discussed. The simulation setup for this work, together with peculiar modeling choices and limits for each of the two codes, was described in chapter 4. Together with simulations results, also the required post-processing on both SOLPS and GBS outcomes, to build inputs for each other, will be addressed in detail.

The coupling strategy between the two codes adopted in this thesis work is direct (see section 2.3.3). Its main goal is to allow to run an optimized SOLPS simulation of the chosen simulation setup employing effective diffusion coefficients evaluated self-consistently from a previous GBS simulation. The corresponding work-flow consisted in the following points:

1. a preliminary SOLPS simulation is run using a set of effective diffusion coefficients taken from previous works in literature on the GyM machine using this code [23, 37]. In these studies, they were evaluated from comparisons between experimental results and simulated plasma quantities profiles. The results of this preliminary simulation are employed to build source/sink terms to be added to transport equations in the subsequent GBS simulation, allowing it to take into account neutrals-related effects which can't be self-consistently evaluated (see sections 4.3.1 and 4.3.4).

2. a subsequent GBS simulation including those source/sink terms is run. Its results are used to evaluate a set of radial profiles for effective diffusion coefficients to be adopted in an optimized SOLPS simulation.

3. a final optimized SOLPS simulation is run employing those radial profiles for effective diffusion coefficients.

The structure of this chapter will follow the above work-flow. First the results from the preliminary SOLPS simulation will be presented and commented (§ 5.1.1) together with the corresponding post-processing work carried out to extract sources/sinks needed as inputs for the subsequent GBS simulation (§ 5.1.2).

Then the results from the GBS simulation will be described (§ 5.2.1) and particular attention will be drawn to the analyses of the drifts arising in the simulated plasma (§ 5.2.2). The required post-processing done on GBS results to build the radial profiles for effective diffusion coefficients to be passed to the optimized SOLPS

simulation will be explained (§ 5.2.3).

Finally, the optimized SOLPS simulation results will be presented and compared to those of the preliminary one (§ 5.3.1).

5.1 PRELIMINARY SOLPS SIMULATION

In table 5.1 the input parameters for the first SOLPS preliminary simulation are described. The values of the effective diffusion coefficients are taken from previous works in literature on the GyM machine using this code [23, 37]. In these studies, they were evaluated from comparisons between experimental results and simulated plasma quantities profiles.

Parameter	Value
Density-driven effective particles $\perp$ diffusivity	$D_n = 0.5\ m^2 s^{-1}$
Effective ion thermal $\perp$ diffusivity	$\chi_i = 1.5\ m^2 s^{-1}$
Effective electron thermal $\perp$ diffusivity	$\chi_e = 1.5\ m^2 s^{-1}$
Initial (uniform) densities	$n_{He^{1+}} = 10^{16}\ cm^{-3}$ $n_{He^{2+}} = 10^{16} cm^{-3}$
Initial (uniform) temperatures	$T_i = 7\ eV$ $T_e = 7\ eV$
Exponential decay lengths	$\Lambda_n = 3\ cm$ $\Lambda_{T_e} = 3\ cm$ $\Lambda_{T_i} = 3\ cm$ $\Lambda_\Phi = 3\ cm$
Time-step	$\Delta t = 10^{-5}\ s$
Number of points in the axial direction	$n_x = 66$
Number of points in the radial direction	$n_y = 14$

Table 5.1: Input parameters for the preliminary SOLPS simulation.

5.1.1 *Analyses of the Results*

The 2D profiles of different plasma quantities resulting from the preliminary SOLPS simulation are reported in figure 5.1. In addition, the corresponding 1D plots in radial and axial direction, taken respectively at $0.02\ m$ and $0.5\ m$ in the notation used in these figures, are also provided. They are shown in figures 5.2 and 5.3 respectively. Finally the plasma velocity field is shown in figure 5.4, where in this case the radial profile for its magnitude was taken at the left target, corresponding to an axial coordinate of $1.03\ m$ in the notation used in these figures. A few interesting comments can be done regarding these results.

The *electrons temperature* presents an almost constant axial profile with a small peak corresponding to the center of the ECRH source, modelled as a gaussian distribution in the axial direction as described in section 4.2.2. In the radial direction it presents a quite constant profile up to larger radii where, after showing a small peak, it decreases exponentially due to the imposed boundary condition (see section 4.2.3). The peak can be ascribed to the combined effects of a constant imposed power

density deposition, due to the ECRH source, and a monotonic drop in electrons density in the radial direction. The flat profile of T_e in the radial direction near the axis of the configuration is expected since symmetry boundary conditions are assumed at $r = 0$.

The *ions temperature*'s value is of the order of 0.1 eV, consistently reproducing the cold ions temperature expected in GyM. This is because the external power source is providing energy directly to electrons and the low plasma density is strongly inhibiting thermal equilibration mechanisms [23]. Further studies should be carried out to investigate the peaks in its values at axial targets.

About the *electrons* and *ions densities* we recall quasi-neutrality is imposed so the electrons and the sum of the ions densities must be equal. As it can be seen the value of He^{2+} density is 3 orders of magnitude smaller than that of He^{1+} and can be considered negligible. This is due to the low electrons temperature in the system [23], not allowing electrons to ionize efficiently the neutrals in the system. Along the axial direction their profiles show a drop near targets thanks to the sink action of solid surfaces. In the radial direction densities, as well as T_e, show an initially constant profile, thanks to the symmetry boundary conditions at $r = 0$. At larger radii a smooth drop is observed, correlated again with the boundary conditions imposed at the outer radius and imposing an exponential decay for these quantities. The *neutrals density* is approximately uniform, since a low ionization degree characterizes the system. This uniform distribution is then slightly decreased in the regions where the plasma density is higher. Peaks for its value can be seen at targets, where recycling from ions fluxes impacting on solid walls and a lower plasma density is present.

Plasma velocity is increasing and directed towards solid targets at which it gets to the value of local plasma sound speed thanks to the imposed Bohm boundary condition (see section 4.2.3). This fact is also shown in figure 5.4 by the radial profile of velocity magnitude at the left target, which follows qualitatively the behaviour of T_e in the radial direction.

5.1.2 *Extraction of Neutrals-Related Sources*

Once the results from the preliminary SOLPS simulation are provided, it is possible to extract the profiles of some important source/sink terms to be passed to GBS and to be included in its transport equations as constant terms. These terms have been described in detail in section 4.3.4. In this section the process to extract them from SOLPS results and the required post-processing to add them into GBS transport equations are presented.

Each source/sink term can be extracted from the corresponding balance in the SOLPS results. Indeed, SOLPS outcomes already include a file called `balance.nc` from which it is possible to access different source and sink terms in balance equations, including plasma particles and electrons energy ones, characterizing the final-steady state of the simulation. In our case: (a) from plasma particles balance, we extract the ionization rate, (b) from electrons energy balance, we extract the external power contribution and electron power losses (see section 4.3.4). These terms are computed for each cell in the B2.5 mesh and they must be divided by the volume of each corresponding cell to rewrite them in terms of particles and
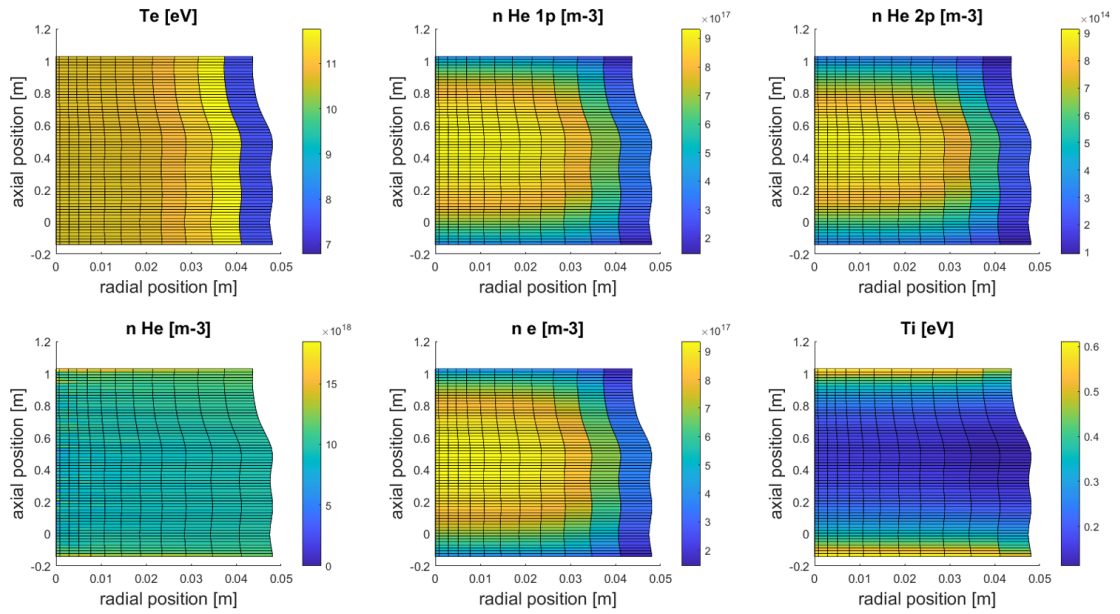
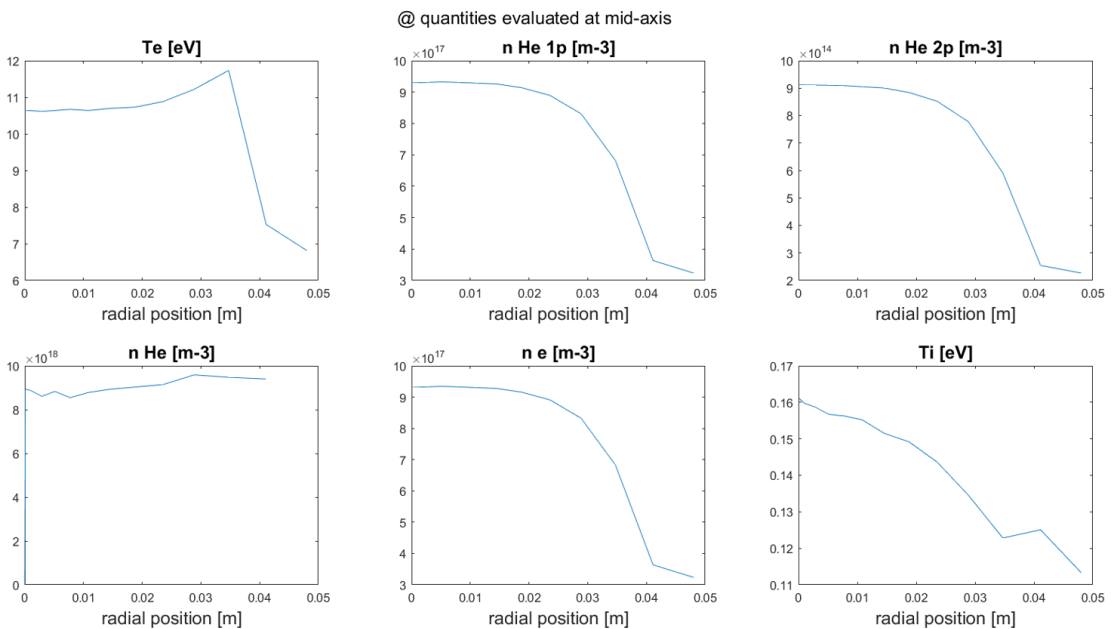**Figure 5.1:** 2D maps of different plasma quantities from the results of the preliminary SOLPS simulation.

Figure 5.2: 1D radial profiles of different plasma quantities from the results of the preliminary SOLPS simulation.
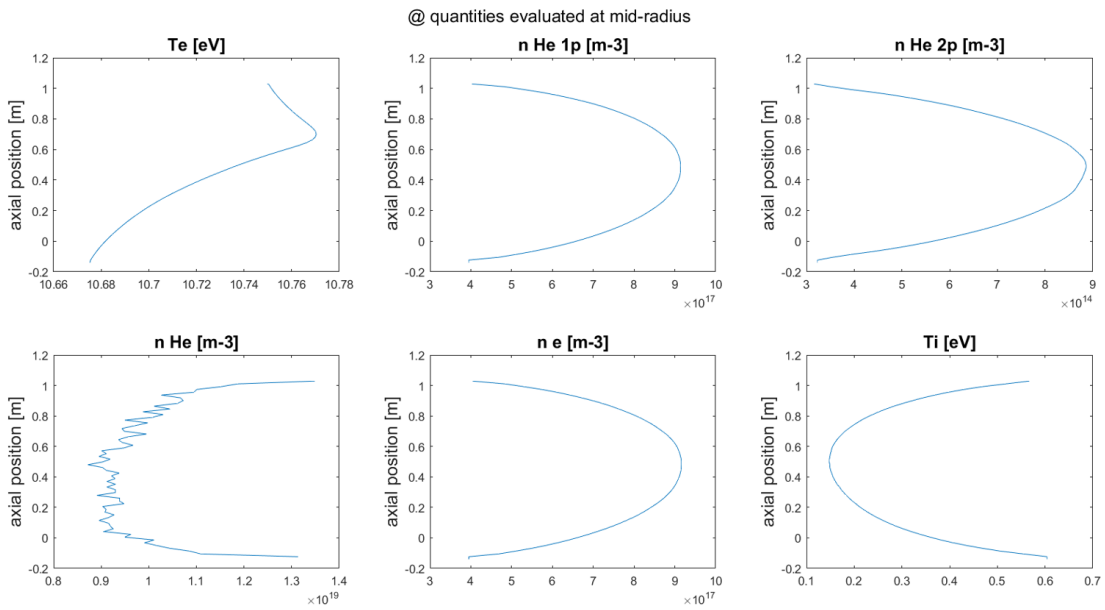
Figure 5.3: 1D axial profiles of different plasma quantities from the results of the preliminary SOLPS simulation.
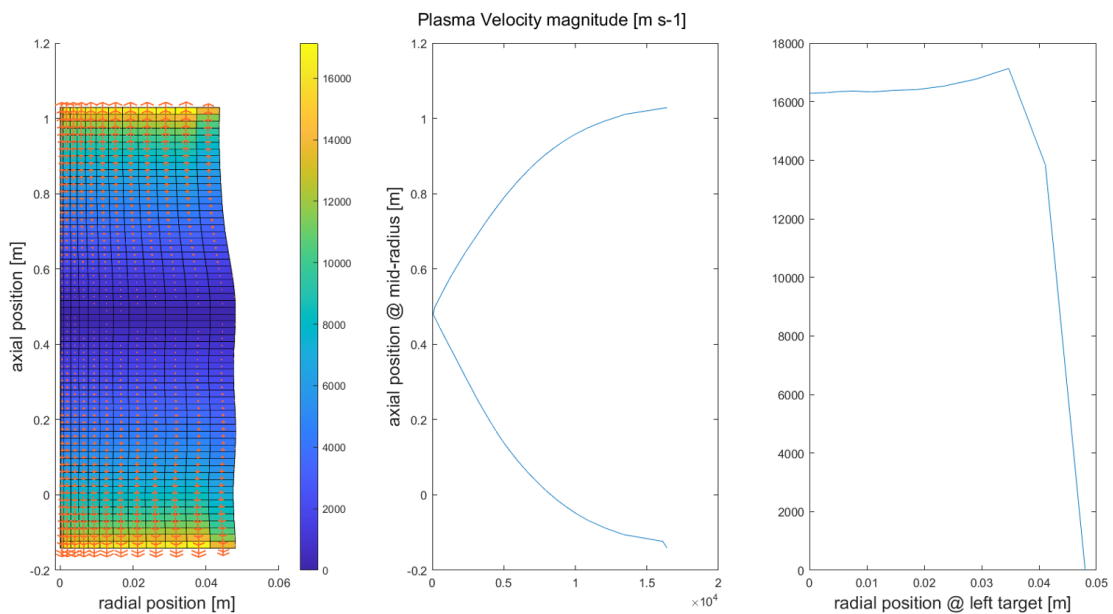

Figure 5.4: Different profiles for plasma velocity from the results of the preliminary SOLPS simulation.

power source/sink densities, as it is needed in transport equations. The profiles of the three sources/sinks densities of interest for our case are reported in figures 5.5, 5.6 and 5.7, respectively representing ionization density rate for ions and external power density and power density losses for electrons.
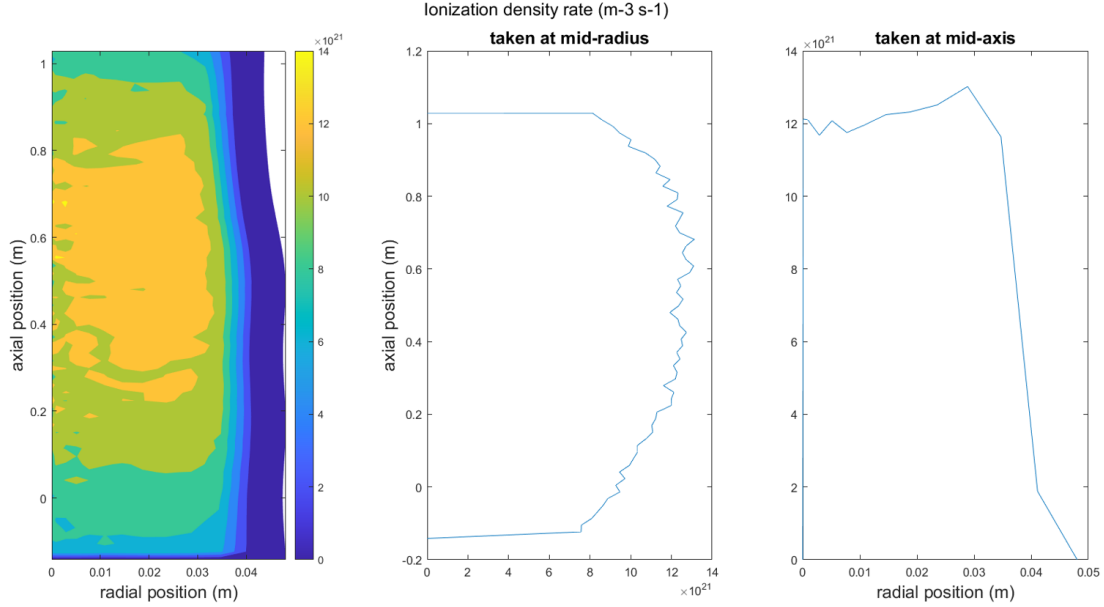

Figure 5.5: Ionization density rate from the preliminary SOLPS simulation.

The next step in the post-processing of the preliminary SOLPS simulation is the implementation of those sources as constant terms in GBS equations.

Before describing this process, it must be underlined here more precisely that our aim is to define constant terms to be included at the right hand side of the expressions employed to update plasma quantities from time-step n to time-step $n+1$ in the adopted explicit time-advancing scheme. Therefore, for any plasma quantity f for which this explicit algorithm is applied, including n and T_e, it holds

$$f^{n+1} = f^n + \Delta f^n = f^n + (RHS_0)^n * \Delta t + S_f * \Delta t \qquad (5.1)$$

where the $(RHS_0)^n$ term is evaluated from the original transport equations implemented in GBS at time-step n and S_f are the external constant sources to be defined. While this specification is needless for the ionization density rate, it is important for the power density source and sink defined above because, as it can be seen from the energy balance equation in equations 2.9, they must be divided by $3/2 \, n_e$ to be applied at the right hand side of the equation for T_e^{n+1}. This computation was performed employing the steady state electron density obtained from the preliminary SOLPS simulation.

At this point the following actions are needed to implement the extracted terms into GBS:

- the extracted terms are adimensionalized employing the reference values chosen for the GBS simulation (see table 5.3).
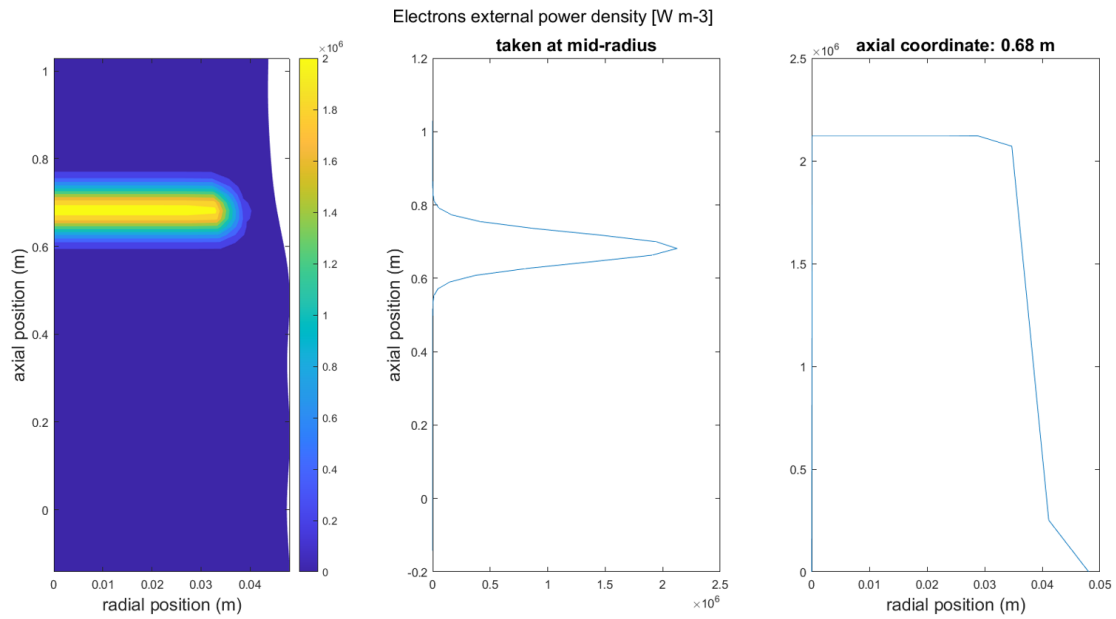
Figure 5.6: Electrons external power density source from the preliminary SOLPS simulation.
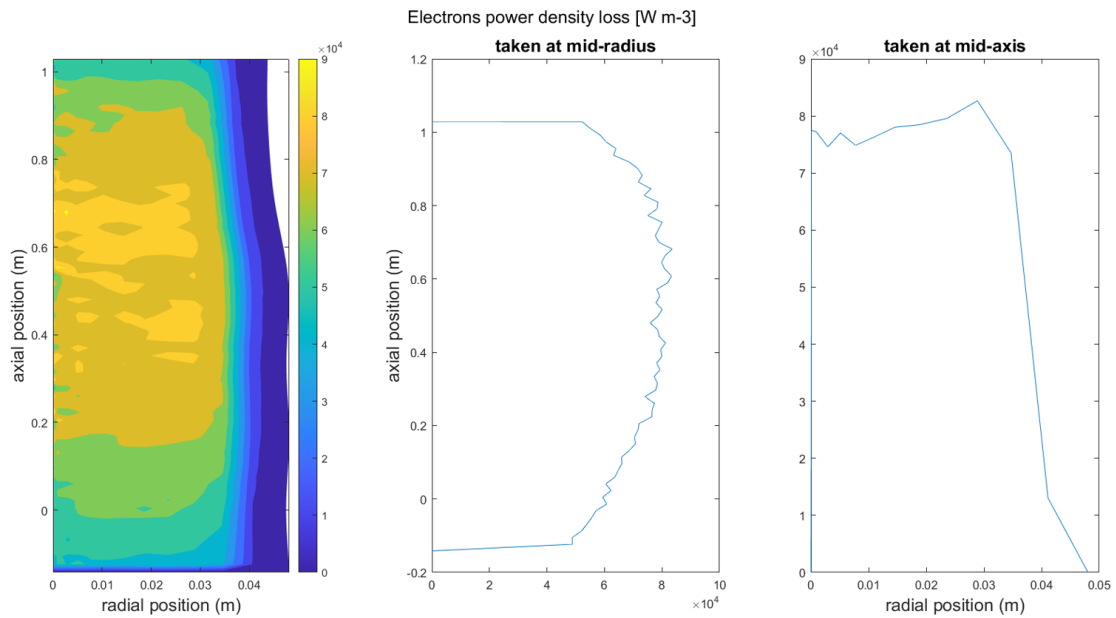

Figure 5.7: Electrons power density losses from the preliminary SOLPS simulation.

- relatively simple fit are used to approximate the adimensional source/sink terms with analytical expressions. This fitting procedure is carried out by assuming the 2D profiles for each source can be rewritten as the product of two factors, one dependent only on the axial coordinate and one dependent only on the radial coordinate, and evaluating them separately by fitting the corresponding axial and radial profiles. Simple tanh profiles are imposed in the radial direction while low degree polynomials or gaussian profiles are imposed in the axial direction. The axial profiles are evaluated at a radius of $0.02\ m$ for each term. The radial profiles are evaluated at an axial coordinate of $0.5\ m$ for the electrons power density loss and for the ionization density rate and at the center of the ECRH source in the axial direction for the electrons power density source, corresponding to an axial coordinate of $0.68\ m$.

  This approach for the fitting procedure was chosen in order to keep the analytical expressions for these terms as simple as possible. Nevertheless its outcomes are in good agreement with the original profiles, maintaining relative errors $< 10\%$ in almost any point of the simulation domain. Some localized peaks in relative errors are present near targets and at outer

- these analytical expressions are added in the corresponding GBS routines to advance in time n and T_e.radii.

The results of this fitting procedure are reported in figure 5.8, 5.9 and 5.10 for the ionization density rate, the electrons external power density source and the electrons power density loss respectively. It must be underlined that quantities are expressed in GBS code units (see table 5.3). In particular z is the coordinate for the axial direction, where $z = 0$ and $z = 2\pi$ correspond to the coordinates of the left and right target in the configuration respectively. The radial coordinate r is instead computed from the center of the $x - y$ cartesian grid, located at $(x, y) = (20, 20)$.

5.2   GBS SIMULATION

The GBS simulation is run including the three sources extracted from the preliminary SOLPS simulation, as described in section 5.1.2. The reference values for different quantities chosen for the simulation are reported in table 5.2.

Quantity	Reference value
Density	$n_0 = 5 \cdot 10^{17}\ m^{-3}$
Electron temperature	$T_{e0} = 10\ eV$
Magnetic field intensity	$B_0 = 0.1\ T$
Parallel length	$L_\parallel = 1.18\ m$

Table 5.2: Reference values chosen for the GBS simulation.

With these quantities it is now possible to evaluate the adimensionalization factors for different quantities in GBS. These are reported in table 5.3. From now on all the results from the GBS code will be reported in the so-called *code units*, that is adimensionalized by these factors, except when explicitly specified otherwise. This

Figure 5.8: Ionization density rate fit to be implemented in the GBS code. Quantities are expressed in GBS code units (see table 5.3).
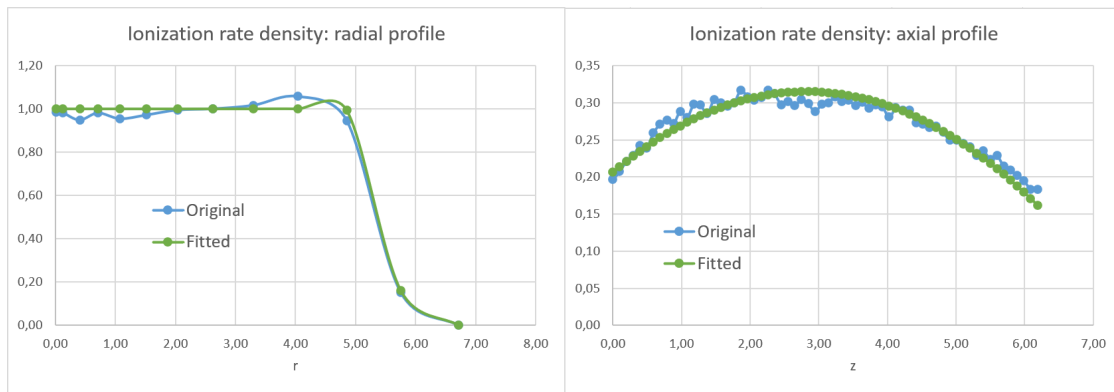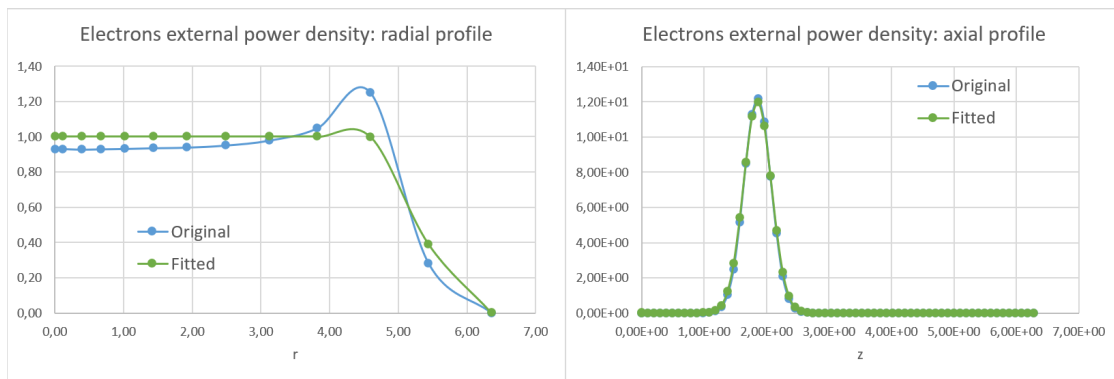

Figure 5.9: Electrons external power density fit to be implemented in the GBS code. Quantities are expressed in GBS code units (see table 5.3).
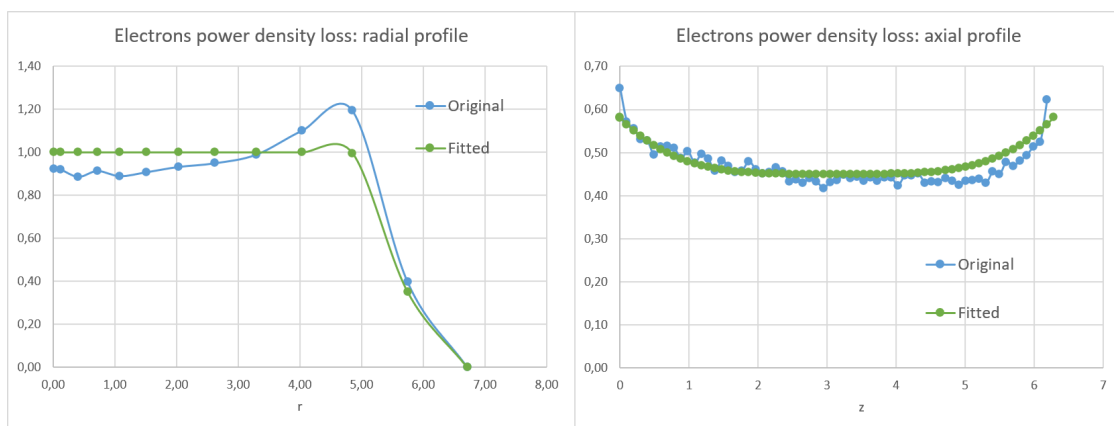

Figure 5.10: Electron power density loss fit to be implemented in the GBS code. Quantities are expressed in GBS code units (see table 5.3).

choice is employed as it is the standard convention for GBS results in literature [15, 24, 45]. Expressing results directly with these code units, based on characteristic plasma and turbulence scales, can help in some cases to have a more direct physical interpretation of profiles.

Quantity	Adimensionalization factor	Value
n	Reference density n_0	$5 \cdot 10^{17} \ m^{-3}$
T_e	Reference electron temperature T_{e0}	$10 \ eV$
$\parallel$ length	Normalized reference parallel length $R_0 = L_{\parallel}/2\pi$	$0.19 \ m$
$V_{\parallel}$	Plasma sound speed $c_{s0} = \sqrt{T_{e0}/m_{He}}$	$1.55 \cdot 10^4 \ m \ s^{-1}$
$\perp$ length	Ion sound Larmor radius $\rho_{s0} = c_{s0}B_0 e/m_{He}$	$7.2 \cdot 10^{-3} \ m$
t	Characteristic parallel time $t_0 = R_0/c_{s0}$	$1.21 \cdot 10^{-5} \ s$
Φ	Reference potential $\Phi_0 = T_{e0}/e$	$10 \ J/C$

Table 5.3: Adimensionalization factors for the GBS simulation. Parallel and perpendicular directions are taken with respect to the main magnetic field component direction and, therefore, they refer to z and $x - y$ directions respectively in the GBS reference frame (see section 3.2.1)

The main simulation parameters for GBS are shown in table 5.4. The discretization of the cartesian grid influences the chosen time-step, as an higher resolution implies a lower time-step to be used. A compromise between these parameters is done so that resolution is increased as much as possible maintaining a reasonable time to run the simulation. As a reference, a GBS simulation with these parameters takes around 70 h to run completely. The dimension of the cartesian grid in the perpendicular plane, that is the $x - y$ plane, is set so that the plasma evolves far from the edge of the grid (see figure 5.8). In this way boundary conditions imposed in $x - y$ direction don't influence the plasma evolution. Values for artificial perpendicular diffusivities, added in transport equations just for numerical stability reasons (see section 3.2.2), are set so that they'll be at least one order of magnitude lower than the corresponding effective diffusivities set in the preliminary SOLPS simulation. Indeed, it was found that running a simulation in GBS with a value for these parameters equal or larger than those diffusivities would inhibit turbulence in the system. Finally, the simulation was carried out discretizing the system in 20 sub-domains in the z direction and 8 and 6 sub-domains in the x and y direction for parallelization (see section 3.2.4).

5.2.1 *Analysis of the Results*

Some snapshots of the instantaneous profiles of different plasma quantities are reported in figures 5.11, 5.12, 5.13, 5.14 and 5.15. We recall ion temperature is not

Parameter	Value (code units)
Artificial perpendicular diffusivity (any quantity)	$D_\perp = 0.01$
Time-step	$\Delta t = 5 \cdot 10^{-5}$
Points in the perpendicular $(x - y)$ direction	$n_\perp = 80$
Points in the axial (z) direction	$n_z = 40$
Grid dimension in the perpendicular $(x - y)$ direction	$L_\perp = 40$

Table 5.4: Input parameters for the GBS simulation.

evaluated and ions are considered cold. T_i is therefore set to a uniform and low value all over the simulation domain.

Turbulent structures can be observed, particularly elongated in the parallel direction. This is expected in a linear configuration. This is especially true for electron parallel velocities, as it can be seen in figure 5.13. The elongated patterns present in the axial direction suggests turbulence is promoting the formation of independent plasma filaments, extending for a large part of the axial length of the machine, allowing electrons to reach large velocities inside them. The electrons parallel velocities are also characterized by a strong shear.

Shorter turbulent structures are also developing in the radial direction, bent by the plasma rotation in the corresponding region (see section 5.2.2). They can be seen, for example, in density and electrons temperature profiles, in figures 5.11 and 5.12. They drive the plasma expansion, from the fairly homogeneous central agglomerate, beyond the radius of the plasma sources (see figure 5.8).

In order to compare the results from the GBS simulation to those of the preliminary SOLPS one, an averaging procedure in time and in the polar direction of each field was carried out on the different plasma quantities. This allows to evaluate 2D average fields in the radial and axial direction. Note that the radial direction is measured from the center of the perpendicular plane, that is the point $(x, y) = (20, 20)$. The results are shown in figures 5.16, 5.17, 5.18, 5.19 and 5.20. For each profile, the corresponding *mean square root deviation*, or *RMSD*, is also plotted. RMSD is evaluated for each given quantity f as

$$RMSD_f = \sqrt{\langle f'^{\,2} \rangle_{t,\vartheta}} \tag{5.2}$$

where f' is the fluctuation of the quantity f, that is $f' = f - \langle f \rangle_{t,\vartheta}$. From these results it is possible to see that fluctuations peak in the region around the radius up to which the plasma sources extends (see figure 5.8), roughly $r \sim 6$ in GBS code units, that is the region from which the perpendicular turbulent structures develop. The fluctuation level peaks in the region ranging from $r \simeq 4$ to $r \simeq 8$ in GBS code units, evaluated as the ratio of RMSD to the corresponding average value, reaching values around 30% for any quantity. The only exception is electrons parallel velocity, where the RMSD value is greater than the corresponding average value in many points of the $r - z$ semi-plane as its profile is highly turbulent. In this case the meaning of the average profile is therefore highly questionable.

The comparison between these average profiles and the ones obtained in the preliminary SOLPS simulation shows that the plasma density is underestimated by nearly a factor 2 in GBS and its profile is smoother in the axial direction. As
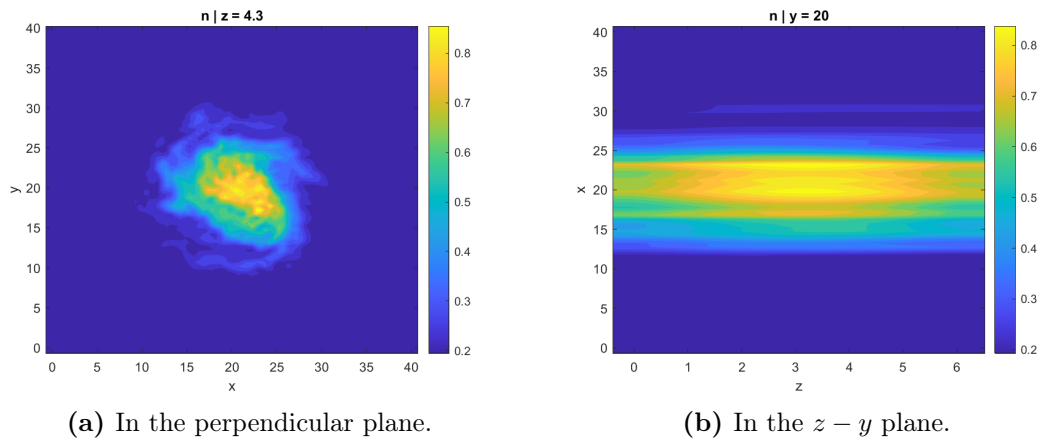
(a) In the perpendicular plane.

(b) In the $z - y$ plane.

Figure 5.11: Instantaneous plasma density snapshot in GBS results. Quantities are expressed in GBS code units (see table 5.3).

(a) In the perpendicular plane.
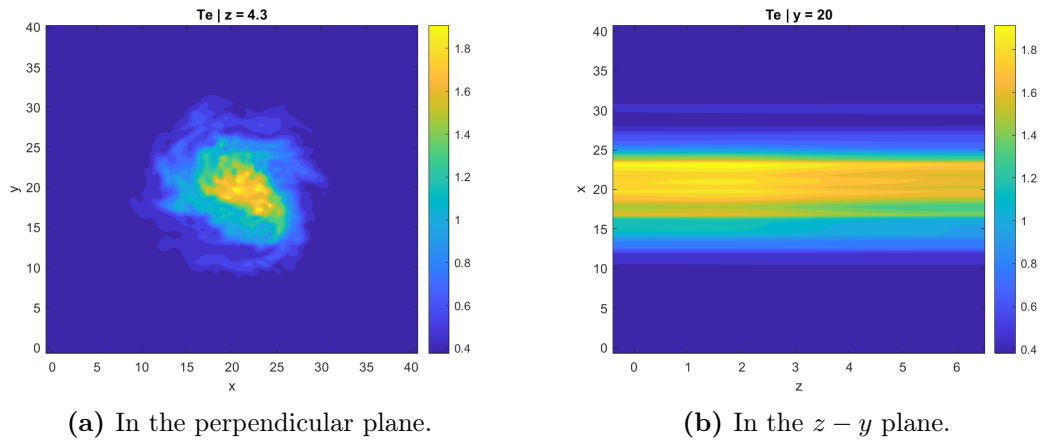
(b) In the $z - y$ plane.

Figure 5.12: Instantaneous electron temperature snapshot in GBS results. Quantities are expressed in GBS code units (see table 5.3).

(a) In the perpendicular plane.

(b) In the $z - y$ plane.

Figure 5.13: Instantaneous electron parallel velocity snapshot in GBS results. Quantities are expressed in GBS code units (see table 5.3).

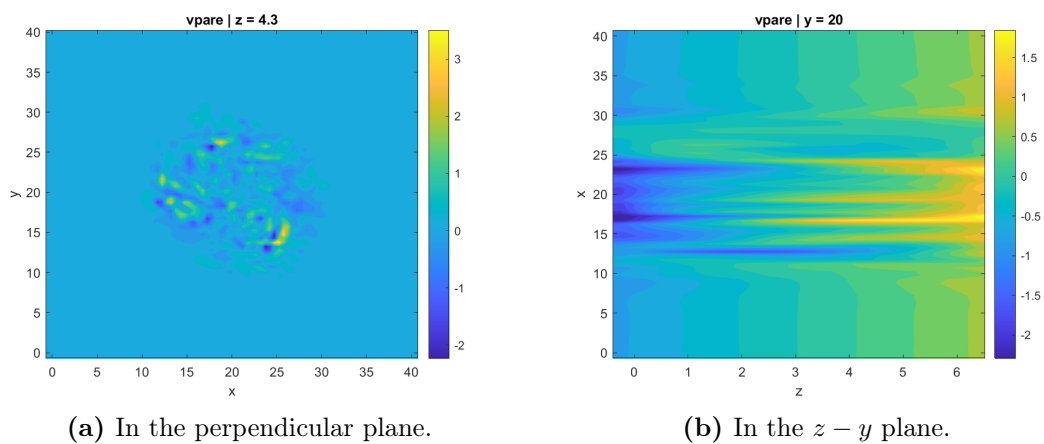**(a)** In the perpendicular plane.

(b) In the $z - y$ plane.

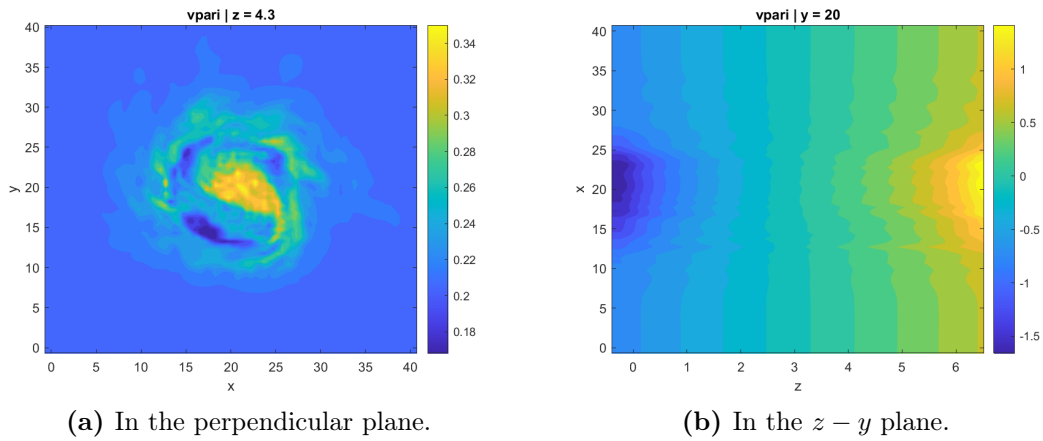**Figure 5.14:** Instantaneous ion parallel velocity snapshot in GBS results. Quantities are expressed in GBS code units (see table 5.3).

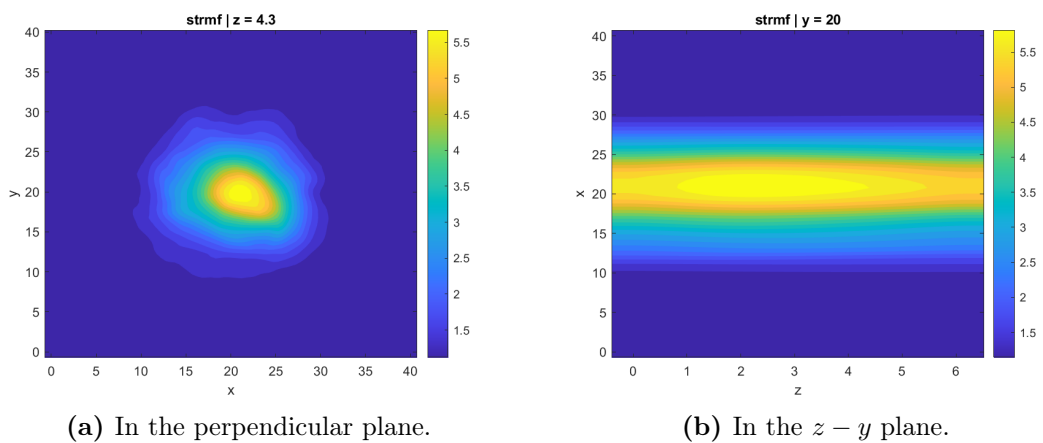**(a)** In the perpendicular plane.

(b) In the $z - y$ plane.

Figure 5.15: Instantaneous plasma potential snapshot in GBS results. Quantities are expressed in GBS code units (see table 5.3).

opposite, the electrons temperature is overestimated in GBS, but its decrease at larger radii proves to be smoother with respect to that observed in SOLPS and its variation in the axial direction is slightly increased. It is also possible to recognize the peak in the axial direction for electrons temperature, related to the center of the external power density source (see figure 5.9). Ions parallel velocities, as expected from the Bohm boundary conditions at targets, evolves between the local plasma sound speeds at the two targets. The different value of the velocity at the targets is due to the different value of electrons temperature. This difference is ascribed to the asymmetry in the axial direction of the electrons external power density source (see figure 5.9).

In addition, also 2D profiles in the $r - z$ semi-plane for the *skewness* of the different analysed quantities are reported in figure 5.21. In particular we represent the normalized cubic root of the skewness, which can be computed for any quantity f as

$$\frac{\sqrt[3]{\langle f'^{\,3} \rangle_{t,\vartheta}}}{RMSD_f} \tag{5.3}$$

This value can measure the asymmetry in the probability distribution function for fluctuations. A positive skewness usually implies the probability distribution function for fluctuations has a longer tail for positive values and therefore f' is more likely to have large positive values with respect to large negative ones. From the results one can observe that skewness patterns are qualitatively similar for each quantity. In any case, around the radius up to which the plasma source extends (see figure 5.8), that is $r \simeq 6$ in GBS code units, and radially outward, skewness is positive[1]. This suggests that a large instantaneous peak for their value is more probable in this region, where perpendicular turbulent structures characterize the shape of the profiles. Instead the opposite trend occurs at low radii, where profiles tend to be more homogeneous, suggesting that large instantaneous drops are more probable.

5.2.2 *Analysis of Drifts*

From the GBS simulation results it's possible to recover the profiles of plasma drifts at each instant in time. Here only the 0th order approximation for the radial plasma velocities [102] will be considered, neglecting the contribution from the ion polarisation drift (see section 3.2.2). In the 0th order approximation only the two following drifts, the $\mathbf{E} \times \mathbf{B}$ and the diamagnetic drifts, are computed

$$\mathbf{V}_{\mathbf{E} \times \mathbf{B}} = -\frac{\nabla \Phi \times \mathbf{B}}{B^2} \qquad \mathbf{V}_{dia} = \frac{\mathbf{B} \times \nabla(nT_a)}{q_a n B^2} \tag{5.4}$$

As for both electrons and ions $\nabla(nT_a)$ is directed radially inward at each point, and so is $\nabla \Phi$, it is possible to predict in advance that the ions diamagnetic drift and the $\mathbf{E} \times \mathbf{B}$ drifts will be in the same direction and opposite to the electrons diamagnetic drift.

This prediction is confirmed by drifts averages in time, presented in figures 5.22, 5.23 and 5.24. Here averages are intended only in time. The average effect of

---

[1]Or, equally, negative in the case of parallel velocities in the regions where their average sign is negative.

(a) Average value.

(b) RMSD.

Figure 5.16: Plasma density in the $r-z$ semi-plane in GBS results. Quantities are expressed in GBS code units (see table 5.3).

(a) Average value.

(b) RMSD.

Figure 5.17: Electrons temperature in the $r-z$ semi-plane in GBS results. Quantities are expressed in GBS code units (see table 5.3).

(a) Average value.

(b) RMSD.

Figure 5.18: Electrons parallel velocity in the $r-z$ semi-plane in GBS results. Quantities are expressed in GBS code units (see table 5.3).

(a) Average value.

(b) RMSD.
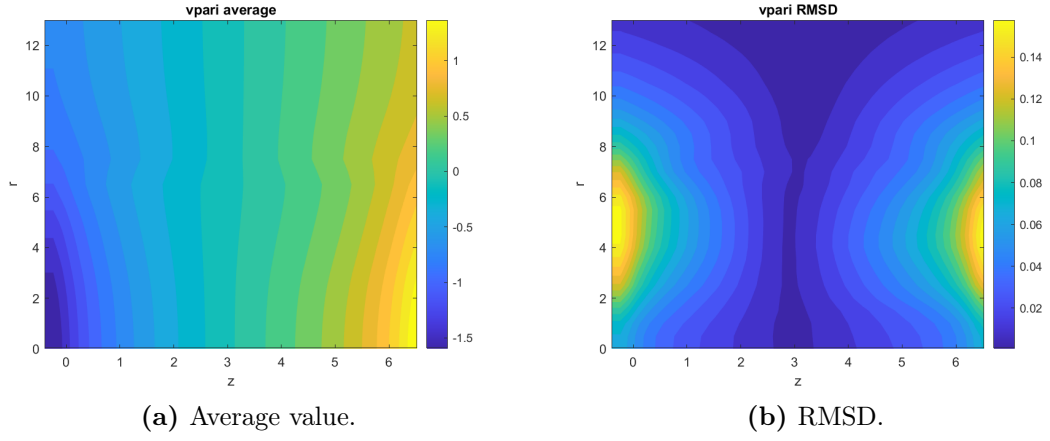
Figure 5.19: Ions parallel velocity in the $r - z$ semi-plane in GBS results. Quantities are expressed in GBS code units (see table 5.3).

(a) Average value.

(b) RMSD.

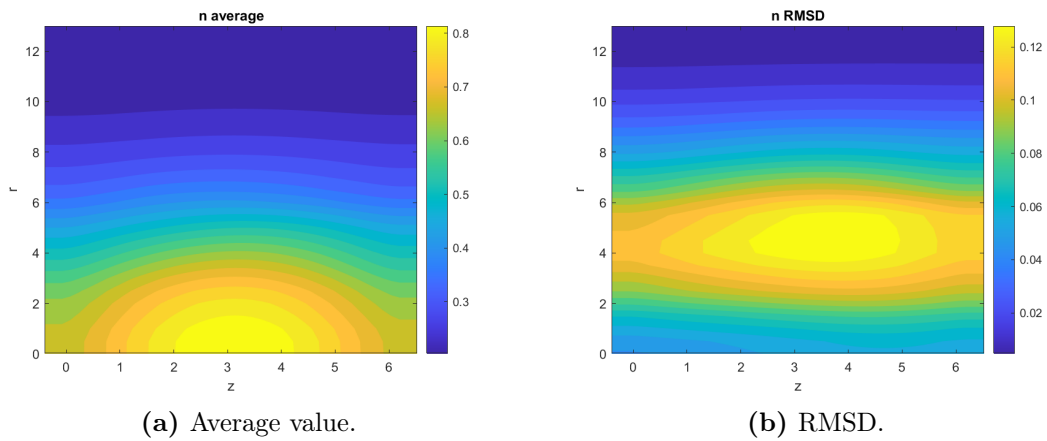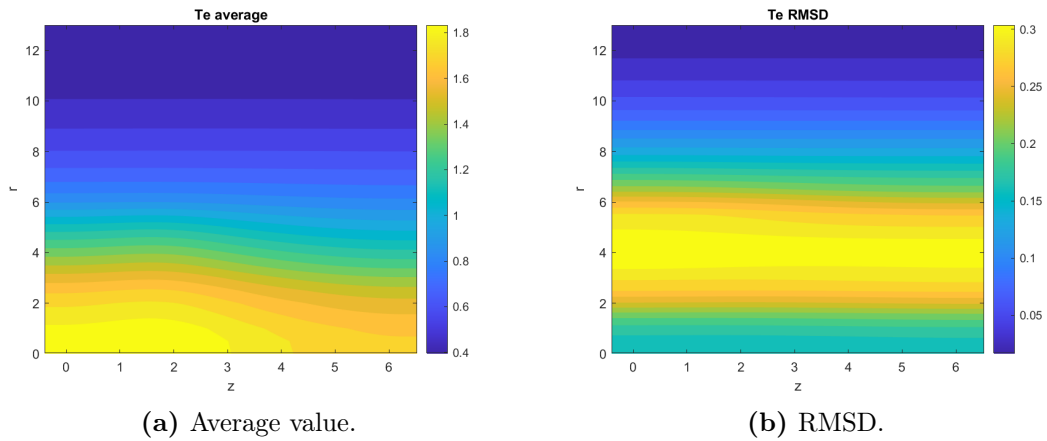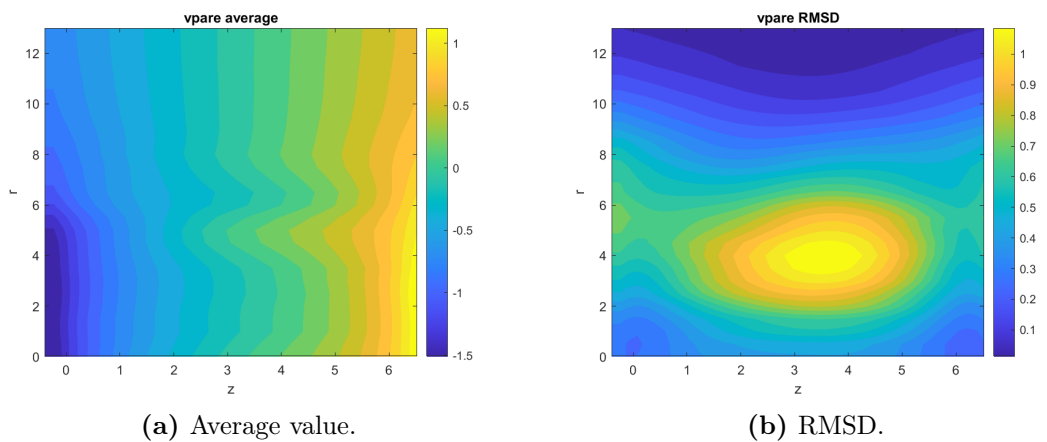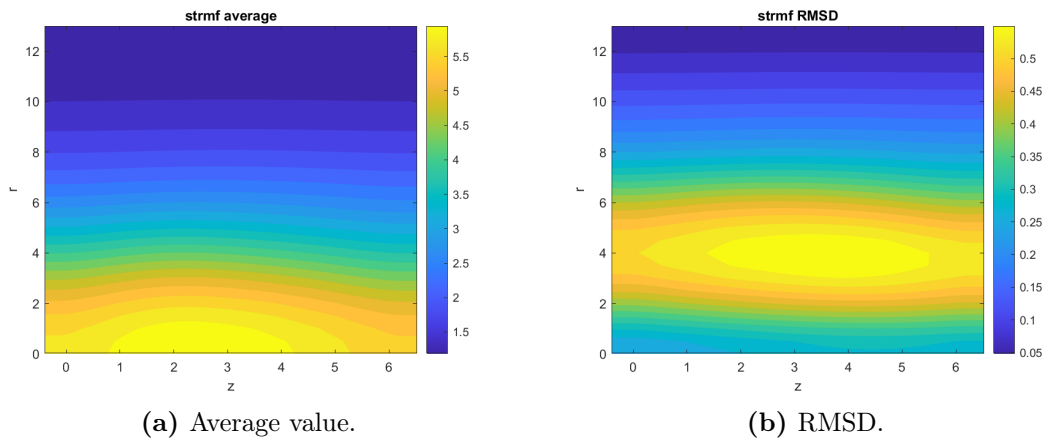**Figure 5.20:** Plasma potential in the $r - z$ semi-plane in GBS results. Quantities are expressed in GBS code units (see table 5.3).

(a) Plasma density.

(b) Electrons temperature.

(c) Electrons parallel velocity.

(d) Ions parallel velocity.

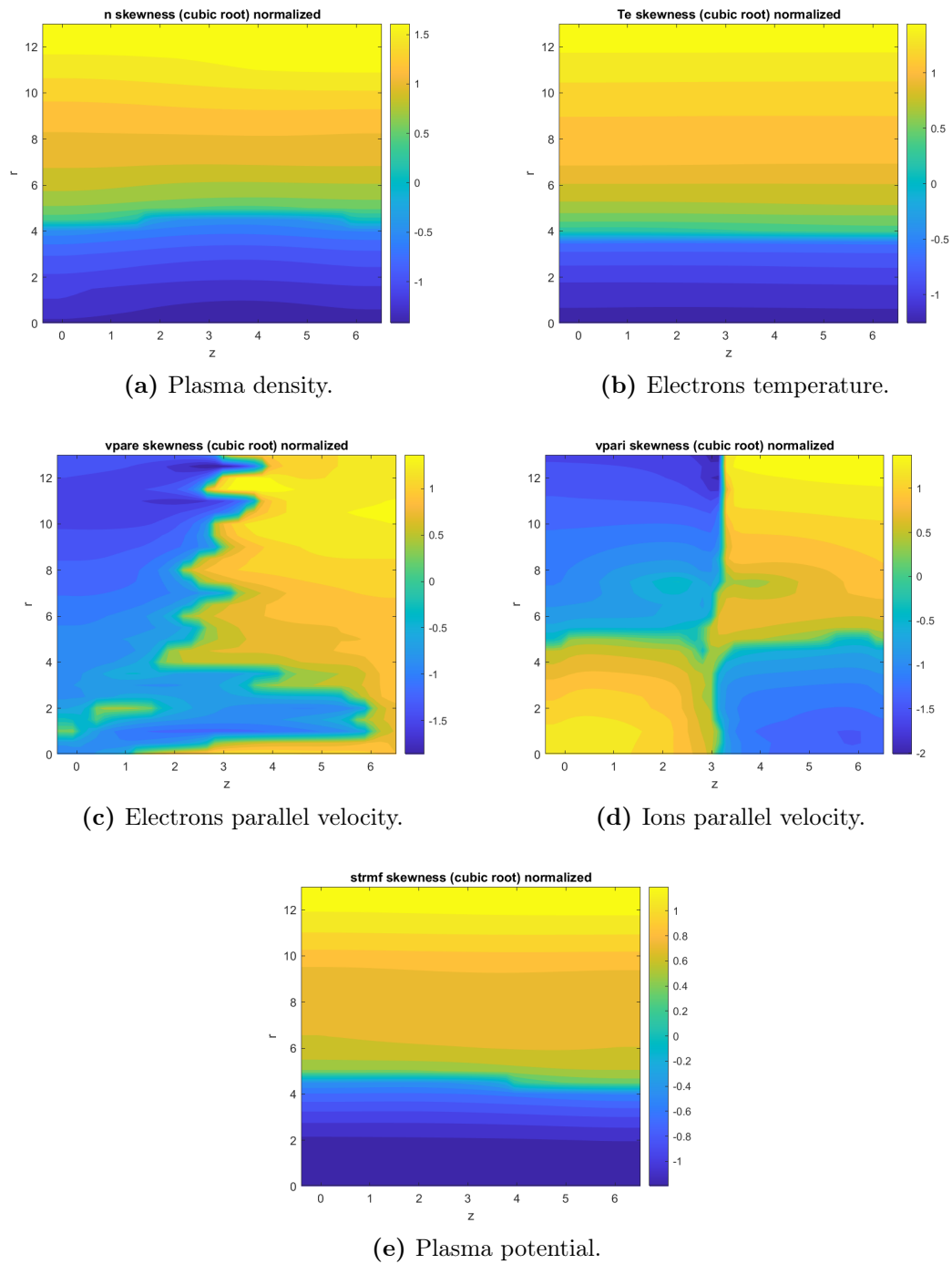

(e) Plasma potential.

Figure 5.21: Normalized cubic root of skewness for different plasma quantities in GBS results.

these drifts, as $\mathbf{B}$ is straight and constant in the axial direction, is the generation of a rotational velocity field in the polar direction. The ions diamagnetic drift is negligible, as T_i was assumed low and uniform. The $\mathbf{E} \times \mathbf{B}$ drift presents a more coherent structure also in its instantaneous profile, as opposite to the electrons diamagnetic drift instantaneous profile which looks more randomly oriented and characterized by some localized peaks in the drift magnitude. This is due to the difference in homogeneity between the instantaneous profiles of Φ and n and T_e, as it can be seen in figures 5.11, 5.12 and 5.15. Nevertheless, on a time average, also the electrons diamagnetic drift profile recovers the expected rotational pattern.

At small radii, the $\mathbf{E} \times \mathbf{B}$ and the electrons diamagnetic drifts almost balance out on average, while approximately from the radius of the plasma sources, that is $r \simeq 6$ in GBS code units (see figure 5.8), and radially outward the $\mathbf{E} \times \mathbf{B}$ term dominates, imposing an overall rotation to the plasma in this region. This can be seen by taking snapshots at subsequent time steps of plasma density, as shown in figure 5.25.

5.2.3   *Extraction of Effective Diffusion Coefficients*

Once the results from the GBS simulation are available, it is possible to extract the radial profiles for effective diffusion coefficients to be passed to SOLPS for an optimized simulation. These parameters characterize the description of radial transport in SOLPS and we adopt for them the same kind of modeling used in the code (see section 3.1.2). The following terms, where averages are carried out in time, polar direction and axial direction, are therefore evaluated:

- an *effective density-driven particles radial diffusivity* computed as

$$D_{n,r} = -\frac{\langle \Gamma_r \rangle_{t,\vartheta,z}}{\langle \partial_r n \rangle_{t,\vartheta,z}} \tag{5.5}$$

  where the radial particles flux can be computed at each instant in time as

$$\Gamma_r = 2nV_{\mathbf{E}\times\mathbf{B},r} + nV_{dia,e,r} + nV_{dia,i,r} \tag{5.6}$$

  This definition for $D_{n,r}$ implies radial particles transport is assumed to be driven only by density variations.

- an *effective electron thermal diffusivity* computed as

$$\chi_{e,r} = -\frac{\langle q_{e,r} \rangle_{t,\vartheta,z}}{\langle n \rangle_{t,\vartheta,z} \langle \partial_r (T_e) \rangle_{t,\vartheta,z}} \tag{5.7}$$

  where the radial electrons heat flux can be computed at each instant in time as

$$q_{e,r} = nT_e V_{\mathbf{E}\times\mathbf{B},r} + nT_e V_{dia,e,r} \tag{5.8}$$

  This definition for $\chi_{e,r}$ implies radial electrons heat transport is assumed to be only conductive.
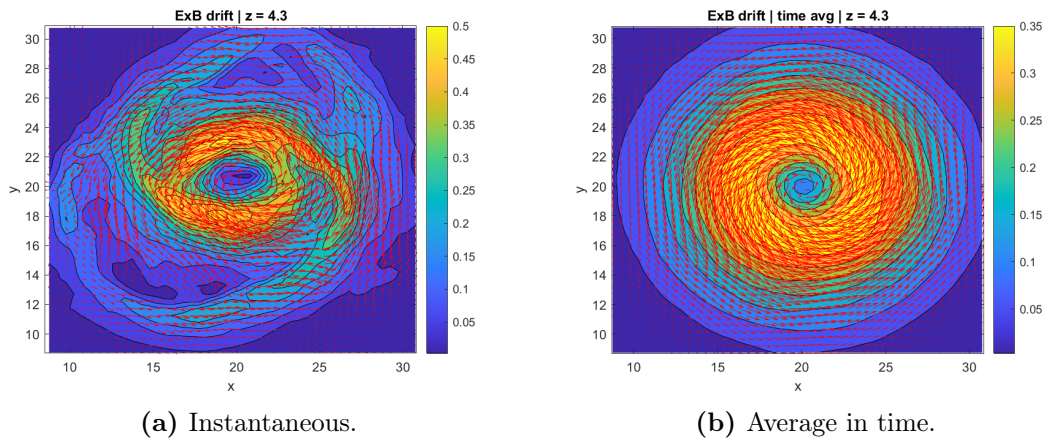
(a) Instantaneous.　　　　　　　**(b)** Average in time.

Figure 5.22: $\mathbf{E} \times \mathbf{B}$ plasma drift in GBS results. Quantities are expressed in GBS code units (see table 5.3).
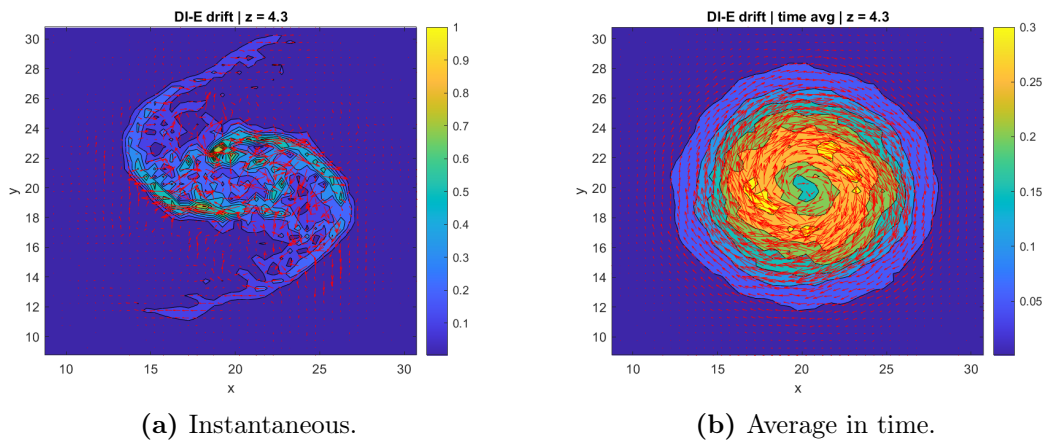
(a) Instantaneous.　　　　　　　**(b)** Average in time.

Figure 5.23: Electrons diamagnetic plasma drift in GBS results. Quantities are expressed in GBS code units (see table 5.3).
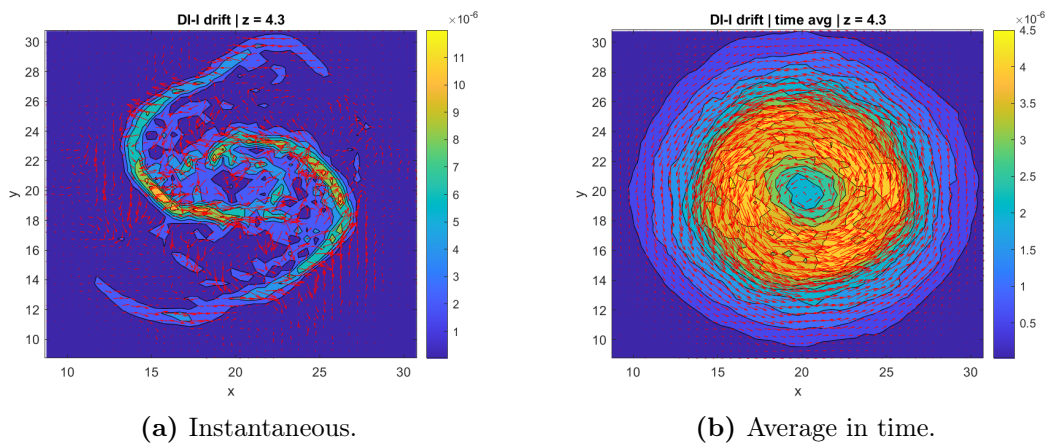
(a) Instantaneous.　　　　　　　**(b)** Average in time.

Figure 5.24: Ions diamagnetic plasma drift in GBS results. Quantities are expressed in GBS code units (see table 5.3).

Figure 5.25: Subsequent snapshots of plasma density in GBS results showing the rotation of the plasma due to the $\mathbf{E} \times \mathbf{B}$ drift. Quantities are expressed in GBS code units (see table 5.3).

- the *effective ion thermal diffusivity* $\chi_{i,r}$ couldn't be computed in the same way as $\chi_{e,r}$, as ions temperature was not evolved in the GBS simulation b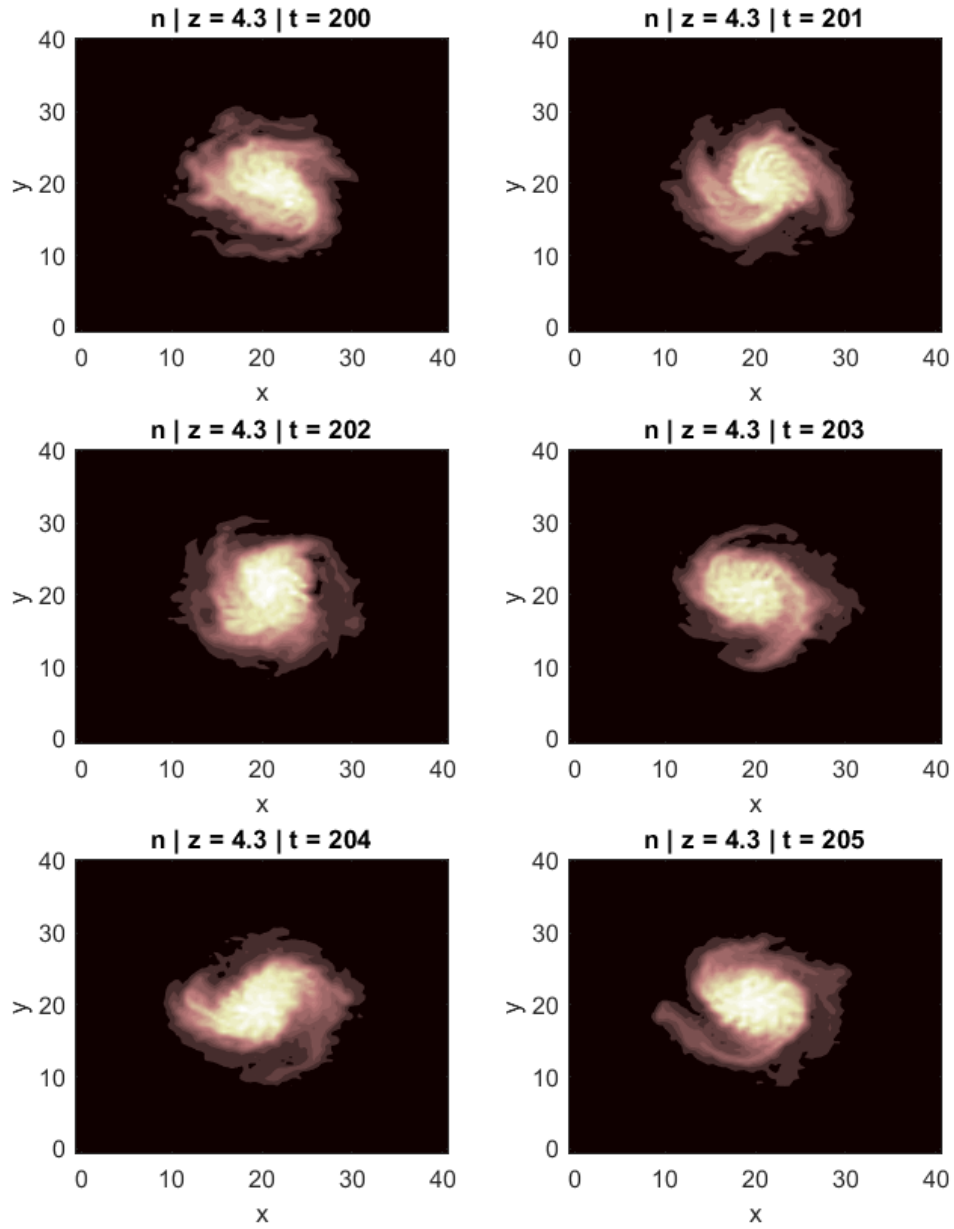ut it was assumed to be low and uniform in the system. Since in the settings for the preliminary SOLPS simulation these two quantities were set to the same value, we have decided to impose $\chi_{i,r} = \chi_{e,r}$ also for these radial profiles to be evaluated. The inclusion of ions temperature evolution in future GBS simulations could help overcome this problematic and evaluate $\chi_{i,r}$ in a completely self-consistent way.

The results of this procedure are shown in figure 5.26 where the value of the effective diffusion coefficients are expressed in SI units, the same used in SOLPS. The results recover satisfying values, especially near the radius up to which plasma source extends (see figure 5.8), which is also the region on which they have a larger influence as it'll be explained in section 5.3.1. Indeed, they are able to recover values with a difference below a factor 2 with respect to the ones used in the preliminary SOLPS simulation. We recall that those preliminary values were taken from literature [23, 37] and they were obtained by fitting simulated plasma profiles against experimental results. As expected, these coefficients' profiles increase in the region where perpendicular turbulent structures dominate the profiles of n and T_e (see figures 5.11 and 5.12). In addition, they tend to lower values at larger distances, where n and T_e rapidly decrease, and at lower radii, where instantaneous profiles are characterized by more homogeneous patterns. As it can be seen, in some points these results provide unphysical values, even predicting negative diffusion coefficients in some cases. This happens in two specific regions:

- at large radii, that is roughly for $r > 11$ in GBS code units (see table 5.3). In this region almost no plasma is present and therefore computations are spoiled by numerical instabilities and background fluctuations. Values in this region have therefore no physical meaning and they're of no interest for the current work as they're well beyond the radius of the B2.5 mesh in SOLPS.

- at small radii, that is roughly for $r \leq 2$ in GBS code units (see table 5.3). In this region computations are probably spoiled by the uniformity of n, T_i and T_e profiles in the radial direction, causing numerical instabilities in the computations. An higher resolution in the GBS simulation is thought to be beneficial in this direction to recover physical values also at small radii. Further work is then needed to recover reasonable results also in this region. A convergence test against the number of time-steps employed for the time averaging procedure in the computation of these profiles was carried out, pointing out the radial coordinate value below which results should be considered unphysical. This is shown in figure 5.27. A radial coordinate of $r = 2$ in GBS code units (see table 5.3) was identified for this threshold, corresponding to $r = 0.014\ m$ in SI units. Indeed, below this radius, it can be seen that profiles are not converging when the number of time-steps employed for the time averaging procedure increases, as it'd be expected.

The problem of unphysical values at low radii for effective diffusion coefficients was tackled in two different ways, which led to the production of two different inputs

related to these parameters for two different optimized SOLPS simulations being run. The first choice was to extrapolate the behaviour of effective diffusion coefficients at low radii: this was performed for points at radial coordinates $r \leq 0.014\ m$ employing modified Akima cubic Hermite interpolation. The second choice was to maintain the profiles as in the original computation shown in figure 5.26, just replacing in case negative values with a really low positive diffusivity values ($0.001\ m^2\ s^{-1}$) to avoid problems from the numerical side. The second procedure therefore still includes strong peaks for $D_{n,r}$ and for $\chi_{i,r}$ at low radii which are believed to be unphysical. Nevertheless, the choice of keeping them was carried out in order to see the sensitivity of the optimized SOLPS simulation to the effective diffusivities values at low radii. The corrected profiles on which the SOLPS input is then built are shown in figure 5.28.

The inputs for the two different optimized SOLPS simulations, based on the two described corrected profiles, are prepared with the following procedure[2]:

- a set of radial coordinates was defined, equally spaced in 18 points from $r = 0\ m$ to $r = 0.061\ m$, beyond the radius of the B2.5 mesh.

- the values of the effective diffusion coefficients on these points were considered.

- a file, called `b2.transport.inputfile`, was created in which a certain structure is defined pointing out the pairs of values for radial coordinate and corresponding effective diffusion coefficient value, for both $D_{n,r}$, $\chi_{e,r}$ and $\chi_{i,r}$. This input file will be read by SOLPS, interpolating effective diffusion coefficients from this set of radial coordinates onto the B2.5 mesh.

5.3   OPTIMIZED SOLPS SIMULATIONS

Two new optimized SOLPS simulations are run, each one employing one of the two corrected radial profiles (see section 5.2.3) evaluated self-consistently from the GBS results for the three effective diffusivities $D_{n,r}$, $\chi_{e,r}$ and $\chi_{i,r}$. The first simulation adopts the set of profiles with extrapolated behaviours for these quantities at low radii and its results are presented with the label *interpolated*. The second simulation adopts the set of originally obtained profiles, just cutting off to a really small positive value diffusivities when they'd get negative, and its results are presented with the label *original*. The comparison between these two different sets of radial profiles will underline the sensitivity of the optimized SOLPS simulation to the variation of effective diffusivities at low radii.

The input parameters for the optimized SOLPS simulations are the same presented in table 5.1 except for the effective diffusivities which are now provided by the `b2.transport.inputfile` (see section 5.2.3).

---

[2]This procedure follows the instructions present in [18], to which we refer for further details.
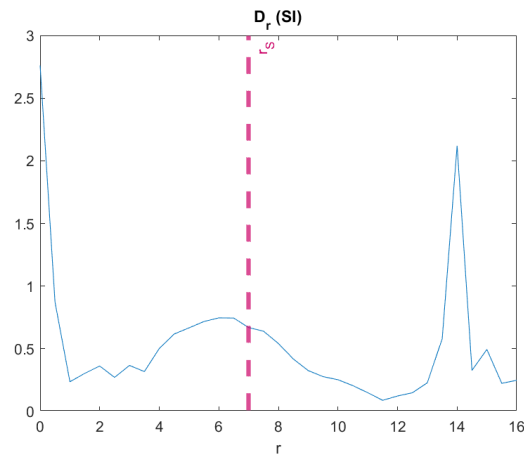
(a) Effective density-driven particles diffusivity.
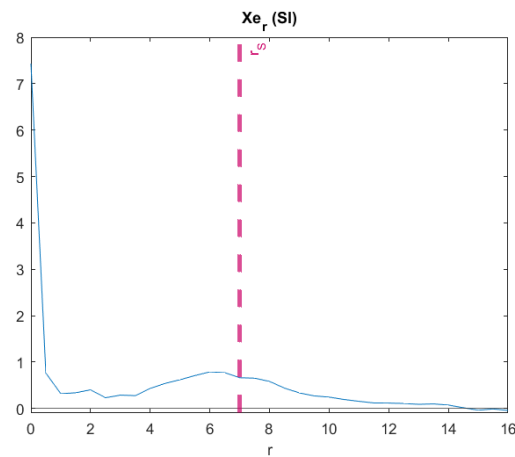
(b) Effective electron thermal diffusivity. This is equal to effective ion thermal diffusivity.

Figure 5.26: Radial profiles for effective diffusion coefficients. The radial coordinate is expressed in GBS code units (see table 5.3) while values for the coefficients are expressed in SI units ($m^2\ s^{-1}$). The radius of the plasma source (see figure 5.8) is also shown for reference with the red dashed line.

(a) Effective density-driven particles diffusivity.
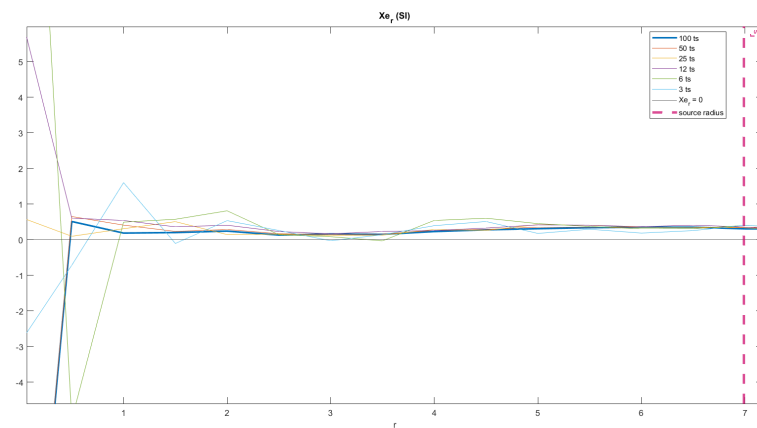
(b) Effective electron thermal diffusivity. This is equal to effective ion thermal
diffusivity.

Figure 5.27: Comparison of different radial profiles for effective diffusion coefficients
evaluated with different numbers of time-steps in the time averaging proce-
dure. The radial coordinate is expressed in GBS code units (see table 5.3)
while values for the coefficients are expressed in SI units ($m^2\ s^{-1}$). The
radius of the plasma source (see figure 5.8) is also shown for reference with
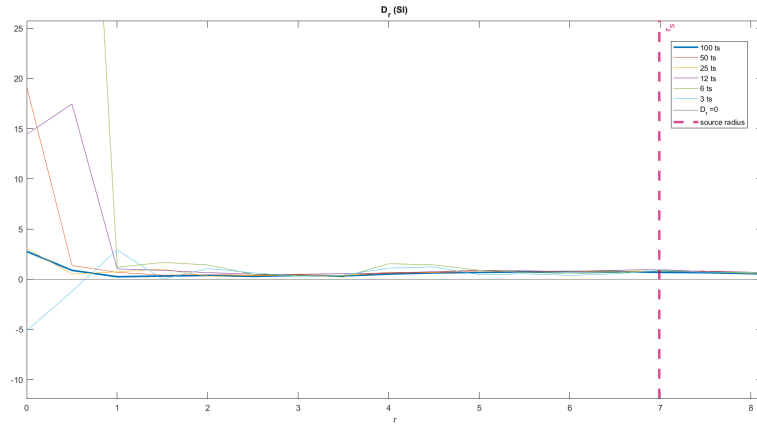the red dashed line.

(a) Effective density-driven particles diffusivity.

(b) Effective electron thermal diffusivity. This is equal
to effective ion thermal diffusivity.

Figure 5.28: Original and interpolated radial profiles for effective diffusion coefficients.
Quantities are expressed in SI units (radial coordinate: m, diffusivities:
$m^2\ s^{-1}$). The radius of the plasma source (see figure 5.8) is also shown for
reference with the red dashed line.

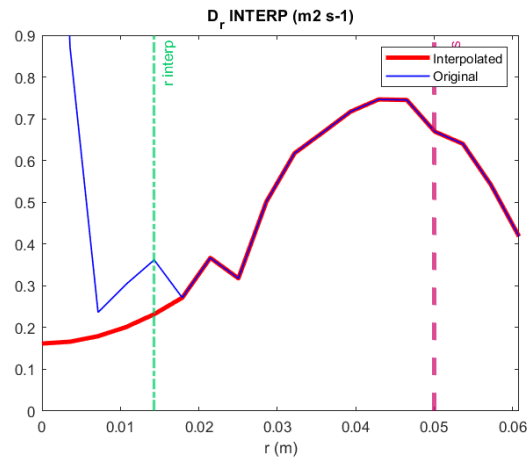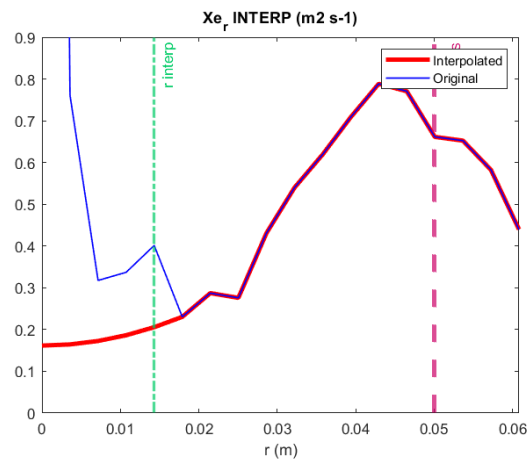### 5.3.1 *Results with Self-Consistent Effective Diffusion Coefficients*

In figures 5.29 and 5.30 the comparison between results from the preliminary and optimized SOLPS simulations for radial and axial profiles respectively, evaluated at mid-radius and mid-axis, are presented. It's also shown there the direct comparison between the profiles and the difference between the profiles from the preliminary and optimized simulations, considering the *interpolated* case. In figure 5.31 the difference between the 2D fields from the preliminary and optimized simulations, considering the *interpolated* case, is shown.

The first important comment about these results is that the outcomes of optimized SOLPS simulations in both the *interpolated* and *original* case are almost perfectly overlapping, even at low radii. This means the optimized SOLPS simulations are not sensitive to the strong differences in effective diffusivities at low radii. This can be explained by the almost flat profiles of plasma quantities near the axis of the configuration due to the imposed symmetric boundary conditions on that edge. This strongly limits the effect of diffusion-like phenomena as the radial derivative for different plasma quantities is almost zero. This leads to the conclusion that a further refinement of effective diffusivities values at low radii would be of no impact on the results in an optimized SOLPS simulation for this configuration.

The differences between the results obtained in the preliminary SOLPS simulation and those obtained in the optimized simulations are small and can be observed in the radial profiles mainly. These differences in the radial profiles are limited to the regions where plasma quantities exhibit radial variations, causing a small change in their slopes. The profiles of He^{1+} and electrons densities in optimized simulations are slightly smoothed out at larger radii, due to the fact that the self-consistent profiles for $D_{n,r}$ exceeds the value employed in the preliminary simulation (see figure 5.28 and table 5.1). As opposite the slopes in electrons and ions temperatures are slightly steeper due to the fact that the self-consistent values for $\chi_{e,r}$ and $\chi_{i,r}$ are lower than the ones employed in the preliminary simulation (see figure 5.28 and table 5.1). Relative variations are nevertheless almost always limited below a few percentage points. Their largest values are reached near the external radius of the mesh, where they have peaks of $\sim 5\%$ for ions and electrons densities and electrons temperature and of $\sim 10\%$ for ions temperature. In the axial direction variations are almost completely negligible. Finally, the small differences in the neutrals profiles can be ascribed by the noise associated to Monte Carlo routines.
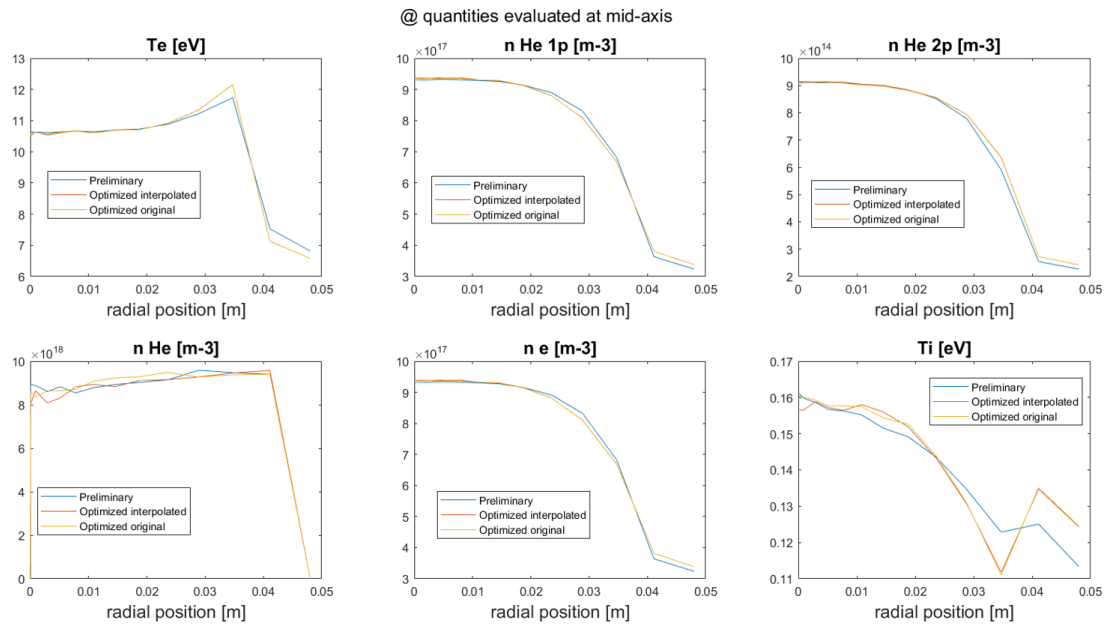
(a) Direct comparison.

(b) Difference between preliminary and optimized *interpolated* simulations.

Figure 5.29: Comparison between the preliminary and the optimized SOLPS simulations for radial profiles related to different plasma quantities.

(a) Direct comparison.
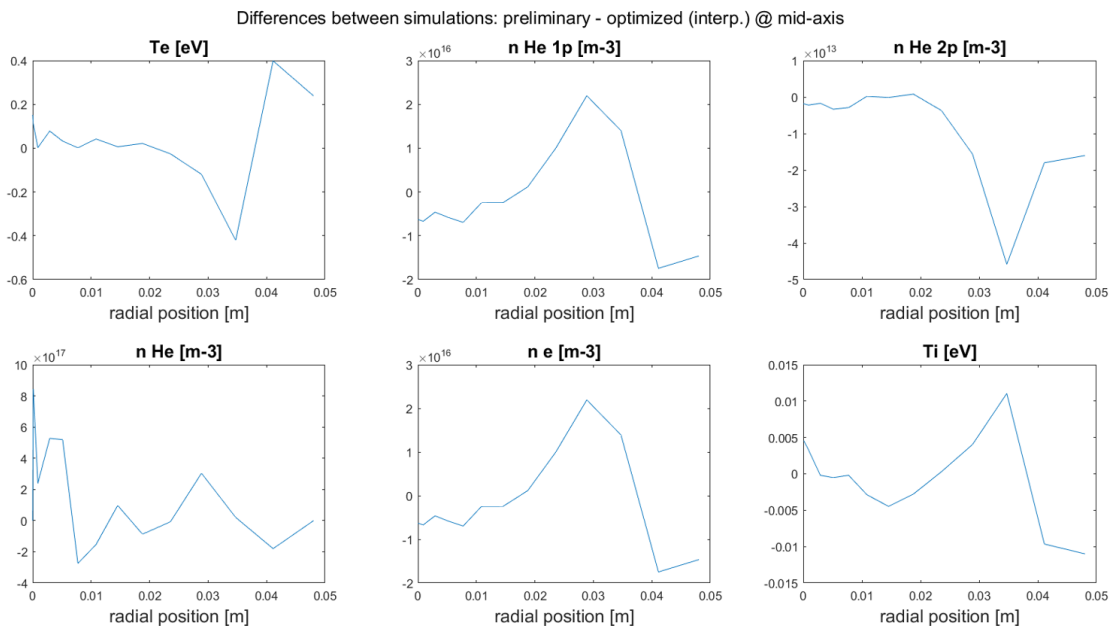

(b) Difference between preliminary and optimized *interpolated* simulations.
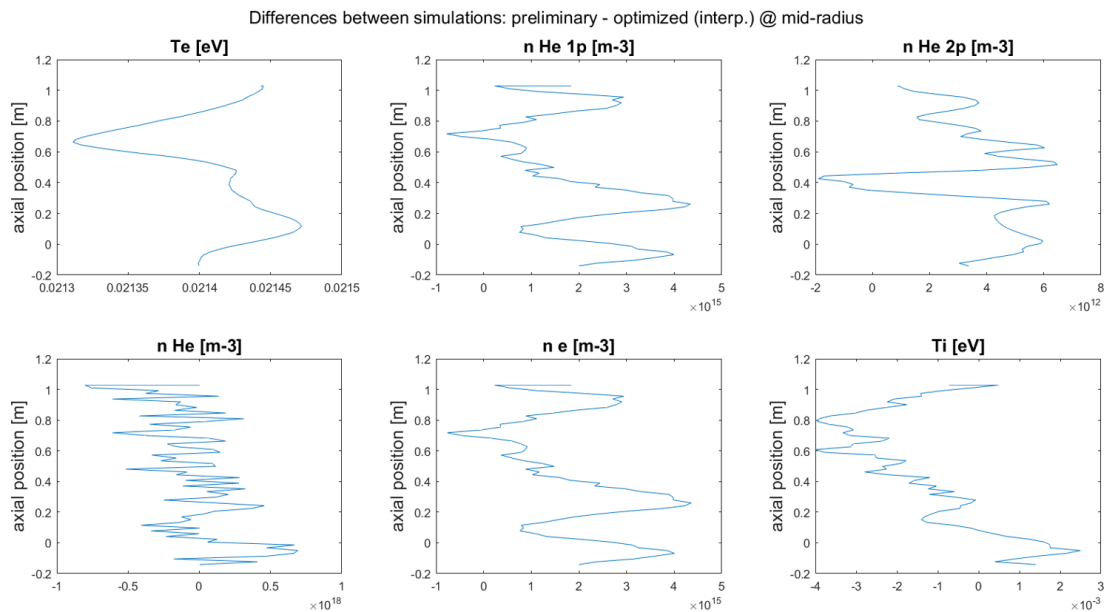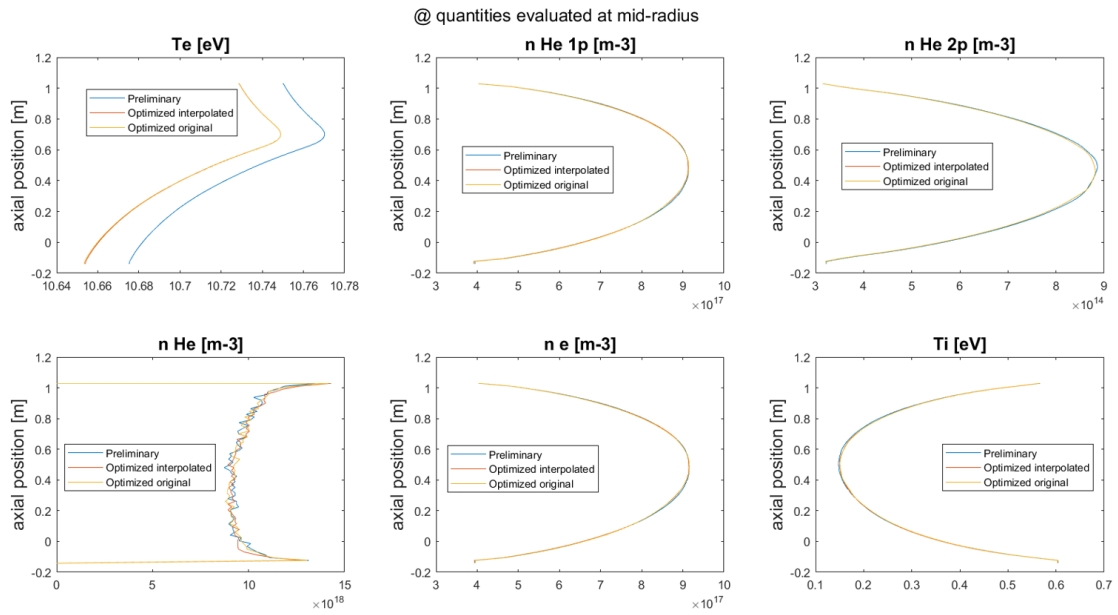
Figure 5.30: Comparison between the preliminary and the optimized SOLPS simulations for axial profiles related to different plasma quantities.
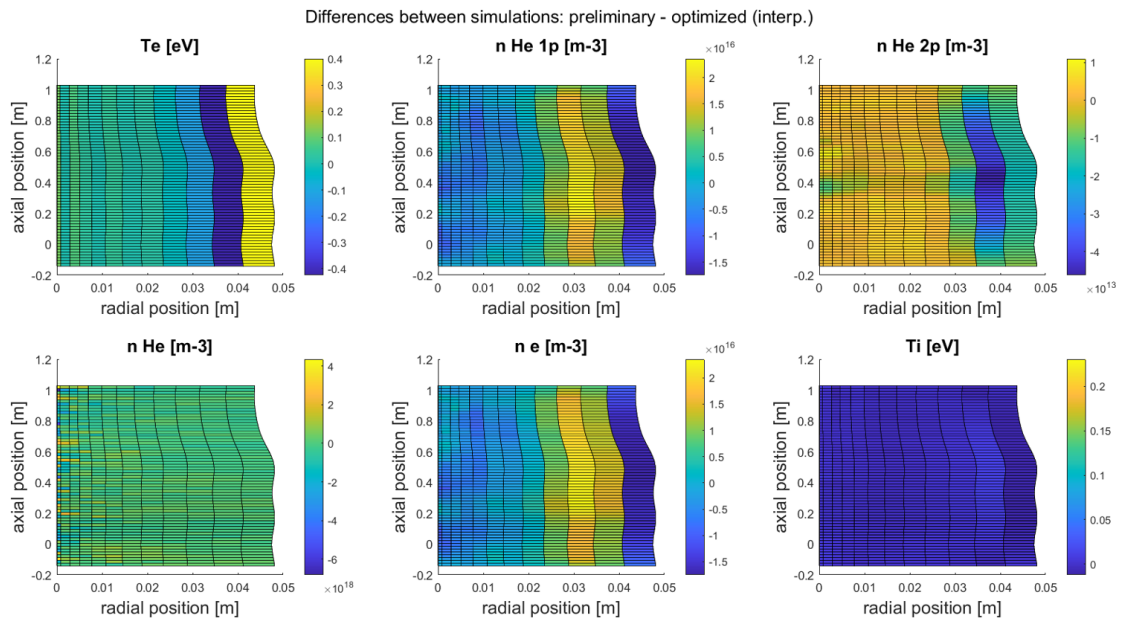
Figure 5.31: 2D maps showing the difference between the preliminary and the *interpolated* optimized SOLPS simulations for different plasma quantities.

Conclusion and Future Perspectives

In this thesis work a preliminary investigation of the coupling between the SOLPS and GBS codes was performed to simulate a linear plasma device configuration based on the GyM machine. Despite the increasing interest in fusion research community on the coupling of mean-field and first principle multi-fluid codes, specific for SOL conditions, only very few works of this type have been performed previously in literature. This is the first time the SOLPS and GBS codes are employed together for this task. In addition, despite the growing role of linear plasma devices in the study of fusion-relevant plasmas, the application of multi-fluid codes for simulating these configurations has only been seldom exploited. In particular, to our knowledge, this is the first work in this direction employing a coupling between a mean-field and a first principle multi-fluid code. Furthermore, many technical modifications on the GBS code were carried out in this thesis work to have the possibility to apply its current version on a linear configuration for the first time.

The first step in the work was devoted to the adaption of the GBS code in order to apply it to a linear plasma device configuration. Many technical modifications have been carried out on the code and this has allowed to introduce some crucial features for a linear machine, above all a straight magnetic field line configuration and the presence of solid targets in the direction of field lines. Nevertheless, the adapted code still lacks important aspects of the physical model, in particular a self-consistent evaluation of the neutrals dynamics. This limit is tackled by providing to GBS needed neutrals-related source/sink terms extracted from a preliminary SOLPS simulation.

After the adaption of the GBS code was completed, the actual simulations of interest could be carried out. An He plasma is considered for this work, characterized by parameters which are similar to those that characterize plasmas obtained in the GyM machine. The main focus of the adopted coupling strategy is the extraction of self-consistently evaluated radial profiles effective diffusion coefficients, to be employed in an optimized SOLPS simulation. The coupling strategy is based on 3 different simulations, called iteratively and each one providing inputs for the subsequent.

A first preliminary SOLPS simulation is run, employing a set of effective diffusion coefficients taken from literature and based on the fitting of results from SOLPS simulations to experimental data for the GyM machine. This simulation is able to provide steady-state profiles for different plasma quantities and neutrals density. Its outcomes are coherent with what is expected in this kind of configuration.

Post-processing is carried out on this simulation's results to extract the steady-state profiles for important neutrals-related terms. These are implemented as constant sources/sinks in the adapted GBS code.

A GBS simulation is then run and its results are analyzed. Instantaneous turbulent profiles are observed for different plasma quantities and some of their basic properties are investigated, such as average value, variance and skewness, also in comparison with previous results from the preliminary SOLPS simulation. Further analyses are carried out on the profiles of drift velocities, highlighting their instantaneous features and their effect on average in time. Finally, post-processing is carried out on this simulation's results to extract self-consistently radial profiles for effective diffusion coefficients to be employed in an optimized SOLPS simulation. This radial profiles are analyzed to assess their physical soundness by simple convergence analyses. In particular, two different radial profiles for each coefficient are considered, differing for their values near the axis of the configuration. In one case the original extracted profiles are kept, even if their values in this region are recognized as unphysical and showing really large peaks, while in the other a numerical extrapolation is employed to correct the results. This leads to two different optimized SOLPS simulations to be run in parallel and compared, in order to assess the sensitivity of their outcomes to this problematic.

Finally, the two optimized SOLPS simulations are run. Their results are discussed with respect to each other to show the influence of the different treatment for values of effective diffusion coefficients near the axis of the configuration. Then results are compared also to those obtained in the preliminary SOLPS simulation to investigate the effect of introducing self-consistently obtained radial profiles for effective diffusion coefficients in the chosen configuration.

The following conclusions are drawn from the results:

- the modified version of GBS can be successfully applied for simulations of linear plasma devices configurations. Despite employing different approximations, the results are satisfying and able to exhibit turbulent features in the plasma profiles and capture drift velocities patterns. Their outcomes, in terms of average profiles, are in large part comparable to those obtained by SOLPS simulations.

- the lack of self-consistent neutrals dynamics evolution in this modified GBS version can be efficiently compensated by introducing some external source/sink terms, aimed at reproducing some important neutrals-related effects in the system. In our case, this has been done with good results extracting their profiles from a previous SOLPS simulation.

- the GBS simulation shows turbulent structures evolve both in parallel and perpendicular directions with respect to the magnetic field. Both of them are not negligible in size with respect to the characteristic dimensions of the system. In the parallel direction elongated plasma filaments characterize the turbulent patterns while in the radial direction shorter structures drive the expansion of the plasma. Fluctuations level in plasma quantities are important in the system, especially at outer radii.

- from the GBS simulation it is possible to recover the distributions for the $\mathbf{E} \times \mathbf{B}$ and the diamagnetic plasma drift velocities, both for ions and electrons. Their average profiles are coherent with what was expected in the configuration of interest and are able to explain the plasma rotation observed in instantaneous plasma profiles.

- it is possible to obtain radial profiles for effective diffusion coefficients from a GBS simulation. Their shapes are coherent with what is expected from the analyses of plasma profiles, except near the axis of the cylindrical configuration. In addition they are comparable, with differences below a factor 2, to the effective diffusion coefficients taken from literature, which were obtained for the GyM configuration by fitting SOLPS simulations with respect to experimental data.

- optimized SOLPS simulations including radial profiles for self-consistent effective diffusion coefficients can be run. The sensitivity of the results to these coefficients variation is relatively low for the simulated linear configuration. In particular, it is approximately null with respect to the values near the axis of symmetry, implying further effort to recover more meaningful results around this region would have nearly no impact on the outcomes of the optimized SOLPS simulation.

This thesis work must be considered only a preliminary investigation of these topics and might be seen as a starting point for future works. In particular, from these conclusions, different developments can be considered, with the aim of improving current results.

With respect to GBS outcomes from this kind of simulations, they could be used to provide more insights about the physical phenomena governing turbulence in the chosen simulation setup. A refined analyses of GBS results could be carried out, allowing to highlight with more precision turbulent profiles characteristics, for example analyzing their spectra in both time and space. This would help to identify which kind of mechanisms and instabilities are playing a major role in turbulent structures development. A comparison with experimental studies, already carried out in the GyM machine on turbulent profiles [17, 20], could be also foreseen for this purpose.

Regarding directly GBS simulations of linear configurations, the current working version of the code can be for sure improved by relaxing all the different assumptions which it employs. This would provide an upgrade in the results of the simulations and it would allow a more consistent comparison between GBS and SOLPS. In particular, referring to the simulation setup investigated in this thesis work, three main steps are identified as the most important in this direction.

The first modification could be the relaxation of cold ions assumption, implying ions temperature is not evolved and is assumed to be low and uniform in the system. In this thesis work this assumption was adopted just to simplify the physical picture, notwithstanding the fact this was a reasonable approximation. Nevertheless, problems from the technical and numerical side are not foreseen regarding the inclusion of ions temperature evolution in GBS simulations from our experience. For this reason this improvement should prove to be pretty straightforward in future

works. The most important benefit related to this upgrade, from the practical side, would be the possibility to adequately assess the effective ion thermal diffusivity profiles in the system (see section 5.2.3).

Another improvement would be the possibility to simulate the effect of lateral radial walls in the configuration of interest. They'd be expected to have an impact on simulations results, especially when considering plasma sources extending up to or close to the lateral walls of the vacuum chamber, as it was assumed in previous works in literature on the GyM machine with the SOLPS code [37]. The inclusion of lateral radial walls in the GBS simulation domain would be quite a challenge both from the theoretical and the technical side. From the theoretical side, the definition of suitable boundary conditions for solid walls parallel to magnetic field lines is still an open issue as usual models applying for oblique incidence don't apply [99]. From the technical side, boundary conditions can't be directly applied on a circular edge in the perpendicular plane in the current version of GBS (see section 3.2.1). Two possible strategies to overcome this problematic could be to: (a) change the employed coordinate system, passing from a cartesian grid to a polar grid in the perpendicular direction, (b) introduce structures to use a penalization method to impose required boundary conditions also inside the computational domain [7, 9] maintaining a cartesian grid in the perpendicular direction. In both cases, deep and delicate technical modifications to the code should be carried out.

Finally, it would also be important for simulations to improve their neutrals dynamics evaluation. The plethora of neutrals-related effects taken into account in GBS should be increased with respect to the ones considered in this thesis work. In addition, it'd be better to include in a more self-consistent way neutrals-related effects in the system. The adaption of the GBS neutrals module to a linear configuration would be the most complete solution, in particular with respect to this last issue. It'd allow GBS to evolve neutrals dynamics in a completely self-consistent way and to run simulations independently without the need for any externally provided input related to their effects coming from SOLPS. Nevertheless, with respect to the current physical and computational model adopted for the neutrals module in GBS [15], this step would be likely a fairly demanding task both from the technical side and from the theoretical side for different reasons. One should also further evaluate if the current GBS neutrals module structure would be able to provide a complete analyses of the neutrals dynamics in the whole considered domain, including its boundaries, able to capture all the important features related to neutrals in the system. This point is particularly crucial in the view of a comparison with results from SOLPS, whose Monte Carlo approach to neutrals dynamics proves to be a really reliable and flexible tool in this direction. In addition, the inclusion of the neutrals module in GBS simulations would impact in a significant way the computational cost of a simulation. Therefore, at least for an initial improvement, it'd be more advisable to follow a simpler and lighter intermediate solution. Instead of implementing in GBS constant terms, extracted from a previous SOLPS simulation, and directly expressing neutrals-related sinks/sources, one could provide GBS an input profile for neutrals density and let the code itself evaluate corresponding source/sink terms using plasma quantities evolved directly by the code at each time-step. As before, this neutrals density profile can be also extracted from steady-state results of a previous SOLPS simulation, for example. The constant in time

neutrals density would be a reasonable assumption considering the low ionization degree characterizing the system and the fact neutrals evolution occurs on time scales way longer than the ones characterizing plasma species [23]. Nevertheless, this would allow to include the effect of turbulence developing in plasma quantities profiles into the computation of neutrals related terms in the system. From the practical side this would imply technical modifications should be carried out on the implementation of transport equations in GBS to include the neutrals-related terms defined in this way. The assessment of the stability of the code including these no longer constant sources/sinks should be investigated.

With respect to the coupling strategy employed between the SOLPS and GBS codes, an important methodological goal for this thesis has also been to underline criticalities and limits of the approach.

A first important open question could be related to the convergence of the results coming from iterated SOLPS and GBS simulations, an aspect which wasn't investigated in this thesis work. Indeed, the fact that self-consistent effective diffusivities profiles recovered results similar to the preliminary initial values and the low sensitivity of SOLPS outcomes with respect to these parameters implied convergence of results, for practical purposes, was reached after just the first iterative cycle of simulations. However, in different systems in which sensitivity to effective diffusion coefficients may be higher or in which the initial guess for effective diffusivities may prove to be fairly inadequate, the issue of convergence for the direct coupling strategy must be further analysed. If a slow convergence of results is found, the computational cost of the coupling approach may become quickly prohibitive. In particular, the GBS code simulations were the bottleneck of the strategy, as they were heavier than SOLPS ones, in this thesis work.

Another problematic to be investigated and evaluated should be the impact of SOLPS approximations on GBS results and, therefore, on the estimate of self-consistent effective diffusion coefficients profiles. Since in the coupling strategies applied in this thesis work GBS simulations describe a plasma evolution driven from sources extracted from SOLPS results, GBS results are in principle surely biased by the SOLPS ones and so are the computed effective diffusion coefficients profiles. As an example, the set of exponentially decaying boundary conditions for different plasma quantities, employed in this thesis at the outer radius of the B2.5 mesh in SOLPS, indirectly influences the values of the ionization density and electron power density losses profiles. With respect to this problematic, as the aim of the coupling is to provide self-consistent effective diffusion profiles to SOLPS, GBS simulations should be made as independent as possible from SOLPS ones, in particular from results related to its plasma quantities profiles. The strategies proposed in the previous paragraph, regarding the improvement on neutrals dynamics evaluation in GBS, could play a beneficial role also about this issue.

Acronyms

GBS   Global Braginskii Solver

Multi-fluid, first principle, turbulence code for edge plasma simulations developed at École Polytechnique Fédérale de Lausanne (EPFL).
http://gbs.epfl.ch/

ITER   International Thermonuclear Experimental Reactor

International project located at Cadarache, France, aiming at realizing an experimental nuclear fusion reactor based on the magnetic confinement approach and able to produce a net energy gain.
https://www.iter.org/

SOLPS   Scrape-Off Layer Plasma Simulations

It has been the workhorse SOL code suite for the design of the ITER divertor and it was the principal tool with which the ITER fuelling and pumping requirements were established. The code package is still intensively employed to study ITER and other devices plasma boundary physics and performances.
https://www.iter.org/newsline/-/2168

Bibliography

[1]   http://open.adas.ac.uk/ (cit. on p. 55).

[2]   U. E. I. Administration. "International Energy Outlook". In: (2016) (cit. on p. 2).

[3]   A. Eksaeva et al. "The impact of surface morphology on the erosion of metallic surfaces – Modelling with the 3D Monte-Carlo code ERO2.0". In: *Nuclear Materials and Energy* 27 (2021). DOI: https://doi.org/10.1016/j.nme.2021.100987 (cit. on p. 12).

[4]   A. Loarte et al. "Divertor Physics Topical 2007 Chapter 4: Power and particle control". In: *Nuclear Fusion* 47 (2007). DOI: http://dx.doi.org/10.1088/0029-5515/47/6/S04 (cit. on pp. 27–29).

[5]   A. Loarte et al. "Sizing up plasmas using adimensional parameters". In: *Nuclear Fusion* 47 (2007). DOI: http://dx.doi.org/10.1088/0029-5515/47/6/S04 (cit. on p. 11).

[6]   A. Mosetto et al. "Finite ion temperature effects on scrape-off layer turbulence". In: *Physics of Plasmas* 22 (2014). DOI: http://dx.doi.org/10.1063/1.4904300 (cit. on pp. 30, 70, 71).

[7]   A. Paredes et al. "A penalization technique to model plasma facing components in a tokamak with temperature variations". In: (2014). DOI: http://dx.doi.org/10.1016/j.jcp.2014.05.025 (cit. on p. 112).

[8]   A. S. Kukushkin et al. "Characteristics of divertor detachment for ITER conditions". In: *Journal of Nuclear Materials* (2015). DOI: https://doi.org/10.1016/j.jnucmat.2014.10.042 (cit. on p. 21).

[9]   A. Stegmeier et al. "Global turbulence simulations of the tokamak edge region with GRILLI". In: (2019). DOI: https://arxiv.org/abs/1904.09230v1 (cit. on p. 112).

[10]   A. Yoshizawa et al. *Plasma and Fluid Turbulence: Theory and Modelling*. IoP Publishing (cit. on p. 19).

[11]   A. Zeiler et al. "Nonlinear reduced Braginskii equations with ion thermal dynamics in toroidal plasma". In: *Physics of Plasmas* (1997). DOI: http://link.aip.org/link/doi/10.1063/1.872368?ver=pdfcov (cit. on p. 51).

117

[12] B. D. Scott et al. "Drift wave versus interchange turbulence in tokamak geometry: Linear versus nonlinear mode structure". In: *Physics of Plasmas* 12 (2005). DOI: https://doi.org/10.1063/1.1917866 (cit. on p. 30).

[13] B. Friedman et al. "Energy dynamics in a simulation of LAPD turbulence". In: *Physics of Plasmas* (2012). DOI: 10.1063/1.4759010 (cit. on p. 32).

[14] B. N. Rogers et al. "Low-Frequency Turbulence in a Linear Magnetized Plasma". In: *Physical Review Letters* (2010). DOI: http://dx.doi.org/10.1103/PhysRevLett.104.225002 (cit. on p. 32).

[15] C. Wersal et al. "A first-principles self-consistent model of plasma turbulence and kinetic neutral dynamics in the tokamak scrape-off layer". In: *Nuclear Fusion* 55 (2015). DOI: http://dx.doi.org/10.1088/0029-5515/55/12/123014 (cit. on pp. 20, 25, 30, 48, 55, 88, 112).

[16] D. Coster et al. *Extensions to the SOLPS edge plasma simulation code to include additional surface interaction possibilities.* https://www.academia.edu/24503327/Extensions_to_the_SOLPS_edge_plasma_simulation_code_to_include_additional_surface_interaction_posibilities (cit. on p. 38).

[17] D. Iraji et al. "Imaging of Turbulent Structures and Tomographic Reconstruction of GyM Plasma Emissivity". In: *Fusion Science and Technology* (2017). DOI: https://doi.org/10.13182/FST12-A15342 (cit. on p. 111).

[18] D. P. Coster et al. *SOLPS-ITER User Manual* (cit. on pp. 37, 45, 46, 67, 100).

[19] D. Reiter et al. *Collision Processes of Hydrocarbon Species in Hydrogen Plasmas: l. The Methane Family.* https://juser.fz-juelich.de/record/23576/files/Juel_3966_Reiter.pdf (cit. on p. 38).

[20] D. Ricci et al. *Characterization of electrostatic fluctuations in the low-density plasma of the linear device GyM.* https://publications.cnr.it/doc/81251 (cit. on p. 111).

[21] D. Schworer et al. "Influence of plasma background including neutrals on scrape-off layer filaments using 3D simulations". In: *Nuclear Materials and Energy* 12 (2017). DOI: https://doi.org/10.1016/j.nme.2017.02.016 (cit. on p. 30).

[22] E. M. Lifshitz at al. *Course of Theoretical Physics, Lev D. Landau, Volume 10: Physical Kinetics.* Elsevier Science, 1995 (cit. on p. 21).

[23] E. Tonello et al. "A point plasma model for linear plasma devices based on SOLPS-ITER equations: application to helium plasma". In: *Nuclear Fusion* 61 (2021). DOI: https://doi.org/10.1088/1741-4326/abfbb3 (cit. on pp. 13, 21, 32, 33, 61–64, 70, 75, 79–81, 99, 113).

[24] F.D. Halpern et al. "The GBS code for tokamak scrape-off layer simulations". In: *Journal of Computational Physics* 315 (2016). DOI: https://doi.org/10.1016/j.jcp.2016.03.040 (cit. on pp. 12, 30, 48, 51, 70, 88).

[25] H. Bufferand et al. "Implementation of drift velocities and currents in Soledge2D – EIRENE". In: *Nuclear Materials and Energy* 12 (2017). DOI: https://doi.org/10.1016/j.nme.2016.11.031 (cit. on pp. 28, 29).

[26] J. R. Myra et al. "Reduced model simulations of the scrape-off-layer heat-flux width and comparison with experiment". In: *Physics of Plasmas* 18 (2011). DOI: https://doi.org/10.1063/1.3526676 (cit. on p. 30).

[27] J. Rapp et al. "The Material Plasma Exposure eXperiment MPEX: Pre-design, development and testing of source concept". In: *2015 IEEE 26th Symposium on Fusion Engineering (SOFE)* (2015). DOI: 10.1109/SOFE.2015.7482351 (cit. on p. 12).

[28] J. Rapp et al. "Transport simulations of linear plasma generators with the B2.5-Eirene and EMC3-Eirene codes". In: *Journal of Nuclear Materials* 463 (2014). DOI: 10.1016/j.jnucmat.2014.12.058 (cit. on p. 32).

[29] J. W. Connor et al. "A review of theories of the L-H transition". In: *Plasma Physics Control* 42 (2000). DOI: https://doi.org/10.1088/0741-3335/42/1/201 (cit. on p. 11).

[30] J.Vogel et al. "Socio-economic conditions for satisfying human needs at low energy use: An international analysis of social provisioning". In: *Global Environmental Change* (2021). DOI: https://doi.org/10.1016/j.gloenvcha.2021.102287 (cit. on p. 1).

[31] K. Jesko et al. "Soledge2D-Eirene simulations of the Pilot-PSI linear plasma device compared to experimental data". In: *Contributions to Plasma Physics* (2018). DOI: https://doi.org/10.1002/ctpp.201700186 (cit. on p. 21).

[32] K. Jesko et al. "Soledge2D-Eirene simulations of the Pilot-PSI linear plasma device compared to experimental data". In: *Contributions to Plasma Physics* 58 (2017). DOI: http://dx.doi.org/10.1002/ctpp.201700186 (cit. on p. 32).

[33] K. Ješko et al. "Studying divertor relevant plasmas in the Pilot-PSI linear plasma device: experiments versus modelling". In: *Plasma Physics and Controlled Fusion* 60 (2018). DOI: 10.1088/1361-6587/aae80d (cit. on p. 12).

[34] L. W. Owen et al. "B2.5-Eirene modeling of radial transport in the MAGPIE linear plasma device". In: *Plasma Sources Science and Technology* 26 (2017). DOI: 10.1088/1361-6595/aa6389 (cit. on p. 32).

[35] M. Baeva et al. "B2-EIRENE SIMULATION OF PLASMA AND NEUTRALS IN MAGNUM-PSI". In: *Journal of Nuclear Materials* 363 (2007). DOI: https://doi.org/10.1016/j.jnucmat.2007.01.029 (cit. on p. 32).

[36] M. Endler et al. "Measurements and modelling of electrostatic fluctuations in the scrape-off layer of ASDEX". In: *Nuclear Fusion* 35 (1995). DOI: 10.1088/0029-5515/35/11/i01 (cit. on p. 20).

120   Bibliography

[37] M. Sala et al. "Simulations of Argon plasmas in the linear plasma device GyM with the SOLPS-ITER code". In: *Plasma Physics and Controlled Fusion* 62 (2020). DOI: https://doi.org/10.1088/1361-6587/ab7c4f (cit. on pp. 13, 29, 32, 33, 40, 46, 61, 62, 64, 67, 68, 79, 80, 99, 112).

[38] M. Schneider et al. "Modelling one-third field operation in the ITER pre-fusion power operation phase". In: *Nuclear Fusion* 59 (2019). DOI: https://doi.org/10.1088/1741-4326/ab3de0 (cit. on pp. 35, 63).

[39] M. Schneider et al. "Modelling one-third field operation in the ITER pre-fusion power operation phase". In: *Nuclear Fusion* 59 (2019). DOI: https://doi.org/10.1088/1741-4326/ab3de0 (cit. on p. 63).

[40] N. Bisai et al. "Role of neutral gas in scrape-off layer tokamak plasma". In: *Physics of Plasmas* 22 (2015). DOI: https://doi.org/10.1063/1.4913429 (cit. on p. 30).

[41] P. Helander et al. "Fluid equations for a partially ionized plasma". In: *Physics of Plasmas* 1 (1994). DOI: https://doi.org/10.1063/1.870470 (cit. on p. 25).

[42] P. Manz et al. "The diffusion limit of ballistic transport in the scrape-off layer". In: *Physics of Plasmas* 27 (2020). DOI: https://doi.org/10.1063/1.5133839 (cit. on p. 67).

[43] P. Ricci et al. "Plasma turbulence in the scrape-off layer of tokamak devices". In: *Physics of Plasmas* 20 (2013). DOI: https://doi.org/10.1063/1.4789551 (cit. on p. 30).

[44] P. Ricci et al. *Progress in simulating SOL plasma turbulence with the GBS code.* https://infoscience.epfl.ch/record/219159 (cit. on p. 30).

[45] P. Ricci et al. "Simulation of plasma turbulence in scrape-off layer conditions: the GBS code, simulation results and code validation". In: *Plasma Physics and Controlled Fusion* 54 (2012). DOI: http://dx.doi.org/10.1088/0741-3335/54/12/124047 (cit. on pp. 11, 29, 48, 70, 88).

[46] P. Vaezi et al. "Understanding the impact of insulating and conducting endplate boundary conditions on turbulence in CSDX through nonlocal simulations". In: *Physics of Plasmas* 24 (2017). DOI: http://dx.doi.org/10.1063/1.4980843 (cit. on p. 32).

[47] R. A. Pitts et al. "Status and physics basis of the ITER divertor". In: *Physica Scripta* 2009 (2009). DOI: 10.1088/0031-8949/2009/t138/014001 (cit. on p. 29).

[48] R. Betti et al. "Inertial-confinement fusion with lasers". In: *Nature Physics* (2016). DOI: http://dx.doi.org/10.1038/nphys3736 (cit. on p. 7).

[49] R. D. Hazeltine et al. "Analytical calculation of neutral transport and its effect on ions". In: *Nuclear Fusion* (1992). DOI: https://doi.org/10.1088/0029-5515/32/1/i01 (cit. on p. 21).

[50] R. J. Pearson et al. *Commercialising Fusion Energy.* 2020. Chap. 2: Review of approaches to fusion energy. DOI: doi.org/10.1088/978-0-7503-2719-0ch2 (cit. on p. 7).

[51] R. Schneider et al. "Plasma Edge Physics with B2-Eirene". In: *Contributions to Plasma Physics* 46 (2006). DOI: https://doi.org/10.1002/ctpp.200610001 (cit. on pp. 27–31, 42, 44).

[52] S. E. Segrè et al. *Fisica dei plasmi.* Zanichelli, 2010 (cit. on pp. 5, 7, 8, 16, 21–24, 66).

[53] S. Wiesen et al. "The new SOLPS-ITER code package". In: *Journal of Nuclear Materials* 463 (2015). DOI: https://doi.org/10.1016/j.jnucmat.2014.10.012 (cit. on pp. 37, 38).

[54] T. A. Carter et al. "Modeling of plasma turbulence and transport in the Large Plasma Device". In: *Physics of Plasmas* 17 (2010). DOI: http://dx.doi.org/10.1063/1.3527987 (cit. on p. 32).

[55] T. H. Shih et al. "Numerical Study of Outlet Boundary Conditions for Unsteady Turbulent Internal Flows Using the NCC". In: *NASA STI Report Series* (2009). DOI: https://ntrs.nasa.gov/api/citations/20090013281/downloads/20090013281.pdf (cit. on p. 71).

[56] T. J. M. Boyd et al. *The Physics of Plasmas.* Cambridge University Press, 2003 (cit. on pp. 26, 45).

[57] V. Rozhansky et al. "New B2SOLPS5.2 transport code for H-mode regimes in tokamaks". In: *Nuclear Fusion* 49 (2009). DOI: http://dx.doi.org/10.1088/0029-5515/49/2/025007 (cit. on pp. 45, 46).

[58] V. Rozhansky et al. "Simulation of tokamak edge plasma including self-consistent electric fields". In: *Nuclear Fusion* 41 (2001). DOI: https://ui.adsabs.harvard.edu/link_gateway/2001NucFu..41..387R/doi:10.1088/0029-5515/41/4/305 (cit. on pp. 45, 46).

[59] X. Garbet et al. "Physics of transport in tokamaks". In: *Plasma Physics and Controlled Fusion* 46 (2004). DOI: 10.1088/0741-3335/46/12b/045 (cit. on p. 16).

[60] Y. Hayashi et al. "Plasma detachment study of high density helium plasmas in the Pilot-PSI device". In: *Nuclear Fusion* 56 (2016). DOI: http://dx.doi.org/10.1088/0029-5515/56/12/126006 (cit. on p. 63).

[61] Y. Nishimura et al. "Coupling of Perpendicular Transport in Turbulence and Divertor Codes". In: *Contributions to Plasma Physics* 42 (2002). DOI: https://doi.org/10.1002/1521-3986(200204)42:2/4$\%$3C379::AID-CTPP379$\%$3E3.0.CO;2-1 (cit. on pp. 30, 31).

[62] Y. Sarazin et al. "Theoretical understanding of turbulent transport in the SOL". In: *Journal of Nuclear Materials* 313 (2003). DOI: https://doi.org/10.1016/S0022-3115(02)01437-X (cit. on p. 30).

[63] Y. Zhang et al. "Neutral impact on anomalous edge plasma transport and its correlation with divertor plasma detachment". In: *Nuclear Fusion* (2020). DOI: https://doi.org/10.1088/1741-4326/aba9ec (cit. on pp. 21, 29, 31).

[64]   A. Arakawa. "Computational design for long-term numerical integration of the equations of fluid motion: Two-dimensional incompressible flow. Part I". In: *Journal of Computational Physics* 1 (1966). DOI: https://doi.org/10.1016/0021-9991(66)90015-5 (cit. on p. 51).

[65]   M. Baelmans. *Code improvements and applications of a two-dimensional edge plasma model for toroidal fusion devices*. Katholieke Universiteit Leuven, 1993 (cit. on pp. 38, 41, 43).

[66]   R. Balescu. *Transport Processes in Plasmas*. Taylor Francis Group, 2002 (cit. on p. 16).

[67]   J. Bohdansky. ""A universal relation for the sputtering yield of monatomic solids at normal ion incidence". In: *Nuclear Instruments and Methods in Physics Research* (1984). DOI: https://doi.org/10.1016/0168-583X(84)90271-4 (cit. on p. 10).

[68]   B. J. Braams. *Computational studies in tokamak equilibrium and transport*. Rijksuniversiteit Utrecht, 1986 (cit. on p. 38).

[69]   S. I. Braginskii. *Reviews of Plasma Physics*. Vol. 1. Consultants Bureau, New York, 1965, pp. 205–309 (cit. on pp. 24–26).

[70]   J. F. Caneses. *Helicon wave propagation and plasma equilibrium in high density hydrogen plasma in converging magnetic field*. Australian National University, 2015 (cit. on p. 12).

[71]   F. Chen. *Introduction to Plasma Physics and Controlled Fusion*. Vol. 1. Plenum, 1984 (cit. on p. 8).

[72]   R. Chodura. "Plasma-wall transition in an oblique magnetic field". In: *The Physics of Fluids* 25 (1982). DOI: https://doi.org/10.1063/1.863955 (cit. on p. 18).

[73]   R. Fitzpatrick. *Online notes for Plasma Physics lectures: Braginskii Equations*. https://farside.ph.utexas.edu/teaching/plasma/Plasma/node53.html (cit. on pp. 11, 20).

[74]   J. Freidberg. *Plasma Physics and Fusion Energy*. Cambridge University Press, 2007 (cit. on pp. 3, 4, 6, 9, 10, 16, 17, 19, 28, 64, 66).

[75]   C. Hirsch. *Numerical Computation of Internal and External Flows*. Vol. 2. Wiley Sons, 1990 (cit. on p. 71).

[76]   ISTP-CNR. https://www.istp.cnr.it/en/ (cit. on pp. 13, 32).

[77]   K. S. Krane. *Introductory Nuclear Physics*. Wiley Sons, 1987 (cit. on p. 3).

[78]   A. S. Kukushkin. "Finalizing the ITER divertor design: The key role of SOLPS modeling". In: *Fusion Engineering and Design* 86 (2011). DOI: https://doi.org/10.1016/j.fusengdes.2011.06.009 (cit. on pp. 28, 29).

[79]   J. D. Lawson. "Some criteria for a power producing thermonuclear reactor". In: *Proceedings of the Physical Society* (1956). DOI: 10.1088/0370-1301/70/1/3039 (cit. on p. 6).

[80] W. Leonard. "Plasma detachment in divertor tokamaks". In: *Plasma Physics and Controlled Fusion* (2018). DOI: https://doi.org/10.1088/1361-6587/aaa7a9 (cit. on p. 21).

[81] R. J. LeVeque. *Finite Difference Method for Ordinary and Partial Differential Equations*. SIAM, 2007 (cit. on p. 71).

[82] J. Loizu. *The role of the sheath in magnetized plasma turbulence and flows*. École Polytechnique Fédérale de Lausanne, 2013 (cit. on pp. 11, 17, 18, 26, 49, 71).

[83] M.Knudsen. "Das Cosinusgesetz in der kinetischen Gastheorie". In: (1916). DOI: https://doi.org/10.1002/andp.19163532409 (cit. on p. 55).

[84] *Magnum-PSI description*. https://www.differ.nl/research/fusion-facilities-and-instrumentation/magnum-psi (cit. on p. 12).

[85] A. Mosetto. *Turbulent regimes in the tokamak scrape-off layer*. École Polytechnique Fédérale de Lausanne, 2014 (cit. on pp. 11, 53, 54).

[86] D. Naujoks. *Plasma-Material Interaction in Controlled Fusion*. Springer, 2006 (cit. on pp. 9, 10, 19).

[87] N. Ohno. "Plasma detachment in linear devices". In: *Plasma Physics and Controlled Fusion* 59 (2016). DOI: https://doi.org/10.1088/1361-6587/aa5394 (cit. on p. 12).

[88] ITER Organization. *Fuelling the fusion reaction*. https://www.iter.org/sci/FusionFuels (cit. on p. 5).

[89] P. Paruta. *Simulation of plasma turbulence in the periphery of diverted tokamaks*. École Polytechnique Fédérale de Lausanne, 2018 (cit. on pp. 11, 49, 50, 52, 76).

[90] J. L. Peterson. "Positivity preservation and advection algorithms with applications to edge plasma turbulence". In: *SIAM Journal on Scientific Computing* 35 (2013). DOI: https://doi.org/10.1137/120888053 (cit. on p. 51).

[91] C. C. Petty. "Sizing up plasmas using adimensional parameters". In: *Physics of Plasmas* 15 (2008). DOI: http://dx.doi.org/10.1063/1.2961043 (cit. on p. 5).

[92] *Plasma dynamics in MAGPIE*. https://physics.anu.edu.au/eme/eps/remote_sensing/magpie.php (cit. on p. 12).

[93] D. Reiter. *The data file AMJUEL: Additional Atomic and Molecular Data for EIRENE*. http://www.eirene.de/html/amjuel.html (cit. on pp. 20, 38).

[94] D. Reiter. *The data file HYDHEL: Atomic and Molecular Data for EIRENE based upon: Janev, Langer, Evans, Post, "Elementary Processes in Hydrogen Helium Plasmas"*. http://www.eirene.de/html/amjuel.html (cit. on pp. 20, 38).

[95] D. Reiter. *The EIRENE code, version: January 1992: users manual*. https://juser.fz-juelich.de/record/849638/files/J%C3%BCl_2599_Reiter.pdf. 1992 (cit. on pp. 38, 47, 48, 65).

[96] P. Ricci. "Simulation of the scrape-off layer region of tokamak devices". In: *Journal of Plasma Physics* 81 (2015). DOI: https://doi.org/10.1017/S0022377814001202 (cit. on pp. 19, 24, 27, 29, 30).

[97] K. U. Riemann. "The Bohm criterion and sheat formation". In: *Journal of Physics D: Applied Physics* 24 (1991). DOI: 10.1088/0022-3727/24/4/001 (cit. on p. 17).

[98] P. Sigmund. "Theory of Sputtering. I. Sputtering Yield of Amorphous and Polycrystalline Targets". In: *Physical Review Journals* 184 (1969). DOI: https://doi.org/10.1103/PhysRev.184.383 (cit. on p. 20).

[99] P. C. Stangeby. *The Plasma Boundary of Magnetic Fusion Devices*. IoP Publishing, 2000 (cit. on pp. 6, 10, 17–22, 26, 67, 112).

[100] E. Tonello. *Numerical investigation of nuclear fusion relevant plasmas in linear devices through the SOLPS-ITER code*. Politecnico di Milano, 2019 (cit. on p. 42).

[101] R. Toschi. "Nuclear fusion, an energy source". In: *Fusion Technology 1996* (1996). DOI: https://doi.org/10.1016/B978-0-444-82762-3.50006-9 (cit. on p. 2).

[102] A. Zeiler. "Tokamak Edge Turbulence". In: *IPP Report* (1997) (cit. on pp. 51, 92).

[103] V. M. Zhdanov. *Transport Processes in Multicomponent Plasmas*. Elsevier Science Publishers, 1988 (cit. on p. 16).

Ringraziamenti

Desidero ringraziare prima di tutto il mio relatore, il Prof. Matteo Passoni. Oltre al supporto pratico nello sviluppo di questo progetto, sin dal primo approccio riguardante la possibilità di svolgere il lavoro di tesi in questo ambito, ha dimostrato molta attenzione nel cercare di osservare le mie preferenze in termini di argomenti trattati, tipologia di lavoro, tempistiche e possibilità di collaborare con qualche istituto straniero.

Allo stesso modo desidero ringraziare il Prof. Paolo Ricci per l'incredibile disponibilità mostrata nei miei confronti, sia riguardo ai miei dubbi e le mie proposte rispetto al lavoro, sia riguardo alla possibilità di svolgere un periodo in visita all'EPFL a Losanna, in Svizzera.

Vanno inoltre assolutamente ringraziate le due persone che, in parallelo, hanno direttamente supervisionato le diverse parti di questa tesi. Senza di loro sarebbe stato letteralmente impossibile completare questo progetto. Elena Tonello è stata principalmente impegnata nel supportare il mio lavoro "lato PoliMi" e nella stesura dell'elaborato scritto. La ringrazio in particolare per la grande pazienza che ha avuto nel controllare tutto ciò che scrivevo e per gli innumerevoli consigli e discussioni riguardanti i più svariati argomenti in questa tesi. Louis Stenger è invece stato impegnato a supervisionare lo sviluppo del progetto "lato EPFL". Lo ringrazio in particolare perché mi ha sempre supportato e guidato nelle fasi tecniche del lavoro, soprattutto quando vi erano delle difficoltà.

Mi ritengo dunque molto fortunato ad avere avuto la possibilità di lavorare con queste quattro persone, dalle quali ho imparato molte cose sia a livello nozionistico che a livello professionale.

In aggiunta, devo assolutamente ringraziare tutte le persone appartenenti alla mia sfera personale: i miei genitori Andrea e Paola, mio fratello Alessandro, la mia fidanzata Francesca e tutti i miei amici. A causa di questa tesi avete tutti sopportato in diversa misura le mie lamentele e miei impegni per tanto tempo. Vi sono davvero grato per questo.

PS: non preoccupatevi, potete anche non leggere il resto.

Milan, October 2021   M. C.